©2020

Joseph J Sherba Jr

ALL RIGHTS RESERVED

TOWARDS THE DEVELOPMENT OF A CONTINUOUS-FLOW, SMART MICRO-ELECTROPORATION TECHNOLOGY TO ADVANCE CELL THERAPY

By

JOSEPH J SHERBA JR

A dissertation submitted to the

School of Graduate Studies

Rutgers, The State University of New Jersey

In partial fulfillment of the requirements

For the degree of

Doctor of Philosophy

Graduate Program in Biomedical Engineering

Written under the direction of

Jeffrey D. Zahn

And approved by

_____

_____

_____

_____

_____

_____

New Brunswick, New Jersey

May 2020

ABSTRACT OF THE DISSERTATION

TOWARDS THE DEVELOPMENT OF A CONTINUOUS-FLOW, SMART MICRO-ELECTROPORATION TECHNOLOGY TO ADVANCE CELL THERAPY

by JOSEPH J SHERBA JR

Dissertation Director:

Jeffrey D. Zahn

FDA approved patient-derived cellular therapies are a groundbreaking biomedical/clinical accomplishment in recent years. This therapy involves the intricate process of removing cells from the patient, genetically modifying them *ex vivo*, and then returning the cells to the patient to combat disease. Though this field is very promising for treatment of otherwise untreatable cancers and other genetic/auto-immune disorders, current manufacturing costs may make this life-saving therapy unaffordable to the general population. Of the manufacturing steps, the use of viral vectors for gene delivery remains the 'rate-limiting' step from an economic point of view. Electroporation is an alternative to viral-mediated gene delivery. Electroporation is an electro-physical, non-viral approach to perform DNA, RNA, and protein transfections of cells. Upon application of an electric field, the cell membrane is compromised, allowing the delivery of exogenous materials into cells. This dissertation focuses on advancing a novel, micro-electroporation technology capable of electrically monitoring the degree of cell membrane permeabilization throughout the

process. Technological advancements are made from a biochemical standpoint, through optimization of the electroporation buffer that cells are suspended in during the electroporation process, as well as microfluidic/hardware/software design. Highly desirable biomedical and clinical applications, such as DNA plasmid delivery and gene editing with CRISPR-Cas9, are demonstrated using this micro-electroporation technology. Furthermore, ideas to enhance the overall throughput of the technology are introduced, such single-cell level feedback control, population-based feedback control, and microfluidic device parallelization. Ultimately with further technological advancement, this continuous-flow, micro-electroporation system may shift the existing cell therapy manufacturing paradigm, with hopes of eliminating the need for viral-mediated gene delivery.

ACKNOWLEDGEMENTS

As I sit and write this section of my thesis, the COVID-19 pandemic has not only been oppressing the country, but the entire globe for an unprecedented period now. Though this has allowed for countless hours of writing and thought towards the completion of this dissertation, the ideas and thoughts regarding the many whom have helped ensure I reach a successful end to this journey, and the start of new adventures, vastly supersedes and outweighs that of this virus.

Broadly speaking to my thesis committee, Dr. Jeffrey Zahn, Dr. David Shreiber, Dr. Hao Lin, Dr. Jerry Shan, Dr. Jay Sy, Dr. Christine Roberts, and Dr. Joel Maslow, I cannot thank you all enough for your insight and guidance, both scientifically and professionally. Through the many hours spent together during meetings not only did your mentorship prepare me as I embark on my professional career but also your ability to lead by example as I have got to witness some of your very own major professional achievements. It has been a great pleasure learning from each of you throughout the course of my graduate studies.

To my thesis advisor, Dr. Zahn, you have been an invaluable resource throughout the completion of this research and dissertation. You are truly passionate about your field of expertise, which shows in your mentoring style and the work environment fostered in the BioMEMS laboratory. I hope to carry on the problem-solving skills that I have learned and witnessed first-hand as I continue in my professional development as a biomedical engineer.

To Dr. Shreiber, I always considered you as a co-advisor throughout my time at Rutgers. Even before arriving to New Jersey, I will remember our phone call conversation in regard to transitioning from the Master's to PhD program. Your constructive criticisms through the years have helped mold me into an efficient scientific communicator and I am confident in my ability to give an effective research/professional presentation no matter the audience.

To Dr. Lin, the unappointed leader and person who makes the wheels churn for the electroporation group. You have provided a solid example of professionalism that I will continue striving towards as I continue in my development.

To Dr. Shan, not only did I value your thoughtful insights and suggestions throughout the development and troubleshooting of this research, but also the mannerisms in which you provided the insight.

To Dr. Sy, I understand you do not fall within our electroporation group. However, following my teaching assistantship year under your guidance, I could tell you were the right fit for my final BME thesis committee member. I knew you would be able to provide constructive feedback when necessary, so thank you for serving on my committee.

To Dr. Roberts and Dr. Maslow, first and foremost thank you for agreeing to serve on my thesis committee. You both provided valuable perspectives on the directions of this project and provided me with a unique PhD experience. This experience, I believe, has put me in a good position to continue to succeed as a scientist.

In addition to the members of my thesis committee. I would also like to acknowledge Dr. Martin Yarmush, Dr. Rick Cohen, Dr. Li Cai, and Dr. Hilton Kaplan. Dr. Yarmush, thank you for providing mentorship during my year as a GAANN fellow. Dr. Cohen, thank you

for both lending out equipment and providing valuable suggestions for executing certain experiments. Similarly, Dr. Cai, thank you for making the BTX pulse generator readily available to others to carry out electroporation experiments. Lastly, Dr. Kaplan, thank you for providing me with an additional income source as the TA for your Applied Clinical Electrophysiology class. I enjoyed working along-side you.

I would like to express my gratitude to those operating behind the scenes in the administrative offices in the biomedical engineering department, Lawrence Stromberg, Robin Yarborough, Stratos Loukidis, and Linda Johnson. On numerous occasions each of you have provided me with assistance in solving some sort of issue, whether lab-related or not.

To all the friends I have made throughout my time at Rutgers, especially those whose paths I have crossed with in both the BioMEMS and Shreiber Labs. Thank you for providing a source of encouragement, brainstorming, and an outlet for stress relief. I would like to specifically thank Mingde (Jack) Zheng, Rick Castellano, and Xin Liu. Jack, thank you for serving as my research mentor in my early graduate school years. Rick, thank you for always lending a hand when asked upon, sacrificing time away from your own work to help me in areas of your expertise. Similar, Xin, thank you for sacrificing your time to provide illustrations / animations to be utilized both within this document and research presentations.

To my family and friends outside of Rutgers. I would not have been able to accomplish this feat without your devoted love and support. There are so many people who either continue to, or, at one point or another, have played a critical role in my life, and for that,

I am forever grateful. I would like to personally acknowledge the Mroz, the Farrow, the Dougherty, the Rieger, and the Makowski families.

To my parents, Mary and Joe, though we may wish things took a different path, thank you for providing me a foundation to build off. A foundation built on having a curiosity for learning and exploring the natural world, taking responsibility in pursuing my education, and persevering when the odds are stacked against me.

To my brother and sister-in-law, Josh and Kelly, saying thank you does not do enough justice. Just know that I am forever grateful to have you both in my life and I am excited to see what the future has in store for all of us.

Lastly, I would like to acknowledge and extend my gratitude to Jessica. I know you did not know what you had gotten yourself into when this graduate school journey began. However, I appreciate all the sacrifices you made along the way to ensure we reach this milestone. This victory is as much yours as it is mine. Love you.

DEDICATIONS

To my friends and family,

not only have you helped to provide opportunities, but the motivation to pursue them.

~Nigdy Rozpacz~

TABLE OF CONTENTS

LIST OF TABLES

LIST OF ILLUSTRATIONS

Chapter 1

Introduction

1.1 Overview of Cell Therapy

The FDA defines human gene/cell therapy as the modification or manipulation of the expression of a gene or altering the properties of living cells for therapeutic use[1]. This therapeutic can work through various mechanisms, including: 1—Replacing a disease-causing gene with a healthy copy of the gene. 2—Inactivating a malfunctioning disease-causing gene. 3—Introducing a new/modified gene into the body to combat disease[2]. These mechanisms of action are currently being investigated in clinical settings for both *in vivo* and *ex vivo* therapies (**Figure 1.1**), however, for the purpose of this thesis the focus is on the *ex vivo* gene/cell therapy landscape.

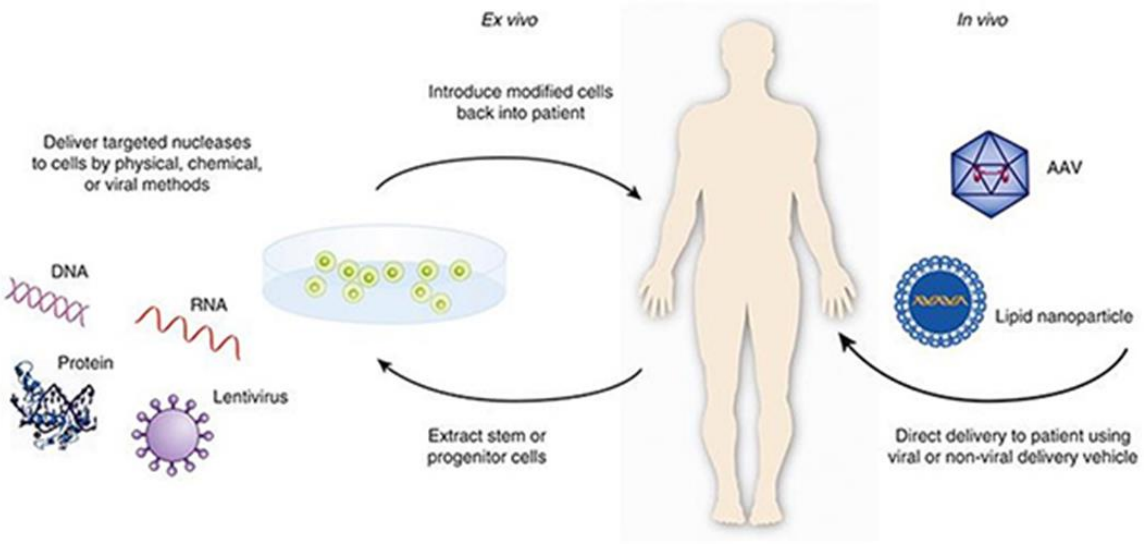

Figure 1.1 Overview of cell/gene therapy.

Patient-derived cellular gene therapies involve an intricate process in which cells are removed from the patient, genetically modified *ex vivo*, and then returned to the patient to combat disease[1]. The most widely known and growing market for this therapy is CAR-T cell therapies to combat certain cancers (CAR—Chimeric Antigen Receptor, T—T Cell Lyphocyte). In this therapy, the patients' own T-lymphocytes are extracted and genetically engineered to produce a receptor on their membrane to better recognize and attack cancer cells upon T-cell reinfusion[3]. Currently, the FDA has approved two CAR-T cell therapies. The first, Kymriah from Novartis, for the treatment of adults with relapsed or refractory diffuse large B-cell lymphoma and young adults up to the age of 25 with relapsed or refractory acute lymphoblastic leukemia[4]. The second FDA approved therapy, Yescarta from Kite Pharma (acquired by Gilead), for the treatment of adults with various types of B-cell lymphomas that have not responded to traditional therapies[4]. Although, only two therapies have been granted approval from the FDA, a large amount of industrial resources are being utilized for the advancement of this field, in particular as of 2018, there were a total of 753 cancer cell therapies under development, with 375 in clinical trials[5-6].

As would be expected, these ongoing clinical trials differ from one another, in aspects such as type of cancer to be treated, the cancer disease target (i.e. receptor to be encoded for), mechanism of action (CAR, TCR, TAA, TSA, TIL, iPSC, CRISPR), and white blood cell type utilized[6]. However, the overall cell therapy manufacturing process is primarily conserved across the different therapies, with slight differences in technologies used for each step[3]. Briefly, cell therapy manufacturing can be broken into the following 7 individual steps (**Figure 1.2**): 1—Apheresis. 2—Washing/Separation. 3—Activation. 4—Gene Delivery. 5—Cell Expansion. 6—Formulation. 7—Cell Therapy Administration[3].

The apheresis step involves separating out the patients' white blood cells from whole blood. During this procedure it is not uncommon for anticoagulants, red blood cells, and platelets to remain in the separated sample, which act as contaminants that have been shown to have downstream effects on white blood cell activation and overall clinical efficacy[7-8]. Thus, following apheresis, ample washing steps are required to remove these contaminants. Most therapies require the selection of a specific white blood cell type for the given therapy. A common method is to use micron-sized magnetic beads labeled with an antibody specific to the subpopulation of white blood cells of interest[3]. Once the population is enriched, the cells are to be activated in culture such that they can grow and proliferate. Naturally, T-cells are activated *in vivo* through the interaction with antigen presenting cells such as dendritic cells[9]. However, this is not an ideal scenario *ex vivo* and additional methodologies have been developed to perform the activation, such as the use of monoclonal antibodies and interleukins, cell-sized anti-CD3/CD28 antibody coated magnetic beads, and the use of non-viable antigen presenting cells[3,10]. Of the three methods, the anti-CD3/CD28 antibody coated magnetic beads is used most prevalently in the clinic[3]. Following activation, cells are ready for genetic engineering via gene delivery. This step is the primary focus of this thesis and will be discussed further in future sections. Briefly, either a viral or non-viral method (such as electroporation) is used to introduce foreign genetic material into the cells, which encodes for the cell membrane receptor to target cancer cells[3]. Following gene delivery, cells are then expanded to the desirable cell number via static culture T-flasks, static culture bags, and/or rocking motion bioreactors[3]. Final cell numbers / cell density and media composition is then adjusted for either cryopreservation or delivery back to the patient as the 'Cell Therapy'[3].

The current state of the art of the manufacturing process for cell therapy production involves many separate steps, some of which require intensive manual labor. Altogether, current cost to patients to receive these life-saving treatments ranges from $150,000—$300,000, with the first FDA approved treatment Kymriah costing $475,000 per treatment[3]. In order for cell therapies to be realized as a commonplace, life-saving treatment, this cost must be driven down to increase the breadth of patients whom will benefit.

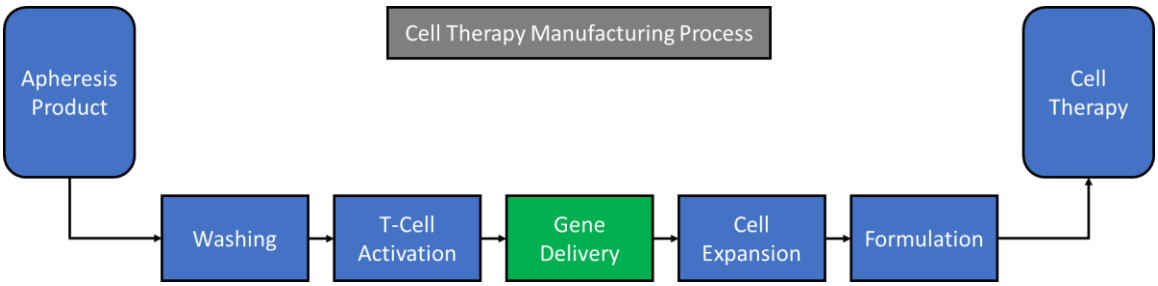

Figure 1.2 Ex Vivo Cell therapy manufacturing process. Following apheresis, white blood cells are washed and separated to collect the specific subset of cells required. These cells are activated to allow for growth and proliferation. Gene delivery is performed to transfect the cells to produce the membrane receptor of interest. These cells are expanded in number required for therapeutic benefit before they are formulated and delivered back to the patient. (Figure adapted from Vormittag *et al.*)

1.2 The Ideal *Ex Vivo* Transfection Method

Overall, the many steps involved in cell therapy production need to be optimized in order to drive down the cost for patients. Relative to this thesis is the step of gene transfer. Current FDA approved treatments use viral methods to perform this step[4]. Although, viral transfections can result in high transfection efficiencies and lead to clinically relevant outcomes, the usage of this material has several drawbacks, a major one being the cost involved in the production of and quality assurance of viral manufacturing[3,11]. However, cost is only one category to consider when developing or choosing the 'ideal' *ex vivo* delivery system. All of the metrics of an ideal *ex vivo* delivery system are: 1—safety/efficiency. 2—scalability. 3—universality. 4—cargo flexibility. 5—cost. (**Figure 1.3**)[11]. Existing delivery modalities will be discussed with these metrics in mind in the next sections, but briefly, each of these metrics will be defined.

An ideal *ex vivo* delivery system should be capable of addressing these 5 design needs. First and foremost, the method for delivery cannot introduce detrimental effects into the overall cell therapy manufacturing paradigm, that upon reinfusion to the patient, would result in severe side effects, deeming the therapy unsafe. In addition to the safety of the patient, the delivery method needs to be efficient. Efficiency in this manner refers to the ability for the resulting gene delivery step to be performed with both a high resulting cell viability, or the number of cells that survive the transfection step, and a high transfection efficiency, or the number of cells that both receive and transcribe the gene of interest. Secondly, the ideal system must be scalable and capable of working with a large range of cell numbers, 10^2—10^9 cells. The delivery method should be considered universal to all cell types/populations, and thus capable of accounting for both the intrinsic biologic

variability seen between cells of various lineages and amongst a given population of the same cell type. The delivery mechanism must not be limited on the cargo that it can delivery, accounting for the physical/chemical properties of the molecules, considering things like charged vs. uncharged, polar vs. nonpolar, and low molecular weight vs. high molecular weight. Lastly, as previously mentioned, the technology to perform the intracellular delivery must not add severe costs to the overall process, as this will prevent the adoption of the technology into a real-world setting, regardless of how well the technology can perform in the other categories.

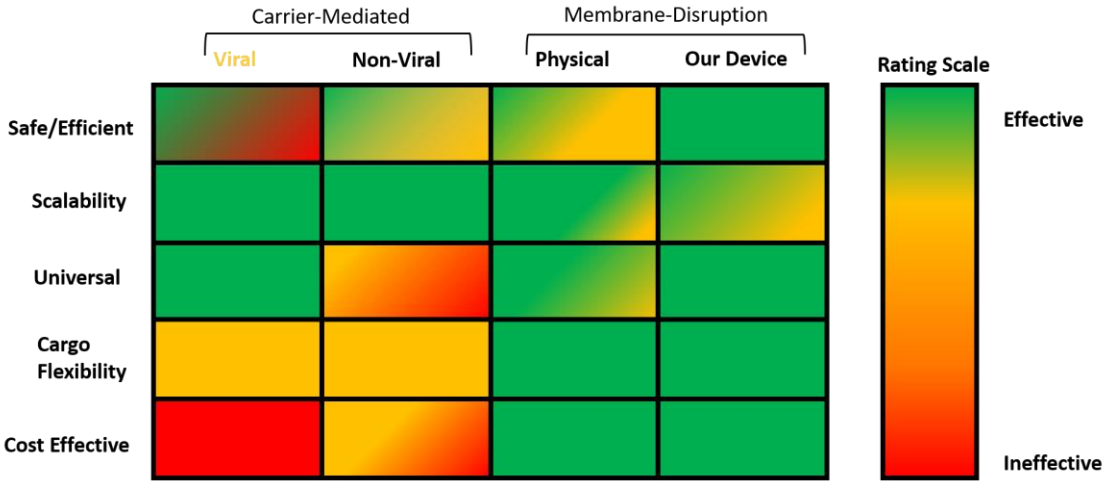

Figure 1.3 Metric comparison chart of *ex vivo* delivery methods. The ideal *ex vivo* delivery system should be effective in all of the categories. Adapted from *Stewart et al.*

1.3 Current Methods for Transfection

The ideal *ex vivo* intracellular molecular delivery technology requires the ability to deliver a vast variety of materials to all biological cells, in small and large quantities, in both a safe and effective manner, while keeping the overall cost of the procedure at a minimum. At this stage of the various technologies capable of performing *ex vivo* molecular delivery, there does not exist an 'ideal' delivery modality, and R&D is still advancing the various technologies. In this section, each of the existing technologies will be discussed in detail in respect to where they stand as being considered the 'ideal' *ex vivo* intracellular delivery technology. There are many technologies available and they are lumped into an umbrella category, such as viral-mediated delivery and non-viral mediated delivery. The non-viral methods can further be broken into carrier-mediated or biochemical mechanisms or a variety of physical-based intracellular delivery technologies.

1.3.1 Viral

Viral-mediated transfection is one of the most common methods used in cell therapy manufacturing and has the advantage of experience/time used in clinical trials over other methods of delivery. As previously mentioned, both FDA approved cell therapies on the market, Kymriah and Yescarta, both use viruses, in particular lentivirus and retrovirus, respectively, to perform the gene delivery step in their bioprocessing[4]. In addition to the use of lentivirus (7.3% of clinical trials, increase from 2.9% in 2012) and retrovirus (17.4% of clinical trials, however numbers are declining), ongoing clinical trials are seeing an increase in adeno-associated virus (AAV) use (increase from 4.9% in 2012 to 7.6% 2018) and adenovirus is the most commonly used viral vector seen in clinical trials (20.5% of clinical trials, however numbers are declining slightly)[5]. Adenovirus usage tops the charts

due to its superb capabilities to transfect cells with high efficiency, regardless of which part of the cell-cycle the cells reside[5]. However, the move towards AAV vectors allows for the delivery of larger genes to target cells, up to 35 kb, which is one of the major drawbacks of viral-mediated delivery, a limited cargo size[5]. Additionally, viral vectors have severe drawbacks in terms of immunogenicity, or the triggering of an immune response upon cell reinfusion, which raises red flags in terms of the safety of the therapy[11-13]. However, the fact that viral-mediated delivery raises health concerns is not biggest issue with this technology, rather the cost to manufacture these viral packages. This is an exhaustive process that requires highly trained personnel in a separate cGMP manufacturing facility, followed by extensive quality assurance testing, leading to an estimate of 10s of thousands of dollars in total added to the overall cost of the cell therapy[3].

1.3.2 Biochemical

Due the major drawbacks of viral-mediated delivery, additional R&D efforts are being put forth to develop technologies to alleviate these concerns. One of these technologies is another carrier-mediated approach, taking advantage of cellular biochemical pathways to package and deliver exogenous material to biological cells. This non-viral approach encompasses many technologies both synthetic and biologically based, in which the molecular payload, typically nucleic acids, is encapsulated by the carrier. These carriers can be lipid-based, synthetic polymers, inorganic nanomaterials (with and without ligand functionalization or cell penetrating peptides), and biological cell ghosts (dead cells whose cytoplasm is replaced with cargo)[11,14-15]. One thing these methods have in common is their reliance and promotion of cell membrane fusion and/or endocytosis of the carrier-package, followed by the endosomal escape/release of the material to be delivered[16-18]. Though these

technologies have been under development for decades, they currently still have several drawbacks, preventing its adoption as the preferable delivery modality in a clinical setting. The limitations of non-viral, biochemical-based delivery mechanisms include efficiency, cell type dependence, cargo flexibility, and manufacturing costs[11]. Since the majority of these technologies are endocytosis dependent, they tend to have low delivery efficiencies, with some technologies only achieving a 1% successful endosomal escape rate[19]. In addition to the low delivery efficiency, the material used as the carrier has also shown to be an important factor, as cellular toxicity needs to be taken into consideration[19-20]. Since this technology relies on the biochemical activation of endocytosis, this limits the cell types capable of targeting. Most importantly, most blood/immune cell types typically used in cell therapies are not easily targeted using these biochemical methods[21-22]. From a chemistry standpoint, potential cargo materials will vary in properties, such as charge, size, hydrophobicity, composition, etc. This variation may require the development of a specific carrier material for each cargo application, as this technology requires both the carrier material and the cargo to be compatible to form the complex[11]. Lastly, similar to viral-mediated delivery, the manufacturing of these biochemical carriers is laborious, uses expensive reagents, and requires highly trained personnel to carry out the synthesis, all of which making this delivery modality costly in its preparation and manufacturing[11].

1.3.3 Physical

Similar to the non-viral carrier mediated or biochemical delivery modality, physical-based or membrane disruption mediated delivery includes a number of different technologies, each of which embodied with their own pro's/con's, however, all of which are 'lumped' together for consideration in **Figure 1.3**. Physical-based delivery technologies include

microinjection, osmotic pressure driven, electroporation, optoporation, sonoporation, and cell squeezing technologies to physically disrupt the cell membrane to allow for molecular delivery[11]. Due to the nature of this delivery mechanism via physical manipulation of the cell membrane, these technologies are advantageous compared to biochemical methods, as they are cell type independent[23-24]. However, on the flipside, viability is a large concern, as the physical nature can lead to excessive cell damage following treatment[11]. In the case of electroporation, which will be discussed in much greater detail in the following chapter, it involves the application of electric fields across the cell membrane to cause pore formation so that treatment protocols require high levels of optimization for each cell type to maximize both the delivery efficiency and cell viability[25]. If the treatment procedure is too weak, a low number of cells will be transfected, while the resulting viability will remain high. If the treatment is too harsh, a large number of cells will be irreversibly damaged and die off. Once optimized though, this method can operate at high efficiencies and is not limited in terms of the cargo it can deliver. Recent advances in gene editing technologies, such as CRISPR (Clustered Regularly Interspaced Short Palindromic Repeats), require the capability to deliver large molecules to cells of interest, in which case electroporation has been noted as the preferred method of delivery to achieve good outcomes[26-29]. Another major advantage of using physical based deliveries is the cost associated with them. This method does not require costly manufacturing procedures and only the one-time purchase of the necessary equipment to carry out the physical nature of the delivery (i.e. pulse generator for electroporation)[25].

1.4 Motivation for Smart Electroporation Technology

Comparing the delivery technologies currently available, none are mature enough to be considered ideal or the preferred method. However, accounting for some of the main concerns associated with each viral, biochemical, and physical techniques, this work involves the further development of electroporation technology, with the goals of addressing the issues of efficiency and protocol development. To do this, the technology utilizes micro-scale fabrication techniques, to develop a microfluidic, flow through system, capable of performing highly controlled, electrically-triggered, single-cell level DNA transfections in which the degree of cell membrane permeabilization during the electroporation process can be monitored electrically (**Figure 1.4**).

Single-cell level electroporation on the micro-scale is no longer a novel concept, and has been previously performed in 2 separate regimes, either static cell systems or flow through devices. Both of these having their own advantages and disadvantages. Static cell systems allow for high level interrogations of the physical status of the cell membrane, i.e. monitoring that the electroporation event has taken place. However, due to the nature of being a static system, the throughput of these systems is extremely low[30]. Flow through micro-devices has the opposite concerns. In these systems, cells continuously traverse through a micro-device containing a set of electroporation electrodes, such that the molecular delivery is performed in a continuous fashion, enhancing the throughput of micro-electroporation devices. However, current devices are incapable of electrically monitoring the onset of electroporation, and thus these devices/systems still require the empirical derivation of electroporation protocols[31]. In this thesis work, a technology has been developed that combines both approaches. The device can monitor the physical state

of the cell membrane (i.e. whether the cell has undergone electroporation), in a continuous, serial fashion. The result is a device capable of performing highly controlled molecular delivery in a high throughput manner. Ultimately, this technology will eliminate the tediousness of empirically deriving electroporation protocols and will be able to account for cell-to-cell variability amongst a population, making this technology attractive for both precious cell types and hard to transfect cells.

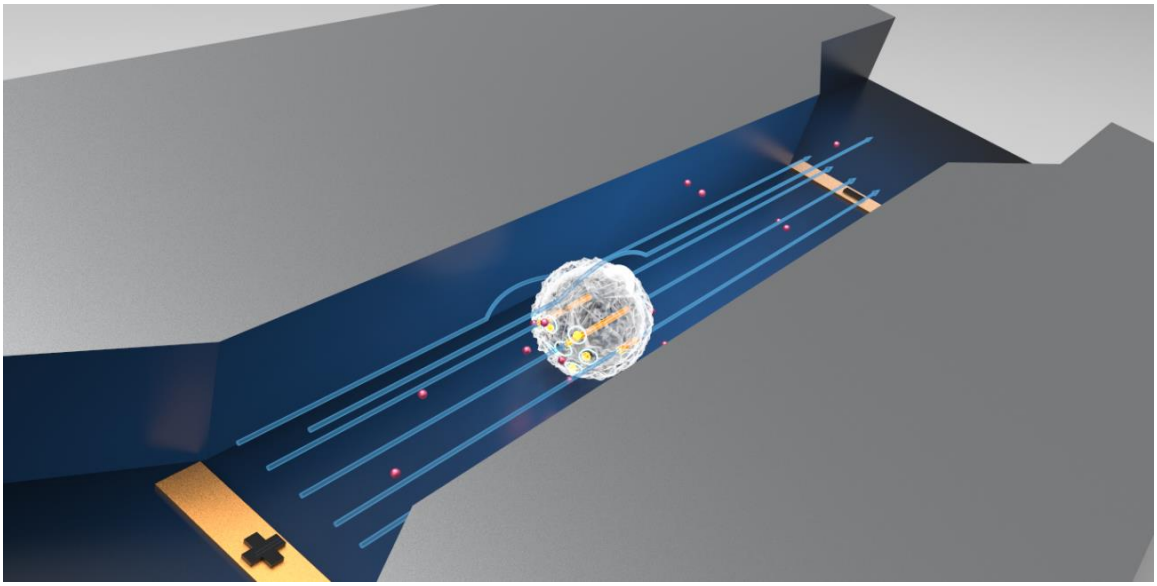

Figure 1.4 Illustration depicting smart electroporation technology. Cell entrance between the electrodes is detected, triggering an electric pulse to be applied. The degree of membrane permeabilization can be controlled and monitored throughout the electroporation process.

1.5 Thesis Overview

This thesis has the common theme of improving electroporation outcomes, however, 2 different approaches are followed to do so. The main goal of this thesis is the development of a microfluidic technology capable of acting as a biosensor to help improve both resulting cell viability and electro-transfection efficiency. This is done by electrically monitoring the degree of cell membrane permeabilization at the resolution of a single cell following the application of an electroporation pulse. Secondly, utilizing a bulk electroporation platform, different molecular compositions of electroporation buffer (the solution cells are resuspended in for the duration of the electroporation procedure) were explored. This work shows the importance of optimizing the electroporation buffer to promote good electroporation outcomes and suggests the biological mechanisms at play that affect viability and electro-transfection efficiency.

Chapter 1 of this thesis introduces the rapidly growing field of gene and cell therapies, in particular on the production of patient-derived cell therapies, such as CAR-T cell therapy. These therapies rely on the ability to effectively deliver genetic material to immune cells *ex vivo*, in which case an 'ideal' *ex vivo* delivery system is described based on various parameters required for a technology to succeed in a clinical setting. Following this description, each of the existing categories currently available to perform the intra-cellular delivery are broadly introduced and discussed upon as to where they stand as the ideal *ex vivo* delivery technology. Lastly, the motivation for this research thesis is introduced and the argument is made for this electroporation technology to improve upon the existing electroporation technologies currently available.

Chapter 2 of this thesis introduces and defines the concept of electroporation from both a biophysical and biochemical perspective, in much greater detail than what is referenced in chapter 1. A brief review of the various applications that electroporation is used for will be explored, ending on the application relevant to this thesis, which is *in vitro/ex vivo* reversible electroporation. The two categories of reversible electroporation will be discussed, macro-scale and micro-scale, and the major works from the literature contributing to the hypothesis for the micro-scale work will be introduced. Finally, the last section describes the different experimental parameters that can affect the outcomes of electroporation procedures and what those effects are.

Chapter 3 involves a large body of research utilizing macro-scale or bulk electroporation to showcase the effect that different molecular compositions of electroporation buffer have on the resulting electroporation outcomes, i.e. cell viability and electro-transfection efficiency. Much detail goes into discussing the background and importance of the work as well as the experimental design. The results focus on showing the effects that both electroporation pulse energy and different ionic contents in the buffer have on cell viability and electro-transfection efficiency. The discussion centers around the role that Mg^{2+} ions play in the electroporation process, how this ion preserves cell viability and hinders electro-transfection efficiency. Different biochemical/enzymatic mechanisms are speculated upon for these effects and supporting evidence for the role that ATPase membrane ion transporters play in cell recovery is shown/discussed. Lastly, a rating system is introduced, termed the electroporation outcome score, to distinguish which buffers/pulsing conditions achieves the best outcomes. A major takeaway from this study is that Mg^{2+} concentration should be optimized in electroporation buffer to improve outcomes. Future studies are

introduced, expanding to both more electroporation buffer compositions and cell types to be tested.

Chapter 4 re-introduces the microfluidic technology. The study and experimental design are introduced, with a focus on the microfabrication and experimental set-up. In this work several electroporation parameters were studied, and the electrical response of the cell membrane was recorded. An electrical metric was created to represent the degree of cell membrane permeabilization. In order to validate that this technology was capable of electrically monitoring the degree of membrane permeabilization, an optical study was performed utilizing propidium iodide, a live/dead cell stain that is impermeable to an intact cell membrane and fluoresces upon binding to nucleic acid. The fluorescence signal was shown to be strongly correlated to the electrical signal, indicating the technology's capabilities of electrically monitoring electroporation events.

Chapter 5 focuses on using this technology for a more clinically relevant application, plasmid DNA transfection encoding for green fluorescent protein. The chapter shows the evolution of the technology, explaining microfluidic device changes as well as hardware improvements. Like chapter 4, major results from chapter 5 include correlating the electrical response of the cell to the resulting cell viability, electro-transfection efficiency, and the applied pulse electrical energy. Additionally, the same scoring metric introduced in chapter 3 (electroporation outcome score), is correlated with both the applied pulse energy and the electrical response of the cell, or the degree of membrane permeabilization. What is found is an optimization curve, showing that to achieve both high cell viability and high electro-transfection efficiency there exists a finite region of cell membrane permeabilization in which this can be achieved. This result highlights the ability of this

technology to serve as a biosensor to aid in the optimization of electroporation protocols. Finally, future directions are introduced which speak on expanding the data set, to include more cell types.

Chapter 6 focuses on the state of the art in terms of the detection software and introduces the idea of a closed-loop, feedback-controlled electroporation device. Such a device would be able to perform electroporation of single cells with the highest level of control, accounting for the intrinsic variability amongst a cell population. A software algorithm capable of performing this level of control is introduced as well as various bottlenecks and alternative approaches to achieve this goal are in the conclusion/future directions.

Chapter 7 is a thesis summary chapter. This will be a summary of the main takeaways from chapter 3 thru chapter 6. As well as introduce preliminary results to be used in future studies.

1.6 Chapter References

1. FDA. What is Gene Therapy? 2018. Retried from: https://www.fda.gov/vaccines-blood-biologics/cellular-gene-therapy-products/what-gene-therapy
2. U.S. Department of Health and Human Services, Food and Drug Administration, Center for Biologics Evaluation and Research. Long Term Follow-Up After Administration of Human Gene Therapy Products, Draft Guidance for Industry. 2018, 1-32.
3. Vormittag, P., *et al.* A guide to manufacturing CAR T cell therapies. *Current Opinion in Biotechnology*, 2018, **53**, 164-181.
4. Zheng, P., Kros, J.M., & Li, J. Approved CAR T cell therapies: ice bucket challenges on glaring safety risks and long-term impacts. *Drug Discovery Today*, 2018, **23(6)**, 1175-1182.
5. Ginn, S.L., *et al.* Gene therapy clinical trials worldwide to 2017: An update. *Journal of Gene Medicine*, 2018, **20**, 1-16.
6. Tang, J., *et al.* The global landscape of cancer cell therapy. *Nature Reviews Drug Discovery*, 2018, **17**, 465-466.
7. Engstad, C.S., Gutteberg, T.J., & Osterud, B. Modulation of blood cell activation by four commonly used anticoagulants. *Thromb Haemost*, 1997, **77(4)**, 690-696.
8. Fesnak, A., *et al*. CAR-T cell therapies from the transfusion medicine perspective. *Transfus Med Rev*, 2016, **30**, 139-145.
9. Chen, L. & Files, D.B. Molecular mechanisms of T cell co-stimulation and co-inhibition. *Nat Rev Immunol*, 2013, **13**, 227-242.
10. Levine, B.L. Performance-enhancing drugs: design and production of redirected chimeric antigen receptor (CAR) T cells. *Cancer Gene Therapy*, 2015, **22**, 79-84.
11. Stewart, M.P., *et al*. *In vitro* and *ex vivo* strategies for intracellular delivey. *Nature*, 2016, **538**, 183-192.
12. Woods, N., *et al*. Lentiviral vector transduction of NOD / SCID repopulating cells results in multiple vector integrations per transduced cell : risk of insertional mutagenesis. *Blood*, 2003, **101**, 1284–1289.
13. Kim, T. K. & Eberwine, J. H. Mammalian cell transfection: the present and the future. *Anal. Bioanal. Chem*., 2010, **397**, 3173–3178.
14. Yin, H., *et al.* Non-viral vectors for gene-based therapy. *Nature Reviews Genetics*, 2014, **15**, 541-555.
15. Yoo, J., *et al*. Bio-inspired, bioengineered and biomimetic drug delivery carriers. *Nature Reviews Drug Discovery*, 2011, **10**, 521-535.
16. Khalil, I.A., *et al.* Uptake pathways and subsequent intracellular trafficking in nonviral gene delivery. *Pharmacol. Rev.*, 2006, **58**, 32-45.
17. Sahay, G., Alakhova, D.Y., & Kabanov, A.V. Endocytosis of nanomedicines. *J. Control. Release*, 2010, **145**, 182-195.
18. Stewart, M.P., *et al.* Challenges in carrier-mediated intracellular delivery: moving beyond endosomal barriers. *Wiley Interdiscip. Rev. Nanomed. Nanobiotechnol.*, 2016, **8**, 465-478.
19. Gilleron, J., *et al.* Image-based analysis of lipid nanoparticle-mediated siRNA delivery, intracellular trafficking and endosomal escape. *Nat. Biotechnol.*, 2013, **31**, 638-646.

20. Lv, H., *et al.* Toxicity of cationic lipids and cationic polymers in gene delivery. *Journal of Controlled Release*, 2006, **114**, 100-109.
21. Peer, D. A daunting task: manipulating leuokocyte function with RNAi. *Immunol. Rev.* 2013, **253**, 185-197.
22. He, W., *et al.* Discovery of siRNA lipid nanoparticles to transfect suspension leukemia cells and provide *in vivo* delivery capability. *Mol. Ther.*, 2014, **22**, 359-370.
23. Van Meirvenne, S., *et al.* Efficient genetic modification of murine dendritic cells by electroporation with mRNA. *Cancer Gene Ther.*, 2002, **9**, 787-797.
24. Clauss, J., *et al.* Efficient Non-Viral T-Cell Engineering by Sleeping Beauty Minicircles Diminishing DNA Toxicity and miRNAs Silencing the Endogenous T-Cell Receptors. *Human Gene Therapy*, 2018, **29(5)**, 569-584.
25. Zheng, M., *et al.* Continuous-flow, electrically-triggered, single cell-level electroporation. *Technology*, 2017, **5**, 31-41.
26. Schumann, K., *et al.* Generation of knock-in primary human T cells using Cas9 ribonucleoproteins. *Proc. Natl. Acad. Sci.* 2015, **112(33)**, 10437-1-442.
27. Rupp, L.J., *et al.* CRISPR/Cas9-mediated PD-1 disruption enhances anti-tumor efficacy of human chimeric antigen receptor T cells. *Nature Scientific Reports.* 2017, **7**, 1-10.
28. Macleod, D.T., *et al.* Integration of a CD19 CAR into the TCR Alpha Chain Locus Streamlines Production of Allogeneic Gene-Edited CAR T cells. *Molecular Therapy*, 2017, **25(4)**, 949-961.
29. Roth, T.L, *et al.* Reprogramming human T cell function and specificity with non-viral genome targeting. *Nature*, 2018, **559**, 405-409.
30. Khine, M., *et al.* Single-cell electroporation arrays with real-time monitoring and feedback control. *Lab on a Chip*, 2007, **7**, 457-462.
31. Hsi, P., *et al.* Acoustophoretic rapid media exchange and continuous-flow electrotransfection of primary human T cells for applications in automated cellular therapy manufacturing. *Lab on a Chip*, 2019, **19**, 2978-2992.

Chapter 2

Overview of Electroporation

2.1 What is Electroporation

Electroporation, also referred to as electropermeabilization, is a non-viral, electro-physical method to gain access to the intracellular space for the exogenous delivery of material, such as DNA, RNA, proteins, or drugs. Through the application of an external electric field, of appropriate strength and duration, an enhanced permeability of the membrane is achieved, via the formation of transient, aqueous pores, to allow delivery of otherwise impermeable materials (**Figure 2.1**)[1]. The term electroporation was first coined in a 1982 study by *Neumann et al.* "Gene transfer into mouse lyoma cells by electroporation in high electric fields", however, it is believed that the use of electric fields to deliver materials to

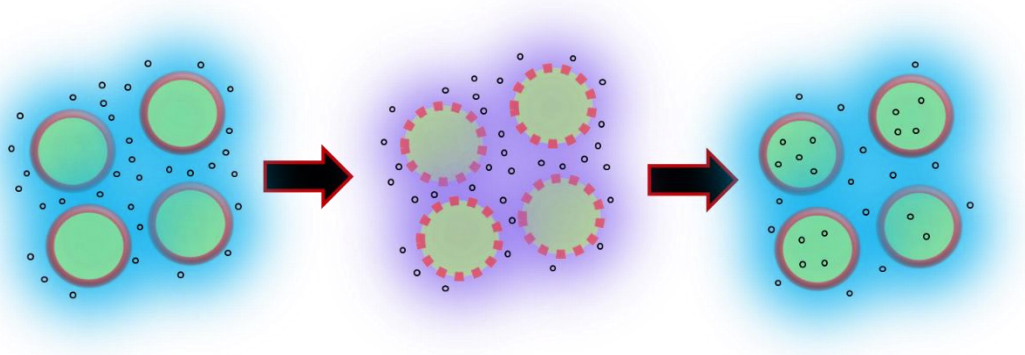

Figure 2.1 Electroporation Procedure. (Left) Cells in suspension with drug molecule. (Middle) Application of electric field, permeabilizing the cell membrane. (Right) Cell membrane resealing following drug delivery.

biological cells pre-dates this study[2,3]. Regardless, following this monumental study, many efforts have been put forth to understand and explain the biophysical and biochemical nature of this phenomenon.

The cell membrane, primarily composed of hydrophobic lipids, acts as an insulative barrier, compartmentalizing the cytosol from the extracellular environment, and separating two ionic mediums (i.e. intracellular vs extracellular). This separation of charge gives rise to a concentration gradient of charge on either side of the membrane which generates a resting membrane potential. This resting membrane potential will vary based on cell types but is typically in the range of -50 to -70 mV[4-6]. Upon the application of an external electric field, this ionic gradient changes, causing various degrees of polarization to occur the membrane of the cell (**Figure 2.2A**), resulting in a new transmembrane potential (TMV). When the TMV surpasses a cell-type specific threshold, the cell membrane undergoes kinetic rearrangement in the form of aqueous-pore formation, i.e. electroporation. This phenomenon has been explained/derived mathematically via solving the Laplace equations, assuming a dielectric shell of wall thickness *d*, resulting in the following equation for the TMV[6]:

$$\Delta TMV(M,t) = f \times g(\lambda) \times E \times r \times \cos(\theta) \times (1 - e^{-t/\tau}) \quad (1)$$

Where the $\Delta TMV(M,t)$ term is the change in transmembrane potential at point *M* on the cell membrane at time *t*, E is the applied electric field strength, r is the radius of the cell, θ is the angle between the direction of the electric field and the normal to point M on the membrane, *f* is a factor related to the shape of the cell (*f* = 1.5 for spherical cells), $g(\lambda)$ is a factor accounting for the conductivities of the membrane (λ_m), the intracellular medium (λ_i), and the extracellular medium (λ_e). Since the cell membrane is not a pure dielectric, i.e.

it is leaky capacitor, assuming a spherical cell with membrane thickness, *d*, and cell radius, *r*, the g factor can be defined as:

$$g(\lambda) = \frac{[(2\times\lambda_i\times\lambda_e)(d/r)]}{[\lambda_m\times(\lambda_i + 2\times\lambda_e) + 2\times(d/r)(\lambda_i - \lambda_m)(\lambda_e - \lambda_m)]} \quad (2)$$

Since the membrane conductivity is much less than both the intracellular and extracellular conductivities, $g(\lambda) \approx 1$. The final term, τ, is the charging time of the cell membrane (which acts as a capacitor). This value is extremely small, on the order of ~ μs, which, relative to the typical electroporation pulse duration (~ ms timescale), renders the exponential term negligible. Thus, the equation can be simplified to:

$$\Delta TMV(M,t) = 1.5\times E\times r\times\cos(\theta) \quad (3)$$

It is easy to decipher that the most important factors dictating the change in TMV are the electric field, the cell size, and the location along the membrane. From this relationship, there exists an inverse relationship between the applied electric field and cell size, i.e. larger cells will require lower levels of applied electric fields to porate and smaller cells require higher levels of applied electric fields to achieve electroporation. This is especially evident when comparing mammalian cells to bacterial cells which can be easily distinguished due to the size difference. Mammalian cells (typically ranging from ~ 10 μm to 30 μm in diameter) surpass the electroporation TMV threshold at ~ 1kV/cm field strengths, whereas bacterial cells (~ 1 μm to 3 μm in diameter) require higher applied field strengths, ~6 kV/cm[6]. The angle dependence also leads to some interesting phenomenon. The cosine term is at maximum when the angle between the electric field and cell membrane is 0° or 180°, which are the polar regions of the membrane facing the electrodes, and where we see the highest degree of membrane permeabilization. Due to the negative resting membrane

potential of cells, an asymmetric pattern of membrane permeabilization occurs. The portion of the membrane closest to the positive electrode (anode) becomes hyperpolarized,

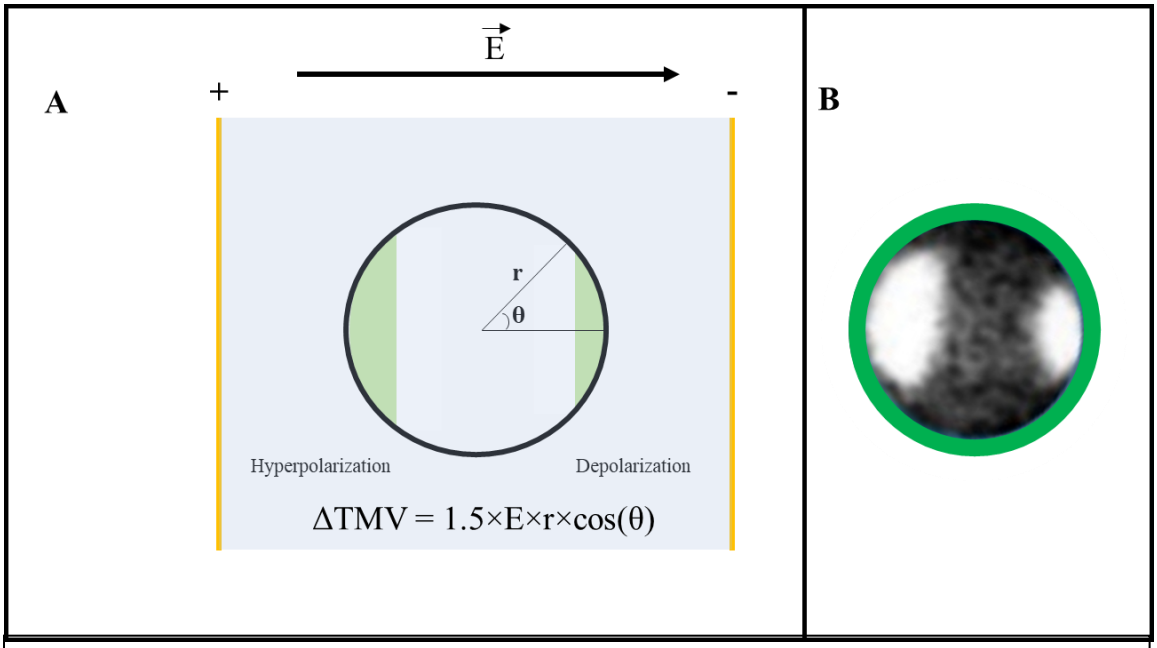

Figure 2.2 Electroporation Schematic. (A) Schematic illustrating a cell in a uniform electric field, noting what portions of the cell membrane surpass the transmembrane potential, resulting in an electroporated region of membrane (green). (B) Experimental result of m3T3 cells electroporated in presence of propidium iodide (PI). PI fluorescence shows the hyperpolarization and depolarization asymmetric phenomena that occurs during electroporation.

resulting in a higher degree of membrane permeabilization compared to the opposite side, closest to the negative electrode (cathode) which is simply depolarized[6]. This asymmetric permeabilization can be seen in **Figure 2.2B**, where a common fluorescent marker indicating membrane permeabilization, propidium iodide (PI), is used.

PI is a chemical that is typically utilized in live/dead cell staining protocols. This molecule is impermeable to an intact cell membrane (live cell), however, when the membrane is compromised (dead cell), PI can diffuse through where it irreversibly binds to free nucleic acids and begins to emit fluorescence (excitation/emission : 535nm/617nm) in far red wavelengths[7,8]. Since the cell membrane is compromised during electroporation, PI is a good indicator to determine the permeabilization percentage of a cell population and the degree of cell permeabilization of individual cells.

The most common nonbinding fluorophores used are membrane impermeant lucifer yellow (LY, 0.5 mM to 3.8 mM) and calcein (10 nM to 1 μM)[7]. Because these dyes do not 'turn on' their fluorescence upon delivery to the intracellular space, experimental designs must compensate for this with additional washing steps to eliminate any background noise[9]. However, a technique to eliminate the need for the wash step is to replace calcein with calcein-AM. In this case the fluorescent calcein molecule is attached to an acetoxymethyl ester group (AM), rendering the molecule non-fluorescent. With the addition of the AM group, calcein-AM becomes permeable to the cell membrane. Upon diffusion through the membrane, intracellular esterases cleave the AM group leaving the membrane impermeable, fluorescent calcein molecule inside the cell. Using this technique electroporation can then be studied by measuring the loss of fluorescence of a cell following pulse application (whereas with the nucleic acid binding fluorophores we see an increase in fluorescence)[10,11].

Both of these imaging techniques give insight as to whether or not cells have undergone electroporation, however, they do not provide any additional information such as cell viability. Ultimately, as a delivery technology, experimenters need to know whether or not

cells are going to survive the pulse applications, regardless of the degree of membrane permeabilization. The easiest method to do so is to perform a live/dead assay in conjunction with a permeabilization marker. These are typically done approximately hours after the electroporation experiments. It is worth noting that many of the permeabilization markers used in electroporation originally were designed to perform live/dead assays. Thus, it is of the utmost importance to ensure you rationally choose your markers for permeabilization and live/dead such that they do not have any overlap on their fluorescence spectrum. These experiments give insight into the overall cell viability, however, due to the nature of electroporation, in particular the resealing of the membrane, they are often deemed not 'true viability'. This is because the pore resealing time can range from seconds, to minutes, to hours, following the pulse application[5]. Therefore, a cell whose membrane has yet to reseal at the time of the live/dead stain will count negatively towards the viability even though the cell would have ultimately survived the procedure.

A better assay to gather information in regard to the success of electroporation experiments entails the delivery of larger fluorescent molecules or functional biological molecules (i.e. DNA or RNA). Fluorescein-Dextran (FD) is a common fluorescent molecule used in electroporation[7]. This molecule is a water-soluble, polysaccharide composed of various lengths of glucose polymers. The exact length of the glucose polymer will determine the molecular weight of the dextran, which typically range from 10^3 Daltons to 10^6 Daltons. Like the previously described electroporation molecules of interest, FD also does not have any clinical relevance other than acting as a delivery marker. However, because the size range is so large, FD can serve as a mimic to more expensive biological reagents such as proteins or DNA. In addition, FD also allows for a more comprehensive assay to be

performed on a cell population. Upon electrical pulse application, FD is delivered across the cell membrane. If the pulse strength is too large and the membrane does not reseal the FD will simply diffuse back into the medium the cells are located in. However, upon resealing of the membrane, FD is trapped inside the cytosol of the cell, which indicates that 1) the cell was permeabilized and 2) the cell is viable[12]. Similar in size to FD, biological molecules, such as DNA or RNA encoding for a fluorescent or luminescent protein, are commonly used in electroporation experiments[13].

The delivery of these molecules via electroporation is referred to as electro-transfection, where transfection is the deliberate introduction of nucleic acids into eukaryotic cells. Plasmid DNA (pDNA, ~ 1 ug/mL to 50 ug/mL), which is the primary indicator used in this thesis, will include the genetic instructions for the cells to produce a protein of interest. The most common proteins are luciferase and green fluorescent protein (GFP). Luciferase is an enzyme that upon administering its ligand, luciferin, an enzymatic reaction ensues causing bioluminescence, which can be detected. Whereas GFP is a protein that naturally fluoresces making it a good indicator of successful transfections and viability (dead cells will not produce the protein). Since these experiments rely on the cells' own machinery to transcribe the DNA into mRNA and then translate the mRNA into the protein of interest, the assay must wait enough time, ~24 hours, before delivery efficiency and viability can be determined. An alternative approach to decrease this time window is to eliminate the need for transcription by simply delivering mRNA directly to the cells. This allows for a much quicker time to determine the electro-transfection efficiency, on the order of hours. However, working with single-stranded RNA molecules instead of the double-stranded DNA molecules comes with its caveats. Most notably, RNA molecules are much less stable

and can be easily degraded which could give rise to experimental variability and an increased level of care / experimental design should be used when transfecting mRNA.

All of these molecules described should not be considered an all-inclusive list of the chemical / biochemical markers used to detect electroporation, electro-transfection, and cell viability. Rather they are some of the more frequently used methods for doing so. In addition to the optical detection techniques described, another approach to detecting the event of electroporation stems from the physical nature of the process (hence the theory previously described). In which the changes to the cell membrane can be detected / measured electrically, to act as a 'bio-sensor' for monitoring the process of electroporation[7,14-18]. This detection method will be discussed in further detail in further chapters as it is a main focus to this thesis work.

2.1.1 Applications

As previously discussed in chapter 1, an application of electroporation is to perform the gene delivery step in the manufacturing process for cell therapy. Although this is the focus application for this thesis, there are many other applications that electroporation is used for. The majority of these applications fall under the same umbrella category as gene delivery for cell therapy production, that being intracellular delivery via reversible electroporation. Where reversible electroporation is referring to the delivery of molecules followed by the membrane resealing, resulting in a viable cell with a successful delivery outcome. Additional applications for *ex vivo* reversible electroporation include the testing of RNA interference therapies, genomic editing via CRISPR-Cas9, and regenerative medicine / stem cell reprogramming[19]. All of these applications stem from the ability to

successfully transfect cells with nucleic acids (DNA/RNA). However, electroporation is not limited to *ex vivo* applications.

In vivo applications include the use of either transdermal, intra-dermal, or intra-muscular electrodes to delivery molecules of interest, such as DNA for vaccinations, to tissues of interest[20]. Another application relying on reversible electroporation of *in vivo* tissue is electro-chemotherapy (ECT). ECT involves the application of electric fields to patients' cancer tissues in conjunction with administration of chemotherapeutic agents, increasing the overall delivery efficiency, resulting in higher amounts of cancer cell death[20]. If electric fields strengths are further increased, the results transition away from reversible electroporation into irreversible electroporation.

Irreversible electroporation, as can be inferred, is when cells cannot recover following the pulse administration, resulting in cell death[20]. This realm of electroporation also has its applications. In *ex vivo* settings, irreversible electroporation can be used for cell lysis, allowing for the analysis of intracellular proteins, RNA, or DNA[21]. Electroporation-caused lysis is also used in the food/biotechnology industry for improved extraction of relevant molecules in food/beverage production, such as polyphenol extraction in red winemaking[22]. However, irreversible electroporation is much more common in *in vivo* settings. In a similar fashion to ECT, irreversible electroporation can be used to perform tissue ablation of tumors[23]. Such electric field parameters can be chosen to kill off cancer cells, while leaving surrounding tissues and constructs unharmed. This is a specialized sub-class of electroporation known as non-thermal irreversible electroporation[24] where no thermal damage occurs in the surrounding healthy patient tissues. In addition to treating tumors, non-thermal irreversible electroporation is also used in the ablation of cardiac

tissues, as is sometimes necessary for individuals suffering from atrial fibrillation, as well as promoting wound healing in burn victims via reducing scar tissue formation[25,26].

These applications give a brief oversight of the versatility of applied electric fields throughout many different facets of biomedical research, clinical research, and food and biotechnology. However, as mentioned, the focus of this thesis is on reversible electroporation in an *in vitro* / *ex vivo* setting to perform clinically relevant pDNA transfections. Throughout this work, different approaches have been investigated to study various parameters that affect the outcomes of electroporation experiments. In particular, bulk, cuvette-based electroporation was used to study the effects of electroporation buffers and a micro-electroporation device was designed to improve on outcomes. The following section will discuss macro-scale and micro-scale electroporation in more details.

2.1.2 Macro versus Micro

Current trends in the development of electroporation-based biotechnologies to advance both clinical and biomedical research are being performed primarily on two separate fronts, macro-scale and micro-scale level devices. Macro-scale electroporation devices are large, benchtop apparatuses, capable of processing large cell numbers per experimental run (10^6—10^9 cells). To do this, cells are typically resuspended is a fixed volume, containing the delivery molecule of interest, and transferred to an electroporation cuvette (**Figure 2.3A**)[13]. This cuvette is then inserted into the macro electroporation device (**Figure 2.3B**) which is electrically connected to the pulse generator (**Figure 2.3C**). A pulse is programmed by the user and applied to the cell suspension. Though the high cell number capability of macro-scale electroporation platforms (see **Appendix A** for a list of cuvette-based electroporation technologies) is highly desirable in a clinical setting, there are some

major concerns surrounding the use of these technologies. Due to the large size scale of the disposable cuvettes, which typically have electrodes spaced 1 mm, 2 mm, or 4 mm, apart, the voltage requirements necessary to achieve efficient levels of electroporation are on the order of 100's to 1000's of Volts. This requirement results in high levels of Joule heating within the solution as well as the formation of electrolysis bubbles, indicating an electro-chemical reaction has taken place at the electrode-electrolyte interface. These factors are known to have downstream effects on the resulting cell viability and cell recovery. In addition, the high voltage requirement in conjunction with high levels of user interaction to perform the procedure, poses a safety risk to the individual[27].

To alleviate some of this risk as well as eliminate the need for user-handling in the electroporation process, flow-through devices have been developed to allow for an automated electroporation process. To date, the systems that can perform high throughput, flow through electroporation are produced by MaxCyte and Miltenyi Biotec. The MaxCyte technology can process large cell numbers in a short period of time, however, it is still a stand-alone platform technology in the sense that users are required to pre-load the system with their cell suspensions[28]. On the other hand, Miltenyi Biotec's CliniMACS Prodigy device is closed-tubing system, capable of performing all manufacturing steps currently involved in cell therapy production (**Figure 1.2**). Recently, an add-on dual pulse electroporation device has been developed and integrated into the Prodigy workflow[29]. Both of these systems are capable of handling large cell numbers per unit time via a batch, flow through electroporation process. This level of automation in desirable in a manufacturing setting, however, these systems do not eliminate all of the downsides of bulk, macro-scale electroporation. These systems still suffer from the usage of high voltage

pulse applications and all of macro-scale electroporation devices suffer from treating a large population of cells as a single entity, resulting in variability as each cell in the suspension has its own intrinsic biological properties and will experience different perturbations in local electric field strengths.

Taking advantage of the advancements in MEMs fabrications techniques, the field of BioMEMs (Biomedical Micro-Electro-Mechanical systems) has materialized. Also known as Lab-on-a-Chip (LOC) or µ-Total-Analysis-Systems (µTAS), this field involves the use and development of miniaturized technologies for the advancement of biomedical research. A subset of this vast field is the area of micro-electroporation technologies which take advantage of performing electroporation on the same size scale as the mammalian cells. This leads to a significant reduction in the voltage requirements necessary for electroporation events to occur, reducing both the amount of Joule heating occurring in the solution and the electrolytic reactions occurring at the electrode-electrolyte interface. The smaller size scale also provides a more uniform electric field when compared to macro-scale electroporation devices. This field uniformity allows for the interrogation of single cells, ensuring that each cell receives the prescribed electric pulse and eliminating some variability amongst a given cell population[27,30].

Typically, micro-electroporation technologies capable of performing single-cell level electroporation fall into two regimes, static-cell and flow-through devices. Each of these approaches has its own pros and cons. Static cell devices allow for higher levels of system control and the electrical interrogation of the event that electroporation has taken place. This electrical information can serve as an analogue to fluorescence markers, such as PI, as an indicator that membrane permeabilization has taken place. The electrical monitoring

of single-cell level electroporation was first shown in 2001, by the Rubinsky group. They developed a micro-device capable of trapping a single cell in a hole. This hole allowed for the passage of current between a set of electrodes. When the cell was present, and no electroporation pulse was applied, and no current could be sensed. However, after an electroporation pulse was applied to the cell, the ensuing pore formation through the cell membrane opened up a current path which was capable of being recorded (**Figure 2.4A**)[14]. Following this breakthrough, *Khine et al*. developed a LOC device in 2007 capable of trapping multiple cells in parallel all the while monitoring the electroporation events of each of them (**Figure 2.4B**)[15]. In this work, the idea of performing feedback-controlled electroporation was first introduced as the ability to deliver precisely the right amount of electrical energy to not over-permeabilize the cell membrane by monitoring the electrical signal after each pulse is administered until a desired change in current is reached. The capability to control the degree of membrane permeabilization across single cells within a population truly eliminates the intra-population variability that is intrinsic to macro-scale level electroporation. These technologies have been further advanced. In 2016 *Guo & Zhu* developed a parallelized array capable of positioning cells precisely between electrodes using negative dielectrophoretic forces. Once positioned, the static cells within the array can then be electroporated while being monitored electrically for the event of membrane permeabilization (**Figure 2.4C**)[16]. Another device developed by *Burgel et al.*, a pseudo-flow device, 'shuttles' a cell back and forth between a sensing and electroporating electrode using a flow inversion algorithm, all-the-while monitoring the impedance of the cell membrane during the process (**Figure 2.4G**)[17]. Although this device utilizes flow in its operation, the need to move a cell back and forth between electrodes does not translate to

high-throughput and this system can be considered ‘static’. These static single cell devices can gather valuable real-time information during the electroporation process, giving insight as to what pulsing conditions / protocols are required to perform efficient electroporation. However, the major drawback associated with these devices is the need for the cells to be static or trapped. This severely limits the overall throughput of these devices to levels that are undesirable in a clinical setting, thus preventing the mainstream adoption of these technologies.

To improve upon the low throughput associated with the static, single cell level micro-electroporation devices, some groups have developed flow through devices. In these setups, cell suspensions are continuously perfused through a microfluidic channel that is equipped with a set of electrodes (**Figure 2.3D**). The electrodes are either constantly biased with a DC voltage offset, such that the cell velocity will determine the pulse width, or are pulsed at a set frequency/duty cycle which matched with the cell velocity, determines the pulse width and pulse number applied to each cell in transit. In the case of a constant applied voltage, Chang Lu’s group has developed a microfluidic device capable of amplifying the local electric field strengths by adding constriction geometries into the microfluidic design, encompassed by the electrode set **Figure 2.4F**)[31]. This simple design eliminates the need for both a function generator and a high voltage power supply. Alternative micro-scale flow through electroporation systems utilize hydrodynamics to improve their electroporation outcomes. *Wei et al*. developed a hydrodynamic focusing devices where two sets of sheathing fluids ‘pinch’ the cell flow stream to the center of the channel. This feature allows for the cells to traverse through the electrode region of the device without ever encountering the electrode-electrolyte interface (**Figure 2.4H**)[32].

Zheng et al also developed a hydrodynamic-based flow through system, however, in this system a single sheath flow was used to push the cell flow against the wall of the microfluidic device causing the rotation of the cell along the wall. The rotating cell was then exposed to the electric pulse causing a more uniform permeabilization around the circumference of the cell membrane (**Figure 2.4E**)[33]. Recent works out of Draper Labs have further advanced flow through systems, combining acoustophoresis with micro-scale electroporation. In this device, cells are acoustically transferred from sheath flows, composed of cell media, into the center stream, composed of electroporation buffer. The cells are then electroporated and transferred back into the cell culture media. This system achieved cell throughputs of ~120,000 cells per minute (**Figure 2.4D**)[34]. Though this rate is great by microfluidic standards, it is still substantially lower than the commercial flow through counterpart MaxCyte which can handle billions of cells in a 30-minute time frame. However, by simply adding multiple channels in parallel, microfluidic throughputs can be enhanced to approach the requirements of a clinical setting.

The two branches of micro-scale electroporation platforms, static and flow through, demonstrate the possibilities that can be achieved by these devices. Each setup contains a highly desirable feature, with the static systems capable of performing electrical monitoring of electroporation events and flow through systems having the ability to process high cell counts per unit time. In this thesis, we look to bridge the gap between these two platforms, developing a technology capable of monitoring single cell electroporation events but in a serial, continuous flow fashion.

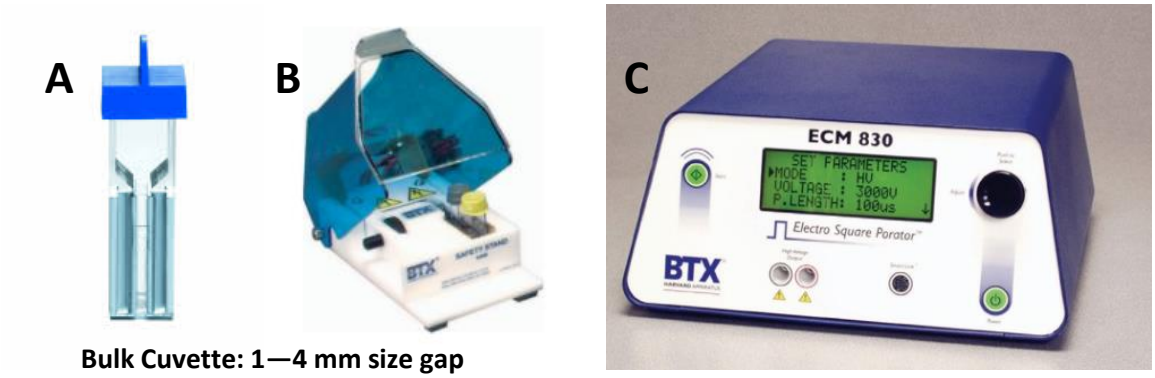

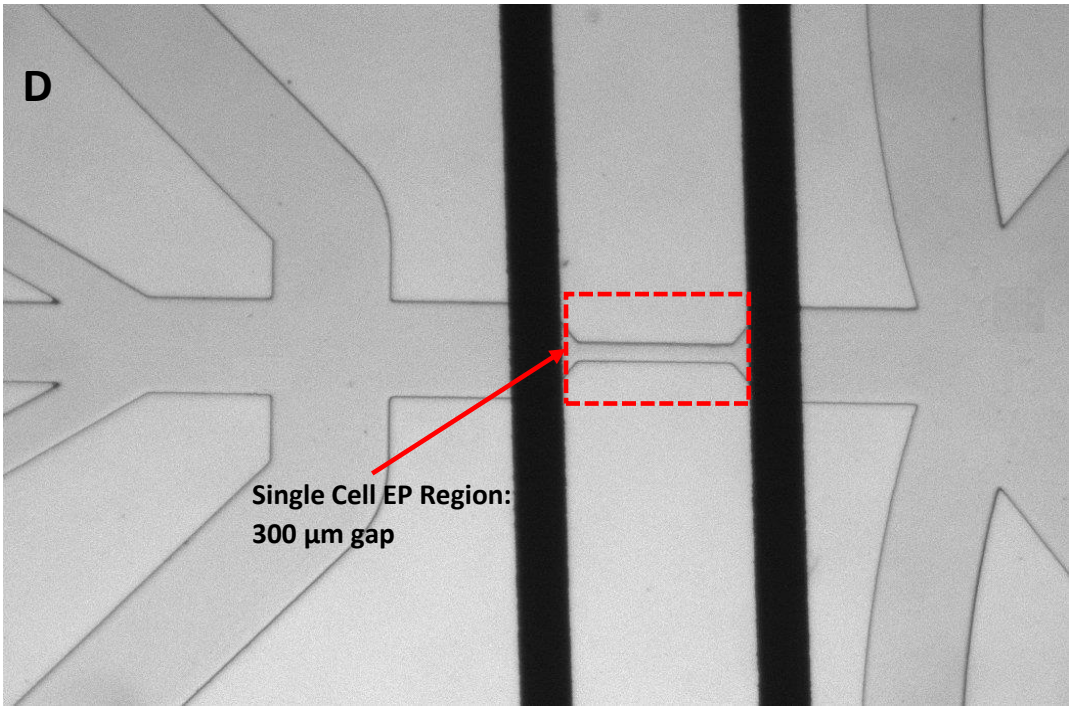

Figure 2.3 Examples of macro and micro electroporation systems. (Top Row, A-C) A standard cuvette-based, bulk EP setup, capable of electroporating cells on the order of 10^6 per mL. (A) Disposable cuvette, ranging from 1 to 4 mm gap sized between the planar electrodes. (B) Cuvette stand. (C) Harvard Apparatus square wave pulse generator. (D) Example of a micro electroporation device, capable of electroporating single cells in a continuous fashion.

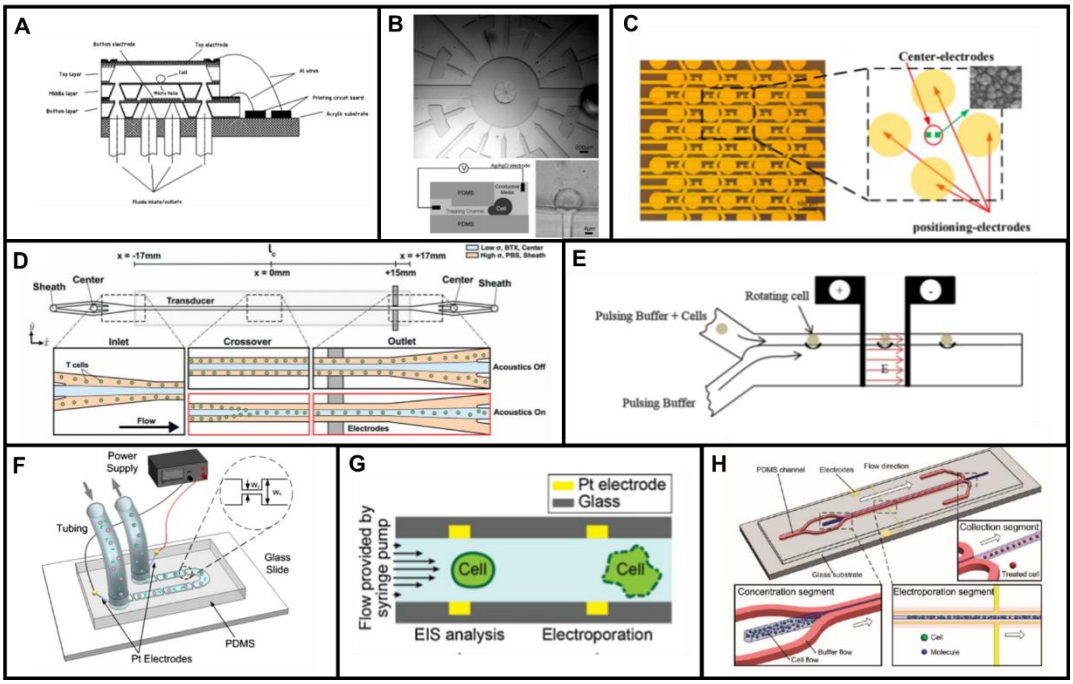

Figure 2.4. Illustrations of existing micro electroporation devices. (A) *Huang & Rubinsky, 2001*, (B) *Khine et al.*, 2007, (C) *Guo & Zhu, 2016*, (D) *Hsi et al.* (Draper Labs), *2019*, (E) *Zheng et al, 2016*, (F), *Wang & Lu, 2008*, (G) *Burgel et al, 2014*, (H) *Wei et al, 2011*.

2.2 Electroporation Parameters

Electroporation, like many experimental techniques, is accompanied by many experimental parameters that will need to be optimized for each application. **Figure 2.5** illustrates many of the parameters for running electroporation experiments. Things to consider when planning the experimental design include the (1) cell type, (2) cell density, (3) electrode size, geometry, material, (4) pulse shape and polarity, (5) pulse waveform, (6) 'drug' concentration, (7) electroporation buffer, (7.1) molecular composition, (7.2) ionic conductivity, (7.3) osmolality, (8) temperature, (9) upstream processing / conditioning, (10) downstream processing / recovery.

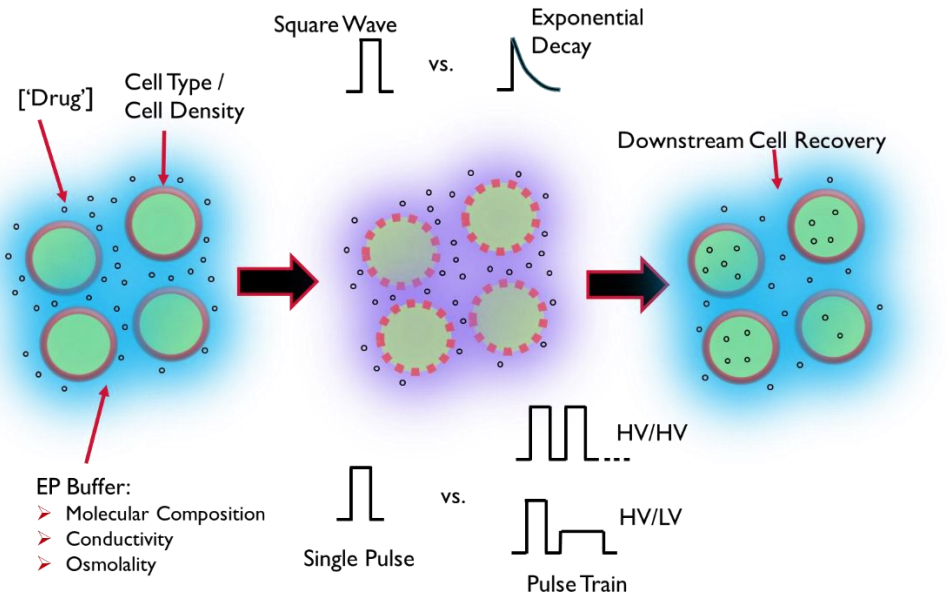

Figure 2.5 Experimental Parameters Affecting Electroporation. This illustration highlights some of the many experimental variables that can have significant effect on the outcome of electroporation-based delivery experiments.

(1) Cell Type—As was shown in equation 1 of this chapter, the physical phenomenon that dictates electroporation events is based on factors that are specific to each individual cell, i.e. cell size (radius) and membrane / intracellular conductivities. This means the properties that are intrinsic to a cell population and cells amongst that population are going to dictate the outcomes of electroporation experiments. In addition, when changing cell types in an experimental setting, one should note that all other experimental parameters will need to be re-addressed to optimize the electroporation outcome.

(2) Cell Density—The cell density, or the number of cells per unit volume, is an important factor to consider when planning electroporation experiments. Protocols typically suggest ~ 1 to 2 million cells per mL of electroporation buffer, however, this is dependent on the cell type. For bulk electroporation experiments, sub-optimal cell densities can have detrimental effects on the resulting cell viability and electro-transfection efficiency. Assuming proper pipetting technique resulting in a single-cell suspension, the localized electric field strengths will vary depending on the number of cells in suspension, recalling the cell membrane acts as an inhibitor. If the cell number is too high, the likelihood that some cells will experience a shielding effect from the applied electric field is increased, which will lead to a lower amount of transfection. In the case of having too few cells per unit volume, the opposite can occur, and more cells can experience too high of electric field strengths which can negatively affect the resulting cell viability. Similarly, in the microfluidic electroporation of single cells, cell density plays a vital role. With too high of a cell density, this increases

the likelihood that multiple cells can enter the electroporation region simultaneously. In the case of performing a high throughput, population-based feedback system (see Chapter 6), the cell density needs to be optimized to both allow for the correct electric field strengths to be administered (minimize the shield effect) while allowing for the maximum cell throughput.

(3) Electrode Size, Geometry and Material—The electrode configuration for the experimental set-up is important since the distance between them will dictate the voltage that is necessary to achieve the desired electric field strengths. Geometry variations in electrode design can lead to local enhancements in electric field strengths, as the electric field lines are going to condense where electrodes come to a point (such as corners, edges, etc.) This can be utilized to lower voltage requirements necessary for electroporation (i.e. using a saw-tooth pattern)[21]. The overall size of the electrodes in contact with the electrolyte solution (electroporation buffer) will dictate the current density experienced at the surface, with smaller surface areas leading to higher current densities. Higher current densities can more readily result in an electrolysis reaction to occur at the electrode surface, a highly undesirable event during electroporation, especially at the micro-scale. Lastly, the material used for electrodes is also going to affect the electrode-electrolyte interaction. An inert metal is preferred (such as gold or platinum) to minimize the degree of electrolytic reaction occurring at the interface as high voltages are applied to the electrodes during electroporation.

(4) Pulse Shape and Polarity—Typically, there exists two standard pulse shapes used to perform electroporation, square-wave and exponential decay[35]. Square-wave

pulses are traditionally used for mammalian cell transfection whereas exponential decay is the standard to perform electroporation of bacterial cells. The polarity of the pulse, i.e. which electrode is positive or negative, will determine 1) which region of the cell will be hyperpolarized and 2) the direction of the electrophoretic forces on either a positively charge molecule (PI) or a negatively charge molecule (DNA). Accounting for the charge of the molecule you wish to delivery, while taking advantage of the hyperpolarized region of the cell membrane may require switching the polarity of the pulse waveform[36].

(5) Pulse Waveform—The pulse waveform is similar to the pulse shape. However, it also includes information such as the strength of the pulse, the duration of the pulse, the number of pulses, the duty cycle of the pulse, and the pulsing scheme. The pulsing scheme, for instance, could be a train of the same pulse strength and duration at a set frequency, it can be a high voltage followed by a low voltage pulse (HV/LV), it can be a high voltage-short duration electroporation pulse (to permeabilize) followed by a low voltage-long duration electrophoretic drive-in pulse (to delivery material), an alternating polarity pulse train (to enhance DNA delivery), or any combination of these[12]. The exact pulse waveform will be optimized on a per cell type basis and should be well thought out considering the other variables affecting electroporation outcomes.

(6) ‘Drug’ Concentration—The ‘drug’ is referring to the material you wish to deliver. As previously discussed, this could be permeabilization indicators such as PI or DNA plasmids to perform transfections. The level of delivery or electro-transfection efficiency is going to be directly related to the ‘drug’ concentration,

with increased concentrations leading to increased amounts of delivery and electro-transfection efficiencies[7]. With increased levels of 'drugs', cell toxicity becomes a concern and should be considered when planning an experiment and determining the optimal starting concentration. In the case that functional cells are desired following the electroporation, the amount of cytotoxicity introduced must be minimized. It has been shown that increasing amounts of plasmid DNA can be detrimental to cellular viability when performing transfection on primary white blood cells, a prime target for cell therapies[37].

(7) Electroporation Buffer—Electroporation buffer will be discussed in much greater detail in chapter 3. Briefly, the molecular make-up of the electroporation buffer (the solution the cells are resuspended in for the duration of the electroporation pulse administration) can have a significant effect on the outcome of the experiment. 7.1) The exact molecular make-up of the buffer (all of the ingredients) is important because this will have an effect on the biochemical processes necessary to recover from the pulse application. 7.2) The overall conductivity of the solution, a result of the molecular make-up, will influence the current passing through the solution, and thus the amount of Joule heating that occurs during the pulse application. If a significant amount of heating occurs (when the conductivity is higher) this can cause damage to the cells in solution and negatively affect the resulting viability. 7.3) The osmolality of the solution will dictate the directionality of water movement across the cell membrane. The standard, physiological osmolality is ~300 mOsm. When solutions are hypo-osmotic solution (i.e. lower than 300 mOsm), this will cause an osmotic pressure

gradient and water molecules will move across the cell membrane to attempt to reach equilibrium, resulting in an increase in cell volume or cell swelling. In the opposite case, when cells are placed in a hyper-osmotic solution (i.e. greater than 300 mOsm) the osmotic pressure gradient is in the reverse direction, causing cells to lose volume and shrink. The swelling / shrinking of cells will affect the outcomes of the experiments and it is best practice to keep the cells in an iso-osmotic buffer (i.e. ~300 mOsm) keeping the osmotic gradient at equilibrium.

(8) Temperature—Though the conductivity of the electroporation buffer will affect the change in temperature of the solution during the pulse application due to Joule heating, the overall temperature during the entirety of the electroporation process should be considered. This is due to the intrinsic, thermodynamic nature of the electroporation process. There are contradictory results in the literature describing what the best temperature protocol is to optimize electroporation outcomes. For instance, one group has shown that pre-heating cells to above physiological temperatures prior to electroporation increases the electro-transfection efficiency[38]. Whereas, additional reports state that cells should be incubated on ice (4°C) prior to applying the electroporation pulses at room/physiological temperatures[39]. This approach is more widely adopted, and it is believed that the lower temperature allows for the negatively charged DNA to come into closer proximity to the negatively charged cell membrane[40]. Following pulse application cells should be transferred to the pre-heated (37°C) recovery media (see 10) and allowed to incubate before being analyzed for

electro-transfection efficiency. Due to the discrepancies, a temperature optimization experiment may be necessary for each cell type.

(9) Upstream Processing/Conditioning—The pre-electroporation temperature bias could be lumped into the category of upstream processing/conditioning for electroporation experiments. However, more broadly, this experimental parameter considers any of the processing steps that need optimized minutes/hours/days prior to running the electroporation procedure. The major process to consider in this category is the cell culturing. Typically, cells are to be passaged and plated approximately 24 hours prior to electroporation experiments. At the 24-hour time point, the cells should be at a density/confluency categorizing them as being in the exponential growth stage of cell culture[13]. The rationale behind this is to attempt to minimize the amount of variance within the cell population in respect to what stage the cells are in within the cell cycle[41]. Ultimately, this process is attempting to minimize variation in results due to this hard-to-control experimental variable. The manufacturing steps prior to gene delivery involved in cell therapy production in CAR-T generation would also be lumped into this category, albeit, they are very specific to that application. However, similar research areas could be investigated to improve electroporation outcomes via ‘conditioning’ the cells prior to pulse applications.

(10) Downstream Processing/Recovery—The downstream processing/recovery involves the optimization of the steps following electroporation pulse application. As with the previous parameter, this could include the temperature at which this stage is performed at, or it could refer to the various steps involved

in the CAR-T generation following gene delivery. However, to be more generalized to basic electroporation procedures, the most important parameter to fall under this category is the optimization of the cell recovery medium following electroporation. The most common change in the electroporation recovery medium is the lack of antibiotics[42]. Following electroporation, the cells' membranes are going to be compromised for an extended period of time (typical 'resealing' is on the order of seconds up to hours following pulse application). Due to this, antibiotics (such as penicillin and streptomycin) which are impermeable to mammalian cell membranes, are now capable of entering the cell following electroporation, resulting in toxic effects and decrease the resulting cell viability. Following 24 hours, antibiotics can safely be supplemented into the culture. The recovery media could also be supplemented with additional molecules to help cells recover from the electroporation trauma. Particularly, growth factors can be used to enhance the metabolic activity following electroporation. Evidence presented within this work in chapter 3 suggests the involvement of ATPase enzymes in the re-establishment of ionic homeostasis following electroporation. These enzymes require both Mg^{2+} and ATP to function. Thus, ensuring that the recovery media includes these molecules, an enhancement in cell viability would be expected. Furthermore, this parameter space has not been explored to the extent as the others, marking it for a prime target for future research exploration, with a primary focus from a biological/molecular biological and biochemical standpoint.

2.3 Chapter References

1. Bolhassani, A., Khavari, A. & Orafa, Z. Electroporation – Advantages and Drawbacks for Delivery of Drug, Gene and Vaccine. In Application of Nanotechnology in Drug Delivery. A.D. Sezer (**Ed.**). (2014), InTech, Rijeka, Croatia - EU.
2. Neumann, E., *et al.* Gene transfer into mouse lyoma cells by electroporation in high electric fields. *The EMBO Journal*. 1982, **7**, 841-845.
3. Deipolyi, A.R., *et al.* Irreversible electroporation: evolution of a laboratory technique in interventional oncology. *Diagn Interv Radiol*. 2014, **20**, 147-154.
4. Weaver, J.C. Electroporation: A General Phenomenon for Manipulating Cells and Tissues. *Journal of Cellular Biochemistry*. 1993, **51**, 426-435.
5. Kotnik T, *et al*. Membrane Electroporation and Electropermeabilization: Mechanisms and Models. *Annual Review of Biophysics*. 2019, **48**, 63–91.
6. Rosazza, C., *et al.* Gene Electrotransfer: A Mechanistic Perspective. *Current Gene Therapy.* 2016, **16**, 98-129.
7. Napotnik, T.B., & Miklavcic, D. In vitro electroporation detection methods—An overview. *Bioelectrochemistry*. 2018, **120**, 166-182.
8. Invitrogen Molecular Probes. Propidium Iodide Nucleic Acid Stain. 2006, MP01304.
9. Sozer, E.B., Pocetti, C.F., & Vernier, P.T. Asymmetric patterns of small molecule transport after nanosecond and microsecond electropermeabilization. *J. Membr. Biol.* 2018, **251**, 197-210.
10. Khine, M., *et al.* A single cell electroporaiton chip. *Lab on a Chip*. 2005, **5**, 38-43.
11. Grys, M., Madeja, Z., & Korohoda, W. Decreasing the thresholds for electroporation by sensitizing cells with local cationic anesthetics and substances that decrease the surface negative electric charge. *Cellular and Molecular Biology Letters.* 2014, **19**, 65–76.
12. Sadik, M. M. *et al.* Scaling relationship and optimization of double-pulse electroporation. *Biophysical Journal.* 2014, **106**, 801–812.
13. Sherba, J.J., *et al*. The effects of electroporation buffer composition on cell viability and electro-transfection efficiency. *Nature Scientific Reports,* 2020 **10**, 3053.
14. Huang, Y., & Rubinsky, B. Microfabricated electroporation chip for single cell membrane permeabilization. *Sensors and Actuators*, 2001, **89**, 242-249.
15. Khine, M., *et al*. Single-cell electroporation arrays with real-time monitoring and feedback control. *Lab-on-a-Chip*, 2007, **7**, 457–462.
16. Guo, X. & Zhu, R. Controllable in-situ cell electroporation with cell positioning and impedance monitoring using micro electrode array. *Scientific Reports*, 2016, **6**, 1-8.
17. Bürgel, S.C., *et al*. On-chip electroporation and impedance spectroscopy of single-cells. *Sensors and Actuators B: Chemistry*. 2015, **210**, 82–90.
18. Zheng, M. *et al.* Continuous-flow, electrically-triggered, single cell-level electroporation. *Technology*, 2017, **5**, 31–41.
19. Shi, J., *et al.* A Review on Electroporation-Based Intracellular Delivery. *Molecules.* 2018, **23**, 3044.

20. Yarmush, M., *et al.* Electroporation-Based Technologies for Medicine: Principles, Applications, and Challenges. *Annu. Rev. Biomed. Eng.* 2014, **16**, 295-320.
21. Lu, H., Schmidt, M.A. & Jensen, K.F. A microfluidic electroporation device for cell lysis. *Lab on a Chip*. 2005, **5**, 23–29.
22. Maza, M., *et al.* Thermal and Non-Thermal Physical Methods for Improving Polyphenol Extraction in Red Winemaking. *Beverages*. 2019, **5**, 47.
23. Rolong A., Rubinsky B., Davalos R.V. (2017) Tissue Ablation by Irreversible Electroporation. In: Miklavcic D. (eds) Handbook of Electroporation. Springer, Cham
24. Phillips, M., Maor, E., Rubinsky, B. Principles of Tissue Engineering With Nonthermal Irreversible Electroporaiton. *Journal of Heat Transfer*. 2011, **133**, 011004.
25. Lavee, J., *et al.* A Novel Nonthermal Energy Source for Surgical Epicardial Atrial Ablation: Irreversible Electroporation. *The Heart Surgery Forum*. 2007, **10**, 96-101.
26. Goldberg, A., *et al.* Preventing Scars after Injury with Partial Irreversible Electroporation. *Journal of Investigative Dermatology*. 2016, **136**, 2297-2304.
27. Geng, T., & Lu, C. Microfluidic electroporaiton of cellular analysis and delivery. *Lab on a Chip*. 2013, **13**, 3803.
28. Li, L., *et al.* Highly Efficient, Large Volume Flow Electroporation. *Technology in Cancer Research & Treatment.* 2002, **1**, 341-349.
29. Bruning, M., *et al.* Monocyte-derived dendritic cells (Mo-DCs) generated with CliniMACS Prodigy are functional and fulfill requirements for cancer vaccines. Poster.
30. Chang, L., *et al.* Micro-/nanoscale electroporation. *Lab on a Chip*. 2016, **16**, 4047-4062.
31. Wang, H., & Lu, C. Microfluidic Electroporation for Delivery of Small Molecules and Genes Into Cells Using a Common DC Power Supply. *Biotechnology & Bioengineering*. 2008, **100**, 579-586.
32. Wei, Z., *et al*. A Laminar Flow Electroporation System for Efficient DNA and siRNA Delivery. *Analytical Chemistry*. 2011, **83**, 5881-5887.
33. Zheng, M., *et al.* Hydrodynamically controlled cell rotation in an electroporation microchip to circumferentially deliver molecules into single cells. *Microfluidics & Nanofluidics,* 2016, **20**, 16.
34. His, P., *et al.* Acoustophoretic rapid media exchange and continuous-flow electrotransfection of primary human T cells for applications in automated cellular therapy manufacturing. *Lab on a Chip*. 2019, **19**, 2978.
35. Ng MM. Exclusive Compendium: Optimizing an Electroporation Protocol. *Harvard Bioscience Publication*. 2019, **1**, 1–17.
36. Rebersek, M., *et al*. Electroporator with automatic change of electric field direction improves gene electrotransfer *in-vitro*. *BioMedical Engineering OnLine*. 2007, **6**, 1-11.
37. Clauss, J., *et al.* Efficient Non-Viral T-Cell Engineering by Sleeping Beauty Minicircles Diminishing DNA Toxicity and miRNAs Silencing the Endogenous T-Cell Receptors. *Human Gene Therapy*. 2018, **29**, 569-584.

38. Rols, *et al.* Temperature effects on electrotransfection of mammalian cells. *Nucleic Acids Research.* 1994, **22**, 540.
39. Wu, M. & Yuan, F. Membrane Binding of Plasmid DNA and Endocytic Pathways Are Involved in Electrotransfection of Mammalian Cells. *PLOS ONE.* 2011, **6**, 1-9.
40. Mao, M. *et al.* Involvement of a Rac1-Dependent Macropinocytosis Pathway in Plasmid DNA Delivery by Electrotransfection. *Molecular Therapy*. 2017, **25**, 803-815.
41. Brunner, S., *et al.* Overcoming the Nuclear Barrier: Cell Cycle Independent Nonviral Gene Transfer with Linear Polyethylenimine or Electroporation. *Molecular Therapy*. 2002, **5**, 80-86.
42. Potter, H. & Heller, R. Transfection by Electroporation. *Curr Protoc Mol Biol.* 2003, **9**, 1-11.

Chapter 3

Effect of Electroporation Buffer on Electroporation Outcomes

3.1 Study Overview

In this chapter macro-scale level electroporation (BTX ECM 830) was used to explore the effects that electroporation buffer composition, pulse energy, and the relationship between these variables have on the electroporation outcomes of cell viability and electro-transfection efficiency. This work was published in *Nature Scientific Reports* in Feb 2020.

The supplementary information referred to in this chapter can be found in **Appendix B**.

Sherba, J.J., Hogquist, S., Lin, H., Shan, J.W., Shreiber, D.I., & Zahn, J.D. The effects of electroporation buffer composition on cell viability and electro-transfection efficiency. *Nature Scientific Reports* **10**, 3053 (2020).

Introduction

The ability to perform DNA, RNA, and protein transfection in a safe and efficient manner is increasingly important in both biomedical and clinical research[1-3]. Currently, the gold standard for gene delivery is the use of viruses to perform DNA transfection. Though viral-mediated gene delivery has been shown to be effective, as demonstrated through the recent FDA approval of initial cell therapies, this delivery modality suffers from several drawbacks[4]. The problems associated with viral transfection include cost, cytotoxicity, immunogenicity, mutagenesis/tumorigenesis potential, and size capacity restrictions on the gene to be delivered[5-7]. These disadvantages have led to the continued development of non-viral alternatives.

Over the last 40 years, electroporation has emerged as an attractive approach for delivery of exogenous materials into cells and tissues. Electroporation is a non-viral technique used to deliver DNA, RNA, and proteins (including plasmid DNA (pDNA) vectors) to biological cells. Through the application of external electric fields of appropriate strength, duration, form, and number, a reversible increase in permeability is achieved to allow delivery of both small and large molecules through an otherwise impermeable cell membrane[8]. For many applications, electroporation is advantageous compared to viral-mediated gene delivery. When applied appropriately, it is generally inexpensive, safe, easy to operate, and efficient in performing transfections of cells from a variety of lineages[9]. However, when not optimized, electroporation can induce significant cell death from excessive permeabilization of a cell or generate insufficient transfection efficiency when permeabilization is limited.

Electroporation outcomes are typically defined as the resulting cell viability, defined as the percentage of living cells following electroporation compared to a non-electroporated control, and electro-transfection efficiency (eTE), defined as the percentage of cells receiving or expressing the delivered vector. These outcomes are dependent on a variety of experimental parameters including: electric pulse strength and duration, number of electric pulses applied, cell type, cell density, pDNA concentration, buffer conductivity, and buffer composition[8-12]. Not only does such a large number of experimental variables increase the complexity of protocol optimization, it has led to a vast landscape of published work, making it difficult to draw conclusions among them. This has given rise to numerous electroporation protocols and electroporation buffers used across laboratories or commercial offerings, and it can often be unclear why a particular buffer was selected for

a given cell type, application, or protocol. Electroporation buffers generally fall into several categories of composition – saline-based, phosphate-based, HEPES-based, or cell-culture-media based – with conductivity tailored by the salt added and osmolality adjusted with an osmotic agent, often sugar or an inert protein[13-15].

The effect of electroporation buffer composition on propidium iodide (PI) uptake into myeloma cells has been previously been investigated[10]. In this study electroporation buffers of various conductivities were made using K^+, Na^+, $C1^-$ and SO_4^{2-} as ions. Following electroporation, PI uptake into the myeloma cells was not significantly different regardless of ionic composition at a fixed medium conductivity. However, medium conductivity did affect viability, with low conductivity buffers of the same ionic composition producing lower viability following electroporation. There were also differences in viability between Na^+ and K^+ based buffers at higher field strength (>5 kV/cm) but similar viabilities at lower field strengths. These early studies motivated us to explore how buffer composition can affect electroporation outcomes.

Recently, we have explored how pulsing conditions affect the delivery of small, membrane impermeant dyes such as PI and larger macromolecules such as fluorescein-conjugated dextrans, as well as the effects on the short-term (<2 hours) viability of cells following electroporation[16-20]. For these studies we used a low conductivity HEPES based buffer with the electrolyte conductivity tailored via the addition of $MgCl_2$. This buffer composition exploited an electrokinetic phenomena known as Field Amplified Sample Stacking (FASS), which exploits conductivity differences between the intracellular and extracellular environments, resulting is an increase in small molecule delivery to the cytosol following electroporation[18,19]. In a subsequent study, we investigated a two-pulse electroporation

protocol, consisting of a high intensity, short duration electric pulse to permeabilize the cells, followed by a lower intensity, long duration electric pulse to enhance delivery of exogenous materials into the cytoplasm[21]. One motivating observation from this work was a strong, negative correlation between short term cell viability and the total applied electrical energy of the second applied pulse in all experiments conducted. However, in this earlier work, different HEPES based electroporation buffer conductivities were tested, but only one salt, $MgCl_2$, was used to titrate the buffer to the desired conductivity.

In this paper, we expand our investigation to explore different electroporation buffer compositions, showcasing the effect of different salts and sugars to study the effect of applied electrical energy on long-term cell viability and eTE of pDNA vectors. We systematically explore different buffer compositions and their effect on the electroporation outcomes of cell viability and transfection efficiency for pDNA encoding green fluorescent protein (GFP) 24 hours following electroporation. We also pre-determined the electrical pulsing parameters to keep either the total applied electrical energy (J) or the total ionic charge movement per unit area, i.e. charge flux (C/m^2), a constant. The resulting cell viability was found to be dependent on the applied pulse applied electrical energy, with different buffer compositions expanding the reversible electroporation capabilities of the cell populations. In particular, the presence of Mg^{2+} ions enhanced the ability of cells to recover following high-energy pulse applications. This led us to hypothesize that the effect of magnesium on post electroporation viability is due to magnesium's role in the activation of the ATPase membrane ion channels. Preliminary supporting evidence for this mechanism is shown by inhibiting these enzymes during electroporation with the addition of an ATPase inhibitor, lidocaine. However, Mg^{2+} concentrations need to be optimized, as

the ion also hinders eTE when compared to K^+-based buffers. The approach established and presented in this study allows for a better understanding of the effects that different electroporation buffer solutions have on electroporation outcomes and highlights the importance of buffer recipe in the optimization of electroporation protocols.

3.2 Materials & Methods

3.2.1 Cell Culture

NIH-3T3 mouse fibroblasts were cultured in DMEM supplemented with 10% v/v fetal bovine serum, 1% v/v L-glutamine, and 1% penicillin-streptomycin (Sigma-Aldrich, St. Louis, MO). Cells were plated at a cell density of 1.65×10^5 cells/mL for 24 hours at 37 °C, in a 95% O_2 / 5% CO_2 incubator (Thermo Electron Corp., Marietta, OH) prior to electroporation experiments.

3.2.2 Electroporation Buffer Preparation

A HEPES-based electroporation buffer was used for the current study. Buffer pH was titrated to 7.4 using NaOH. Buffer osmolality was balanced to ~300 mOsm using a commercial osmometer (model 3D3, Advanced Instruments, Norwood, MA) with either sucrose or trehalose as the osmotic balancing agent. Buffer conductivity was adjusted to either 500 μS/cm or 2000 μS/cm using a variety of salts: $MgCl_2$, KCl, $MgSO_4$, or a $MgCl_2$/KCl mixture. Buffer conductivity was measured using a commercial conductivity meter (model COND 6+, Oakton Instruments, Vernon Hills, IL). **Table 3.1** lists detailed information regarding the electroporation buffers tested in this study. For lidocaine experiments, lidocaine hydrochloride was diluted to a final concentration of 10 mM within the cell resuspension. All molecular additives were purchased from Sigma-Aldrich (Sigma-Aldrich, St. Louis, MO).

Salt (mM)	Sugar	Conductivity (µS/cm)
$MgCl_2$ 1.5	Sucrose	500
$MgSO_4$ 1.8	Sucrose	500
$MgCl_2$ / KCl 0.7 / 1	Sucrose	500
KCl 2	Sucrose	500
KCl 2	Trehalose	500
$MgCl_2$ 10	Sucrose	2000
KCl 14	Sucrose	2000

Table 3.1. Electroporation Buffer Concentrations. All buffers contain 10mM HEPES and 3mM NaOH. Both sucrose and trehalose are at a final concentration of 285 mM for all buffers.

3.2.3 DNA Plasmid

Plasmid pMAX-GFP (Lonza, Walkersville, MD), was procured at a concentration of 1 μg/μL from commercially available cell transfection kits (Lonza, Cat No.:VCA-1003, Lot: F-12559, endotoxin levels <1 pg/μg plasmid). Plasmid vectors were loaded to a final concentration of 20 μg/mL prior to electroporation[22-24].

3.2.4 Electroporation Pulse Parameters

A square wave generator, BTX ECM 830 (Harvard Bioscience Inc., Holliston, MA), was used to generate a single electrical pulse of predetermined electric-field strength and duration to an electroporation cuvette. Electric field strength was nominally calculated as: $E = V/d$, where E is the electric field strength (kV/cm), V is the applied voltage (kV), and d is the distance between the electrodes (0.2 cm) in the cuvette. A 1.2 kV/cm pulse for 1 ms in duration was used as the control pulse for determining the remaining pulses in the study. Pulse applications were chosen to conserve either the total applied electrical energy ($W = \sigma \times E^2 \times t \times \upsilon$) or total charge flux ($\Phi_Q = \sigma \times E \times t$), where W is the total applied electrical energy (J), σ is the electroporation buffer conductivity (S/m), E is the applied electric field (V/m), t is the pulse duration (s), υ is the total electroporation buffer volume (m^3), and Φ_Q is the total charge flux (C/m^2). The pulsing conditions applied for constant total charge flux and constant total applied energy can be found in **Table 3.2** and **Table 3.3,** respectively. For each pulsing condition used in this study, temperature changes due to Joule heating of the electrolyte were conservatively calculated assuming all the electrical energy, W, is converted to heat in the solution as $W = \rho \times \upsilon \times C_p \times \Delta T$, where ρ is the solution density (1,000 kg/m^3), υ is the cuvette buffer volume (1×10^{-7} m^3), C_p is the heat capacity of water at room temperature (4,184 J/kgC), and ΔT is the temperature change from the electroporation

pulse. From these calculations, the temperature change from Joule heating is less than 0.75ºC and 3ºC for the 500 μS/cm and 2000 μS/cm buffers respectively for all pulse conditions tested and are considered negligible in this study.

3.2.5 Cell Harvest & Electroporation

3T3 fibroblasts cells were harvested for experiments 24 hours following cell passage. An electroporation protocol was adapted from *Potter & Heller* and our previous work[13, 16-21]. Briefly, following trypsinization, cells were resuspended in antibiotic-free media and centrifuged for 2 minutes at 2000 rpm. The cells were washed using the electroporation buffer under investigation. They were then resuspended at a concentration of 3×10^6 cells/mL in a 0.2 cm gap electroporation cuvette (Fisher Scientific, Waltham, MA), which included the pMAX GFP vector at a final concentration of 20 μg/mL. The total resuspension volume was 100 μL. The cuvettes were then placed on ice for 10 minutes prior to pulse application. Control experiments were conducted for each individual experiment for which the entire experimental procedure was followed but no electrical pulse was delivered. The exterior of the cuvette electrodes were dried, and the cuvettes were secured in the BTX cuvette safety stand where electrical contact was verified with a multimeter. Pulses were applied at room temperature in sterile fashion. Following pulse application, cuvettes were briefly placed on ice before the cells were transferred to a pre-warmed (37 ºC) tissue culture plate containing antibiotic free media and incubated for 24 hours prior to imaging. Cuvettes were discarded after a single use.

3.2.6 Cell Viability & Gene Electro-Transfection Efficiency

Quantification of viability and eTE used a protocol adapted from Haberl et al.[23] Following 24 hours of incubation, cells were washed with PBS and then imaged under phase contrast and epifluorescence microscopy (FITC filter) using a 10× objective to determine the resulting cell viability and eTE, respectively (Microscope: Olympus IX81, Japan, Camera: Hamamatsu Photonics, Model: C4742-95-12G04, Japan, Software: MetaMorph). Images were captured from 5 random locations to gather representative images of the overall population for each experimental condition. Cell viability was determined by normalizing the total cell count per experimental condition to the total cell count in the no pulse control condition. Gene eTE was defined as the ratio of the total number of GFP positive cells to the total number of viable cells per experimental condition.

3.2.7 Statistical Analysis

All experiments were independently run in triplicate (n=3) with the results represented as mean ± standard deviation. Results were analyzed using a two-way ANOVA followed by a Tukey multiple comparison test (GraphPad Prism v7, GraphPad Software, La Jolla, CA) with $p < 0.05$ considered statistically significant. Results from the two-way ANOVAs and statistically significant results from the multiple comparison tests can be found in Supplementary Table 1 and Supplementary Table 2, respectively (**Appendix B**).

3.3 Electroporation Outcomes: Constant Applied Electrical Energy

The effects of buffer composition and charge flux on cell viability and eTE were evaluated in conditions where applied energy was held constant (**Table 3.2**). Separate two-way ANOVAs were performed for two different conductivities. Plots of viability for both conductivities are found in Supplementary Figure 1 (**Appendix B**). For the 500 μS/cm buffers, cell viability was not significantly affected by buffer composition, the charge flux, or the interaction between these. For buffers with 2000 μS/cm conductivity, the effects of charge flux on viability are significant ($p = 0.0044$), whereas the buffer composition and the interaction between the two variables do not have a significant effect. Together, these results generally support our previous observations that cell viability following electroporation is largely dependent on the overall electrical energy applied during transfection procedures[20].

When analyzing the effects that buffer composition, charge flux, and the interaction of these variables have on the eTE, a similar trend is found (refer to **Table 3.2** for eTE values). A two-way ANOVA of the results with 500 μS/cm and with the 2,000 μS/cm conductivity buffers indicated that both buffer composition ($p < 0.0001$) and charge flux ($p = 0.0073$ / $p < 0.0001$) have significant effects on eTE, and that the interaction of these variables is not significant. However, the significant effect of buffer composition on eTE results from the different molecular contents (i.e., Mg^{2+} vs. K^{+} based buffers) of the electroporation buffer. This is better understood when comparing electroporation outcomes for different energy pulse applications.

Pulse Strength (kV/cm)	Pulse Duration (ms)	Viability (%)	eTE (%)	Pulse Strength (kV/cm)	Pulse Duration (ms)	Viability (%)	eTE (%)
Sucrose, $MgCl_2$ (2000 µS/cm)				**Sucrose, $MgCl_2$ / KCl (500 µS/cm)**			
1.2	1.00	77 ± 19	11 ± 3.0	1.2	1.00	90 ± 26	29 ± 19
1.8	0.44	86 ± 9.5	8 ± 0.6	1.8	0.44	88 ± 20	24 ± 6.2
2.4	0.25	84 ± 8.1	14 ± 1.5	2.4	0.25	94 ± 17	35 ± 16
3.6	0.11	65 ± 6.2	19 ± 7.8	3.6	0.11	83 ± 8.6	27 ± 2.9
4.8	0.06	58 ± 8.0	30 ± 2.5	4.8	0.06	88 ± 4.7	34 ± 12
Sucrose, KCl (2000 µS/cm)				**Sucrose, KCl (500 µS/cm)**			
1.2	1.00	79 ± 4.6	21 ± 3.2	1.2	1.00	101 ± 22	32 ± 13
1.8	0.44	77 ± 9.9	17 ± 6.1	1.8	0.44	72 ± 7.8	22 ± 1.5
2.4	0.25	69 ± 13	28 ± 3.1	2.4	0.25	83 ± 18	36 ± 11
3.6	0.11	63 ± 9.3	23 ± 4.6	3.6	0.11	56 ± 7.0	31 ± 12
4.8	0.06	52 ± 20	37 ± 7.0	4.8	0.06	63 ± 20	47 ± 11
Sucrose, $MgCl_2$ (500 µS/cm)				**Trehalose, KCl (500 µS/cm)**			
1.2	1.00	91 ± 2.6	12 ± 4.0	1.2	1.00	68 ± 17	36 ± 7.8
1.8	0.44	96 ± 3.5	8 ± 1.2	1.8	0.44	53 ± 18	43 ± 3.2
2.4	0.25	87 ± 5.9	17 ± 3.5	2.4	0.25	38 ± 4.6	48 ± 18
3.6	0.11	95 ± 10	13 ± 1.0	3.6	0.11	34 ± 12	49 ± 15
4.8	0.06	78 ± 13	22 ± 4.0	4.8	0.06	27 ± 4.5	52 ± 13
Sucrose, $MgSO_4$ (500 µS/cm)							
1.2	1.00	88 ± 8.7	14 ± 3.8				
1.8	0.44	96 ± 42	16 ± 5.6				
2.4	0.25	76 ± 3.1	21 ± 9.3				
3.6	0.11	84 ± 21	21 ± 5.1				
4.8	0.06	81 ± 6.2	23 ± 11				

Table 3.2. Electroporation outcomes for constant applied energy.

3.4 Electroporation Outcomes: Constant Charge Flux

The effects of buffer composition and applied electric pulse energy on cell viability and eTE were examined with conditions where charge flux was held constant (**Table 3.3**). **Figure 3.1** is a plot of cell viability versus applied electrical energy for the constant charge flux experiments using the Mg^{2+} and K^{+} based buffer solutions at a final conductivity of 500 μS/cm. Two separate two-way ANOVAs were performed to examine the effects that buffer composition and applied pulse energy have on cell viability. The first analysis including all buffer compositions at 500 μS/cm. The analysis showed that the buffer composition, pulse energy, and the ordinal interaction between the two all had significant effects on cell viability ($p < 0.0001$). However, a noticeable difference in the viability versus applied energy curve for different buffer compositions is shown in **Figure 3.1**, with two distinct cell viability responses observed, i.e. linear versus nonlinear decay, for the Mg^{2+}-containing and Mg^{2+}-lacking buffer compositions, respectively. A two-way ANOVA of results with only the Mg^{2+} -containing buffer compositions ($MgCl_2$, $MgCl_2$/KCl, $MgSO_4$) indicated that the energy of the pulse application has a significant effect on cell viability ($p < 0.0001$), while both buffer composition and the interaction between variables is not significant, with the post hoc analysis resulting in no statistical significance achieved at any pulse condition between buffer compositions. A visual representation of this can be found in Supplementary Figure 2 (**Appendix B**). This demonstrates the importance of having Mg^{2+} in the buffer composition for cell viability, enhancing the range of reversible electroporation for cell populations. These results are in agreement with other reports, indicating that Mg^{2+} is essential in preserving cell viability[22,23].

Pulse Strength (kV/cm)	Pulse Duration (ms)	Viability (%)	eTE (%)	Pulse Strength (kV/cm)	Pulse Duration (ms)	Viability (%)	eTE (%)
Sucrose, $MgCl_2$ (2000 µS/cm)				**Sucrose, $MgCl_2$ / KCl (500 µS/cm)**			
1.2	1.00	77 ± 19	11 ± 3.0	1.2	1.00	90 ± 26	29 ± 19
1.8	0.67	80 ± 4.7	11 ± 0.6	1.8	0.67	88 ± 3.6	20 ± 4.6
2.4	0.50	50 ± 6.0	34 ± 1.5	2.4	0.50	87 ± 8.5	42 ± 14
3.6	0.33	24 ± 5.9	55 ± 6.7	3.6	0.33	67 ± 14	42 ± 3.8
4.8	0.25	18 ± 4.0	65 ± 7.6	4.8	0.25	39 ± 11	70 ± 9.8
Sucrose, KCl (2000 µS/cm)				**Sucrose, KCl (500 µS/cm)**			
1.2	1.00	79 ± 4.6	21 ± 3.2	1.2	1.00	101 ± 22	32 ± 13
1.8	0.67	44 ± 12	32 ± 5.5	1.8	0.67	49 ± 6.1	40 ± 4.2
2.4	0.50	24 ± 4.0	57 ± 5.8	2.4	0.50	30 ± 10	73 ± 8.7
3.6	0.33	11 ± 5.9	57 ± 2.5	3.6	0.33	6.3 ± 2.5	71 ± 2.6
4.8	0.25	7 ± 2.1	80 ± 10	4.8	0.25	9.0 ± 4.4	82 ± 1.0
Sucrose, $MgCl_2$ (500 µS/cm)				**Trehalose, KCl (500 µS/cm)**			
1.2	1.00	91 ± 2.6	12 ± 4.0	1.2	1.00	68 ± 17	36 ± 7.8
1.8	0.67	91 ± 5.1	9 ± 1.0	1.8	0.67	30 ± 11	48 ± 2.9
2.4	0.50	82 ± 9.1	26 ± 3.5	2.4	0.50	21 ± 9.5	67 ± 21
3.6	0.33	83 ± 7.0	18 ± 1.5	3.6	0.33	24 ± 17	52 ± 17
4.8	0.25	61 ± 12	43 ± 12	4.8	0.25	8 ± 4.4	69 ± 24
Sucrose, $MgSO_4$ (500 µS/cm)							
1.2	1.00	88 ± 8.7	14 ± 3.8				
1.8	0.67	102 ± 5	15 ± 4.2				
2.4	0.50	79 ± 14	25 ± 8.6				
3.6	0.33	80 ± 26	21 ± 4.4				
4.8	0.25	49 ± 4.0	42 ± 16				

Table 3.3. Electroporation outcomes for constant charge flux.

Although Mg^{2+} ions appear to preserve cell viability, the addition of magnesium can dramatically reduce the eTE[25,26]. When comparing results for the eTE, Mg^{2+}-containing buffers result in lower eTEs compared to that of the K^{+}-based buffer solutions (**Figure 3.2**). In a similar fashion, two separate two-way ANOVA were performed to analyze the 500 μS/cm data (Mg^{2+}-containing buffers and all buffers). The two-way ANOVA results when comparing all buffer solutions show that pulse energy ($p < 0.0001$), buffer composition ($p < 0.0001$), and the interaction between variables ($p = 0.148$, ordinal) all have a significant effect on eTE. A separate analysis of only Mg^{2+}-containing buffer compositions indicates that the applied pulse energy and the buffer composition significantly effect eTE ($p < 0.0001$), but the interaction between them is not significant. Post hoc comparisons revealed that higher concentrations of Mg^{2+} negatively impact eTE. In particular, the combination buffer of $MgCl_2$/KCl resulted in significantly greater eTEs when compared against buffers containing only $MgCl_2$ and $MgSO_4$. Altogether, these results suggest an optimal concentration of Mg^{2+} could be determined for an electroporation buffer, as the Mg^{2+} ion plays a major and competing role in cell viability and transfection efficiency.

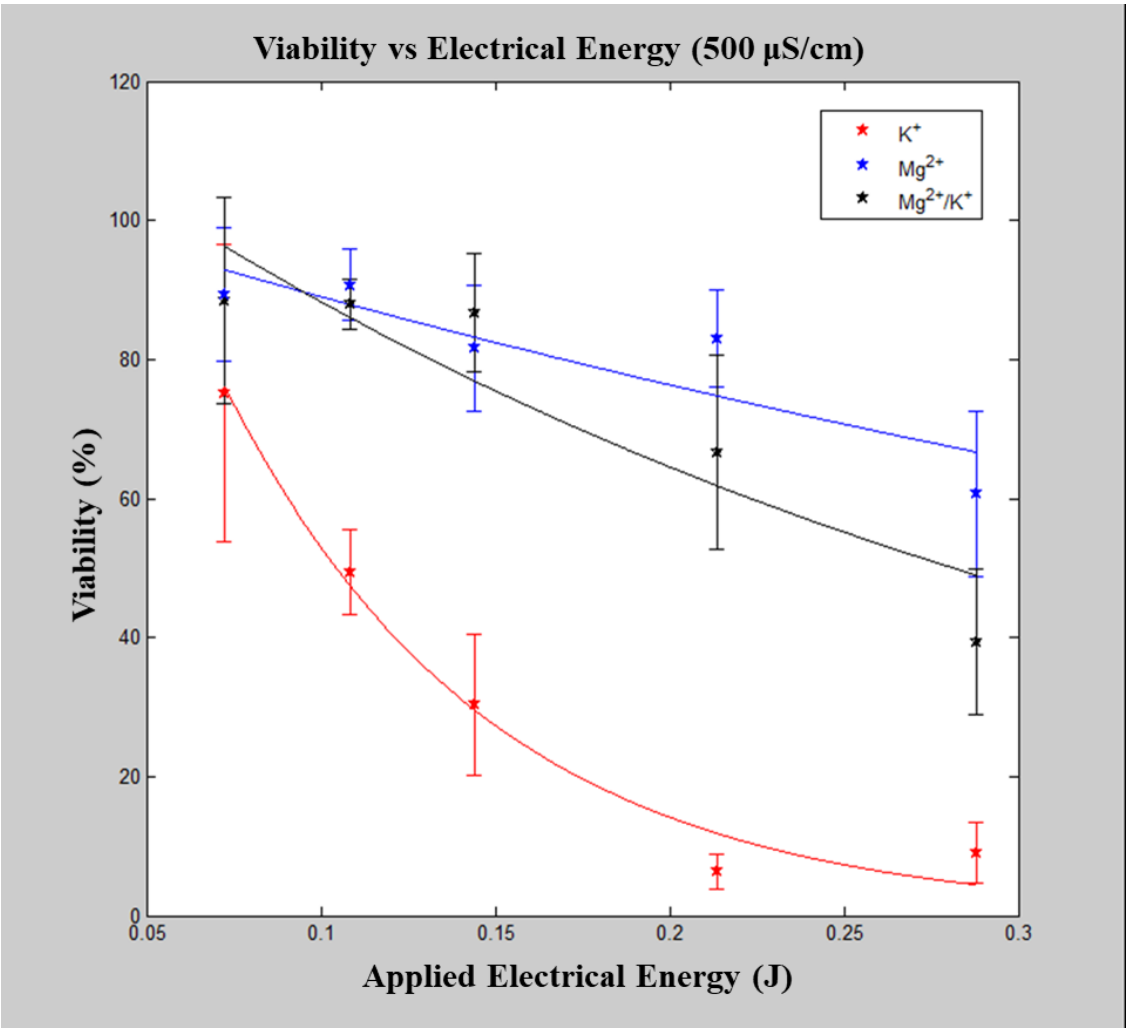

Figure 3.1. Viability versus applied electrical energy. Each buffer with a final conductivity of 500 µS/cm with Cl^- as the anion, and sucrose as the osmotic balancing agent. Mg^{2+} and Mg^{2+}/K^+ buffers had significantly greater viability results ($p < 0.05$) when compared to the K^+ buffer. Mg^{2+} -containing buffers resulted in a linear viability response, whereas the K^+ buffer resulted in an exponential decay viability response curve.

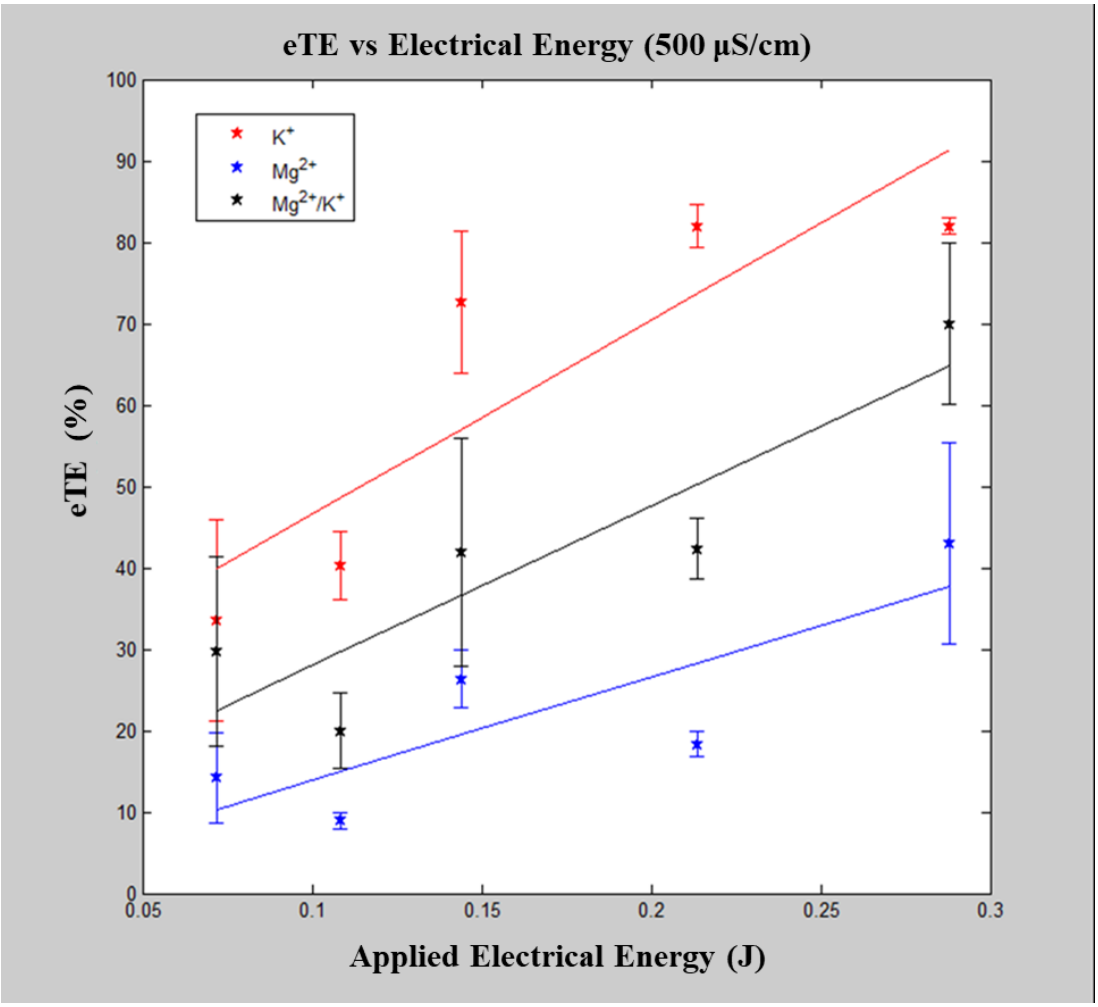

Figure 3.2. Electro-transfection efficiency versus applied electrical energy. Each buffer with a final conductivity of 500 µS/cm with Cl^- as the anion and sucrose as the osmotic balancing agent. The presence of Mg^{2+} leads to lower levels of eTE compared to the KCl-based buffer, with higher concentrations of Mg^{2+} further enhancing this observed effect. All buffer compositions saw a linear increase in eTE with increasing applied energy.

3.5 Role of Magnesium During Electroporation

These findings led us to hypothesize that effects of Mg^{2+} on viability and eTE are due to the interaction between Mg^{2+} and nucleic acids, the role that Mg^{2+} plays as a cofactor for biochemical reactions, or a combination of the two. Mg^{2+} is an essential divalent cation that is required for the activation of numerous cellular enzymes.

Using fluorescently labeled pDNA vectors, Haberl et al. reported an enhanced interaction between the cell membrane and pDNA with increasing concentrations of Mg^{2+} [22]. Although they believe this to be a necessary step for transfection, it is possible this interaction leads to lower eTE as more DNA is captured on the membrane surface and fewer vectors permeate through the membrane into the intracellular space. Another mechanism that may lead to lower eTE is the role of the magnesium ion as a cofactor for biochemical reactions, in particular the activation of DNase and RNase enzymes, leading to the degradation of the pDNA or translated mRNA prior to protein synthesis[27]. This hypothesis has been tested previously via nonspecific enzyme inhibition using Zn^{2+} [28]. Delgado-Canedo et al. examined the effect of adding Zn^{2+} to the buffer solution either prior to electroporation, during electroporation, or immediately following electroporation. They reported a 12% enhancement in eTE when Zn^{2+} was added immediately following electroporation compared to no Zn^{2+} added[29]. This methodology was repeated by Haberl et al., but no changes in eTE with the presence of Zn^{2+} were reported[23]. We also repeated this experiment (data not shown), and found no increase in eTE in any of the three Zn^{2+} application conditions. The inability to reproduce this experiment is likely the result of experimental variability, as the inhibition is dependent on the timing of Zn^{2+} application. However, the

use of Zn^{2+} resulted in a decrease in cell viability presumably due to the inhibition of membrane-protein ion channels.

3.6 ATPase Inhibition

Upon exposure to the high-intensity external electric field during electroporation, intracellular ionic homeostasis is disturbed, with the resulting cell viability dependent on the recovery of this homeostatic environment[30] presumably through the sodium-potassium ATPase ion pump. Rols et al. demonstrated that depleting ATP in CHO cells via incubation in sodium azide and 2-deoxy-D-glucose did not affect permeabilization efficiency but had a dramatic effect on viability following electroporation[31]. In addition to the activation of DNase/RNase enzymes, Mg^{2+} is also required for the activation of ATPase ion transporters[27,32]. Pilotelle-Bunner et al. reported that Mg^{2+} has a high binding affinity (K_d = 0.069 mM) for this enzyme, with enzyme activity saturating at ~ 1 mM Mg^{2+} These protein transporters are responsible for the active transport of critical ions (Na^+, K^+, Cl^-, etc.) across the cell membrane[32]. Hence, the presence of Mg^{2+} in electroporation buffers may enhance cell viability by accelerating the re-establishment of ionic homeostasis, even at higher-energy pulse applications.

To preliminarily examine this hypothesis, lidocaine, a known ATPase ion channel inhibitor, was added to the electroporation buffer solutions (KCl and $MgCl_2$ at 500 μS/cm) at a final concentration of 10 mM[33-35]. Electric pulses of different applied energy and cell viability was assessed at 24 hours. **Figure 3.3** is a plot of cell viability versus applied electrical energy for both buffers with and without the addition of lidocaine. Both buffer composition (i.e., presence of lidocaine) and pulse energy significantly affected cell viability. (Please refer to Supplementary Tables 1 and 2 for exact tests and significance values, **Appendix B**). In the case of the KCl buffers, the addition of lidocaine led to a decreased cell viability at lower pulse energy applications, however, the statistical viability

response was not affected. This suggest that intracellular Mg^{2+} stores allow for cell recovery at lower energy pulse applications. A more dramatic effect was observed with the addition of lidocaine to the $MgCl_2$ buffer. In this case, upon surpassing an applied energy threshold, we see a dramatic change in the viability response curve, resembling the viability response of the KCl-based buffer solution. This data provides some evidence that ATPase activation, through binding of extraneous Mg^{2+}, is necessary to conserve cell viability following high-energy electroporation pulse applications, enhancing the cell population's electrical energy tolerance to result in reversible electroporation.

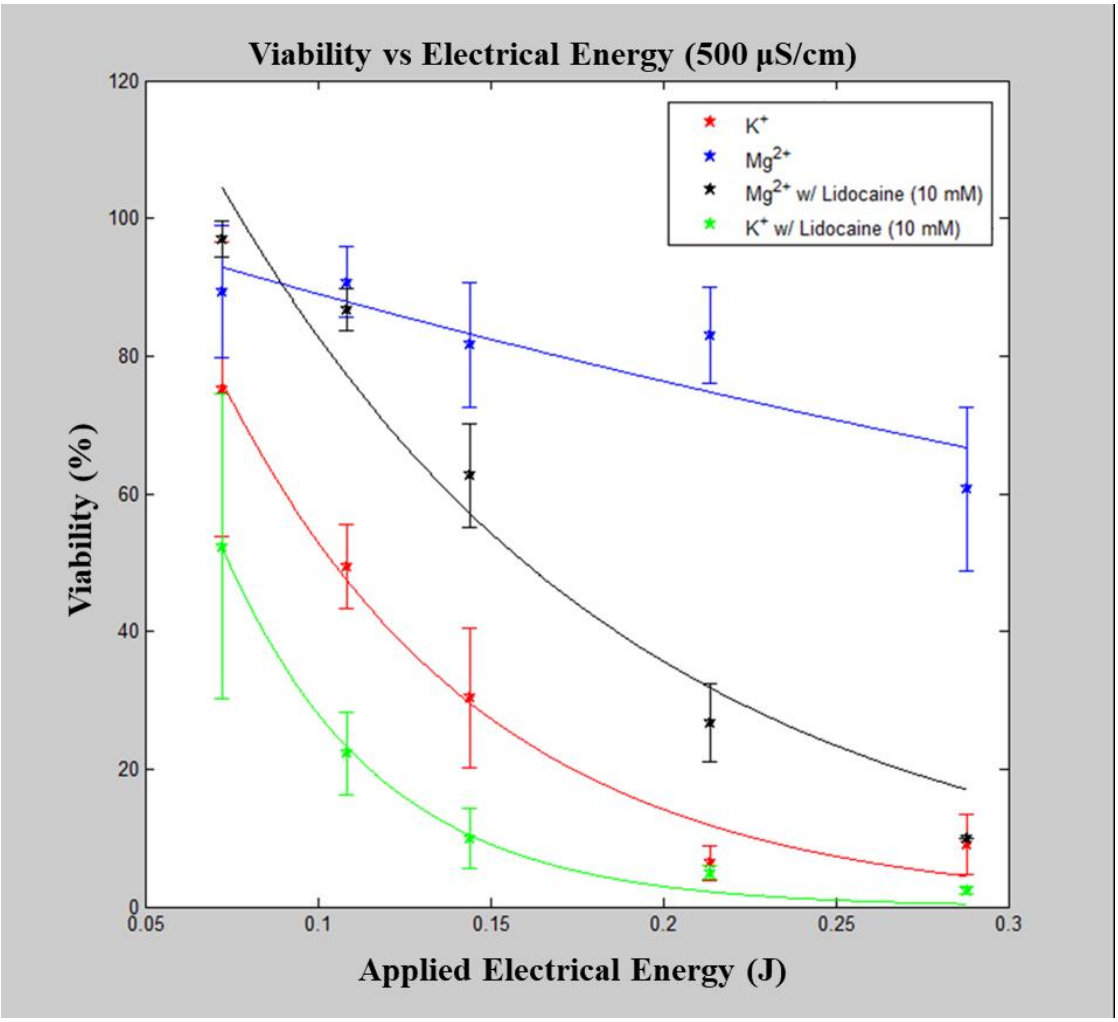

Figure 3.3. Membrane ATPase inhibition. Cell viability was assessed for both $MgCl_2$ and KCl buffers at 500 µS/cm with the addition of lidocaine, an ion channel inhibitor, at a final concentration of 10 mM. A significant difference is found in resulting cell viability when lidocaine is present even in the presence of Mg^{2+}, most notably the shift in the viability response curve resembling that of the KCl-based buffer composition.

3.7 Electroporation Outcome Score

To explore the combined effects of both viability and eTE on electroporation outcomes, where one seeks to obtain both high viability and high transfection efficiency, a scoring metric was created (**Figure 3.4**). This metric is the product of the cell viability (% living cells) and transfection efficiency percentages (of those living cells, % transfected/expressing GFP), with scores ranging from 0 a.u. to 100 a.u., for each experimental condition as shown in **Figure 3.4**. This metric allows for the discrimination between both the different buffer solutions and pulse applications in the study. In our results we find the existence of three distinct regions: high viability with low eTE (1), low viability with high eTE (2), and moderate-to-high viability with moderate eTE (3). The high viability with low eTE group (1) is composed of all buffer solutions at lower-energy pulse applications and Mg^{2+} containing buffers at higher-energy pulse applications. In this region it is likely that few cells were permeabilized, resulting in low transfection outcomes. The low viability / high eTE group (2) is composed of buffers lacking Mg^{2+} at high-energy pulse applications. Therefore, cells suspended in a KCl-based buffer that remain viable following high-energy pulses are likely to be successfully transfected. Cells in this group are presumably over-permeabilized and unable to recover, resulting in low viability outcomes. The final group, which we consider optimal according to our metric, is the moderate to high viability / moderate eTE (3). This region of outcomes is the result of the most cells undergoing reversible electroporation, up-taking and transcribing the pDNA, all the while surviving the overall electroporation process. This group mainly consists of the KCl buffer at 500 μS/cm with low- to moderate- energy pulse applications and the $MgCl_2$ / KCl mixture buffer at 500 μS/cm for all pulse applications, with the mixture buffer

resulting in the highest outcomes scores. These data further show the necessity of including an optimal amount of Mg^{2+} in the electroporation buffer. The highest electroporation outcome was 52 a.u. ($MgCl_2$ / KCl, 2.4 kV/cm : 500 μs, viability—93%, eTE—56%), demonstrating substantial room for improvement, particularly in eTE. Recent works have demonstrated and noted the important role of endocytotic pathways in successful electro-transfection outcomes, specifically the inhibitory effect of prolonged cold temperatures on cells following electroporation pulse application[26,36-38]. Taking this into consideration, by eliminating the brief ice incubation period following electroporation, an enhancement in the electroporation outcomes could be expected. Nevertheless, these results provide important insights and a methodology to show a quantifiable comparison between the different effects the chosen buffer compositions have on electroporation outcomes and thereby allow for the rational development of electroporation buffer composition. In particular, the results highlight the need to optimize the Mg^{2+} ion concentration to enhance both cell viability and eTE outcomes, which is in agreement with other reports[26]. Utilizing these findings in tandem with optimization of the other variables will increase electroporation-outcome scores, leading to further adoption of electroporation as a modality to perform clinically-relevant cell transfections.

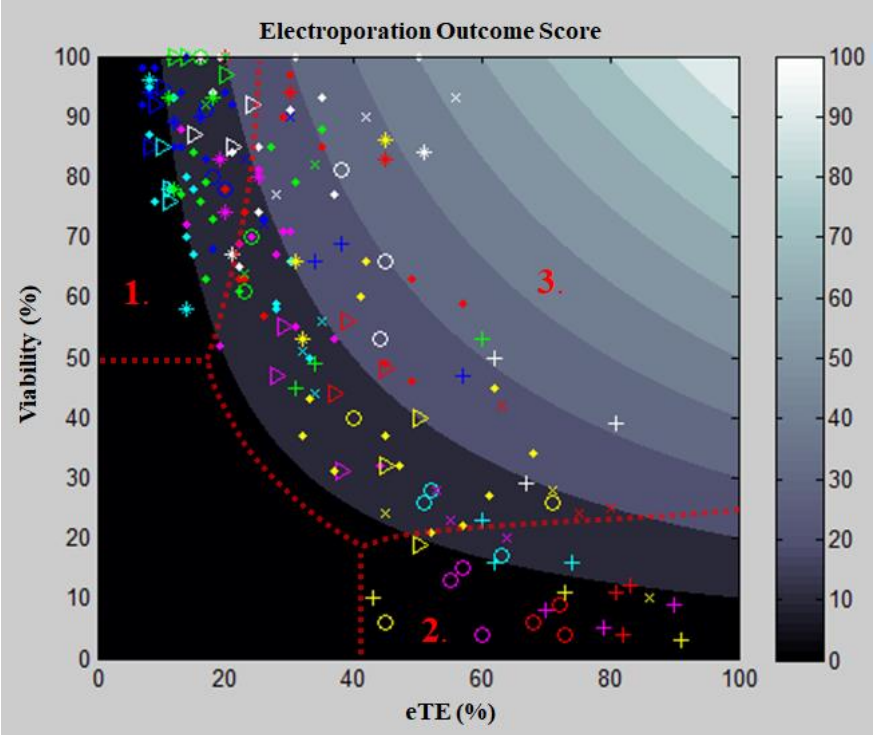

Figure 3.4. Electroporation outcome score. Buffer color code: blue—$MgCl_2$ (500 µS/cm), red—KCl (500 µS/cm), cyan— $MgCl_2$ (2000 µS/cm), magenta— KCl (2000 µS/cm), white— $MgCl_2$/KCl (500 µS/cm) green—$MgSO_4$ (500 µS/cm), yellow—KCl with trehalose (500 µS/cm). Pulse application code: *****—control pulse (1.2 kV/cm : 1 ms), ◊—constant applied energy, Δ—1.8 kV/cm : 670 µs, ×—2.4 kV/cm : 500 µs, ○—3.6 kV/cm : 330 µs, +—4.8 kV/cm : 250 µs. Region 1 is representative of high viability with low eTE and is comprised of Mg^{2+} (+) buffers and/or low energy pulse applications. Region 2 is representative of low viability with high eTE and is comprised of Mg^{2+} (-) and/or high energy pulse applications. Region 3 is moderate to high viability with moderate eTE and is comprised of Mg^{2+} (-) at low energy pulse applications and Mg^{2+} (+) at higher energy pulse applications, with the Mg^{2+}/K^{+} buffer resulting in the best outcome scores.

3.8 Future Directions / Conclusion

We anticipate that the approach used in designing these studies can be expanded to include other buffer compositions and cell types (i.e., PBMCs, Jurkat cells, HEK293T cells). This will help inform the development of optimized electroporation protocols for specific applications such as gene editing, CAR T-cell generation, etc. However, each electroporation buffer (i.e., cell-culture media, phosphate-buffered saline, and other phosphate-based buffers) and cell type may yield different viability and eTE for a given application and must be considered moving forward. We also wish to further examine our hypothesis that the effect of magnesium on post electroporation viability and eTE is due to magnesium's role as a cofactor in biochemical processes. We believe the systematic modification of buffer composition coupled with keeping pulse energy and total charge flux constant represents an improved approach to determining optimized electroporation protocols in such a large experimental parameter space.

In this work we showcase the effect that different compositions of electroporation buffer have on cell viability and eTE. Most notably, the results confirm the important role that Mg^{2+} plays as an enzymatic co-factor leading to an enhancement of cell viability while hindering eTE following the electroporation process. Electroporation outcomes were compared using a quantifiable metric, the product of the cell viability and eTE percentages, allowing for a discrimination between experimental results. These results suggest that an optimal concentration of Mg^{2+} should be contained within the electroporation-buffer solution to strengthen a cell population's ability to undergo reversible electroporation.

3.9 Chapter References

1. Carlo, D. Di, & Lee, L. P. Dynamic Single-Cell Analysis for Quantitative Biology. *Analytical Chemistry* **78**, 7918–7925 (2006).
2. Wang, D., & Bodovitz, S. Single cell analysis: The new frontier in "omics." *Trends in Biotechnology* **28**, 281–290 (2010).
3. Zheng, M. *et al.* Continuous-flow, electrically-triggered, single cell-level electroporation. *Technology* **5**, 31–41 (2017).
4. Ginn, S. L. *et al.* Gene therapy clinical trials worldwide to 2012 - an update. *Journal of Gene Medicine* **15**, 65–77 (2013).
5. Gallego-Perez, D. *et al.* Topical tissue nano-transfection mediates non-viral stroma reprogramming and rescue. *Nature Nanotechnology* **12**, 974–979 (2017).
6. Kim, T. K., & Eberwine, J. H. Mammalian cell transfection: The present and the future. *Analytical and Bioanalytical Chemistry* **397**, 3173–3178 (2010).
7. Roth, T. L. *et al.* Reprogramming human T cell function and specificity with non-viral genome targeting. *Nature* **559**, 405–409 (2018).
8. Bolhassani, A., Khavari, A. & Orafa, Z. Electroporation – Advantages and Drawbacks for Delivery of Drug, Gene and Vaccine. In Application of Nanotechnology in Drug Delivery. A.D. Sezer (**Ed.**). (2014), InTech, Rijeka, Croatia - EU.
9. Kotnik, T. *et al.* Membrane Electroporation and Electropermeabilization: Mechanisms and Models. *Annual Review of Biophysics* **48**, 63-91 (2019).
10. Djuzenova, C.S. *et al.* Effect of medium conductivity and composition on the uptake of propidium iodide into electropermeabilized myeloma cells. *Biochim. Biophys. Acta Biomembranes* **1284**,143-152 (1996).
11. Yao, S. *et al.* Improvement of electroporation to deliver plasmid DNA into dental follicle cells. *Biotechnology Journal* **4**, 1488–1496 (2009).
12. Pucihar, G. *et al*. Equivalent Pulse Parameters for Electroporation. *IEEE Transactions on Biomedical Engineering* **58**, 3279-3288 (2011).
13. Potter, H. & Heller, R. Transfection by Electroporation. *Curr Protoc Mol Biol.* **9**, 1-11 (2003).
14. Ding, X. *et al.* High-throughput Nuclear Delivery and Rapid Expression of DNA via Mechanical and Electrical Cell-Membrane Disruption. *Nature Biomedical Engineering* **1**, 0039 (2017)
15. Li, L. H. *et al.* Highly efficient, large volume flow electroporation. *Technology in Cancer Research and Treatment* **1**, 341–349 (2002).
16. Demiryurek, Y. *et al.* Transport, resealing, and re-poration dynamics of two-pulse electroporation-mediated molecular delivery. *Biochimica et Biophysica Acta (BBA) - Biomembranes* **1848**, 1706–1714 (2015).
17. Li, J., & Lin, H. Numerical simulation of molecular uptake via electroporation. *Bioelectrochemistry* **82**, 10–21 (2011).
18. Li, J. *et al.* The effect of extracellular conductivity on electroporation-mediated molecular delivery. *Biochimica et Biophysica Acta - Biomembranes* **1828**, 461–470 (2013).

19. Sadik, M. M. *et al.* Quantification of propidium iodide delivery using millisecond electric pulses: Experiments. *Biochimica et Biophysica Acta – Biomembranes* **1828**, 1322–1328 (2013).
20. Zheng, M. *et al.* Hydrodynamically controlled cell rotation in an electroporation microchip to circumferentially deliver molecules into single cells. *Microfluidics and Nanofluidics* **20**, 1–12 (2016).
21. Sadik, M. M. *et al.* Scaling relationship and optimization of double-pulse electroporation. *Biophysical Journal* **106**, 801–812 (2014).
22. Haberl, S., Miklavčič, D., & Pavlin, M. Effect of Mg ions on efficiency of gene electrotransfer and on cell electropermeabilization. *Bioelectrochemistry* **79**, 265–271 (2010).
23. Haberl, S., et al. Effect of different parameters used for *in vitro* gene electrotransfer on gene expression efficiency, cell viability and visualization of plasmid DNA at the membrane level. *The Journal of Gene Medicine* **15**, 169-181 (2013).
24. Ng, M.M. Exclusive Compendium: Optimizing an Electroporation Protocol. *Harvard Bioscience Publication*. **1**, 1-17 (2019).
25. Wang, H., & Griffiths, M. W. Mg2+-free buffer elevates transformation efficiency of Vibrio parahaemolyticus by electroporation. *Letters in Applied Microbiology* **48**, 349–354 (2009).
26. Wu, M. & Yuan, F. Membrane Binding of Plasmid DNA and Endocytic Pathways Are Involved in Electrotransfection of Mammalian Cells. *PLOS ONE* **6**, 1-9 (2011).
27. Schmitz, C. *et al.* Dual-Function Ion Channel/Protein Kinases: Novel Components of Vertebrate Magnesium Regulatory Mechanisms. *Pediatric Research* **55**, 734–737 (2004).
28. Ku, W. Y. *et al.* The zinc ion in the HNH motif of the endonuclease domain of colicin E7 is not required for DNA binding but is essential for DNA hydrolysis. *Nucleic Acids Research* **30**, 1670–1678 (2002).
29. Delgado-Cañedo, A. *et al.* Optimization of an electroporation protocol using the K562 cell line as a model: Role of cell cycle phase and cytoplasmic DNAses. *Cytotechnology* **51**, 141–148 (2006).
30. Reinhart, R. A. Clinical correlates of the molecular and cellular actions of magnesium on the cardiovascular system. *American Heart Journal* **121**, 1513–1521 (1991).
31. Rols, M. *et al.* Control by ATP and ADP of voltage-induced mammalian-cell-membrane permeabilization, gene transfer and resulting expression. *European Journal of Biochemistry* **254(2)**, 382-388 (1998).
32. Pilotelle-Bunner, A. *et al.* Mechanism of Mg2+binding in the Na+, K+-ATPase. *Biophysical Journal **96***, 3753–3761 (2009).
33. Yatime, L. *et al.* P-type ATPases as drug targets: Tools for medicine and science. *Biochimica et Biophysica Acta - Bioenergetics* **1787**, 207–220 (2009).
34. Grys, M., Madeja, Z., & Korohoda, W. Decreasing the thresholds for electroporation by sensitizing cells with local cationic anesthetics and substances that decrease the surface negative electric charge. *Cellular and Molecular Biology Letters* **19**, 65–76 (2014).

35. Kutchai, H., Geddis, L. M., & Farley, R. A. Effects of Local Anaesthetics on the Activity of the Na , K-ATPase of Canine Renal Medulla. *Pharmacological Research* **41**, 1–7 (2000).
36. Rosazza, C. *et al.* Gene Electrotransfer: A Mechanistic Perspective. *Current Gene Therapy* **16**, 98-129 (2016).
37. Mao, M. *et al.* Involvement of a Rac1-Dependent Macropinocytosis Pathway in Plasmid DNA Delivery by Electrotransfection. *Molecular Therapy* **25**, 803-815 (2017).
38. Rols, MP *et al.* Temperature effects on electrotransfetion of mammalian cells. *Nucleic Acids Research **22**, 540 (1994).*

Chapter 4

Cell Membrane Permeabilization Detection

4.1 Study Overview

The work presented in this chapter is the first generation of the micro-scale, microfluidic electroporation platform, capable of electrically monitoring the degree of membrane permeabilization on the single-cell level in a continuous flow environment. In this chapter, evidence of this technology's capability to electrically monitor the degree of cell membrane permeabilization is presented. Parts of this work have been published in the journal *Technology* and/or as part of an application note on the Zurich Instruments website.

Zheng, M., Sherba, J.J., Shan, J.W., Lin, H., Shreiber, D.I., Zahn, J.D. Continuous-flow, electrically-triggered, single cell-level electroporation. *Technology*, **5**, 1-11, 2017.

Sherba, J.J., & Zahn, J.D. Monitoring of Cell Membrane Permeabilization in an Electroporation Device. *Zurich Instruments Application Note*. 2017. https://www.zhinst.com/sites/default/files/zi_hf2li_appnote_electroporation.pdf

Previous works and technologies contributing to the motivation for this work were discussed in detail in chapter 2. The innovation of this micro-scale device is its ability to detect, pulse, and electrically monitor single cells both in a continuous flow environment and an automated fashion. This technology bridges the gap between the predecessor devices, the static, electrical monitoring-abled devices and the continuous flow, high-throughput devices[1-4]. Ultimately, upon further technology advancement, this micro-scale electroporation has the potential to eliminate the need for empirically-derived electroporation protocols.

4.2 Materials and Methods

4.2.1 Device Fabrication

The micro-device consists of a pair of planar, titanium/platinum (Ti/Pt) electrodes on a glass substrate and a polydimethylsiloxane (PDMS) microchannel fabricated via soft lithography[5,6]. The silicon wafer master mold with device features were fabricated using standard photolithographic techniques using the EVG620 mask aligner. The recipes for photolithography were developed following recommended protocols from the photoresist suppliers (MicroChem). The mask was designed using AutoCAD software and manufactured by Cad/ART, with a guaranteed resolution of 10 μm. The electroporation region of the microfluidic device was designed as having a channel constriction of the dimensions 250×25×10 μm^3, the depths of the channels were validated using a surface profiler (DekTak). Prior to pouring PDMS over the silicon master mold, the mold was treated with perfluorodecyltrichlorosilane (SigmaAldrich) to form a self-assembled monolayer to minimize the adherence of PDMS on the SU-8 substrates and increasing the lifetime of the silicon master mold. A 10 : 1 mixture of PDMS polymer and hardening agent were poured over the master mold to create a negative replica and was allowed to cure at 65 °C overnight. The cured PDMS was then surgically cut-off of the master mold and holes were punched to define the inlet (0.75 mm) and outlet (3 mm), to gain fluidic access to the device. Punched PDMS devices were sonicated in an isopropanol bath to removed debris from the inlets/outlets and then placed in the 65 °C oven overnight to de-swell. Ti/Pt planar electrodes were fabricated via a metal ‘lift-off’ process. Electrode patterns were defined photolithographically on a glass substrate and recesses were chemically etched in a 10 : 1 buffered hydrofluoric acid for 1 minute to a depth of ~200

nm. The metals were deposited using physical vapor deposition (KJL PVD75, Kurt Lesker). The deposition times for titanium followed by platinum were 8 min and 10 min, respectively. Following deposition, the remaining photoresist was dissolved in an acetone bath to perform the 'lift-off', leaving behind the defined set of Ti/Pt planar electrode traces which were 100 μm in width and 300 μm in separation. The surfaces of the PDMS and electrode substrates were treated under oxygen plasm at 70 W power, 250 sccm O_2, at 350 mTorr for 35 s (PX-250, March Instruments). The activated substrates were aligned under a stereo microscope (SZ61 Binocular Stereo Zoom, Olympus) and irreversibly bonded to form the enclosed microfluidic capillary. Devices were briefly placed on a hot plate at 95 °C to ensure a strong bond. Copper wires were bonded to the planar electrodes via conductive epoxy to allow for electrical connection with the rest of the experiment set-up. An illustration of the electroporation region of the microfluidic device can be seen in **Figure 4.1**.

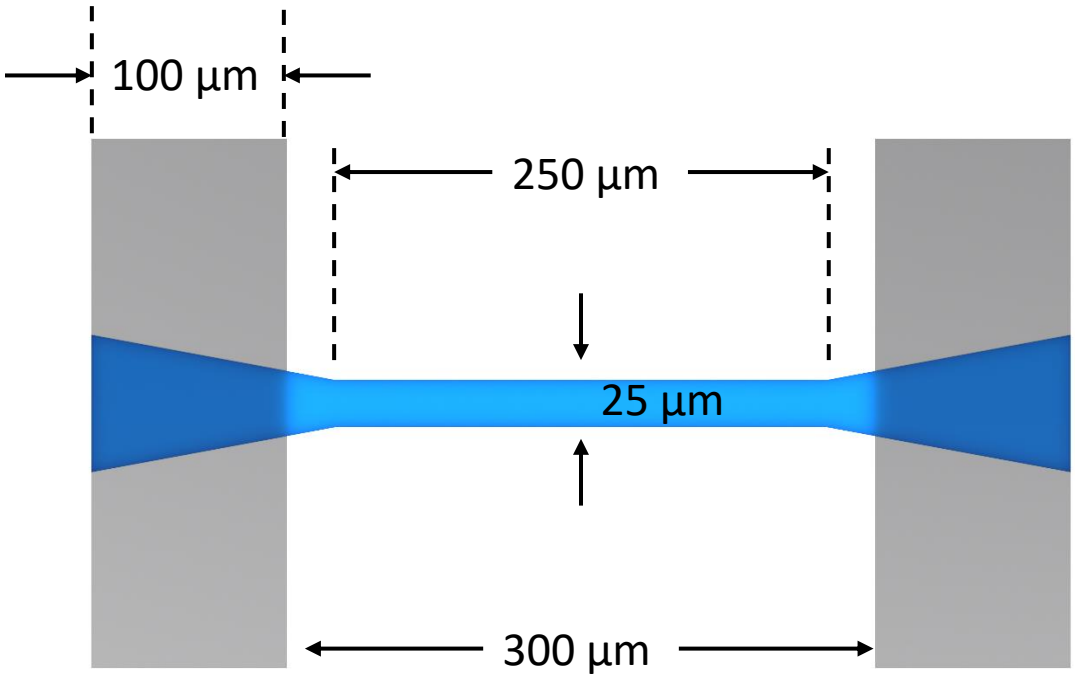

Figure 4.1. Illustration of the electroporation region of microfluidic device. The microfluidic structure was manufactured out of PDMS using soft lithography. The electroporation region of the device was irreversibly bonded using oxygen plasma surface activation. The channel constriction (250×25×10 μm^3) is between a set of planar titanium/platinum electrodes which are 100 µm wide separated by 300 um.

4.2.2 System Operation

The operation of the automated, detect-pulse electroporation system starts with the perfusion of single cells through the microfluidic channel constriction (**Figure 4.1**). The electroporation region was designed as a microchannel constriction-based geometry[7]. This geometry allows for a high cell-volume fraction which increases the signal-to-noise ratio (SNR) capabilities of the sensing device. The high SNR allows for both the detection of the current change due to the entrance of the cell (ΔI_c) as well as the change in current following electroporation pulse application (ΔI_p) noted as the permeabilization current. An example of an electric current reading for a cell electroporated with a 1.05 kV/cm : 5 ms pulse is shown in **Figure 4.2**. In addition, the geometry amplifies the applied electric field strength by a factor of 1.75-times (determined with COMSOL), minimizes the voltage requirements to achieve successful electroporation.

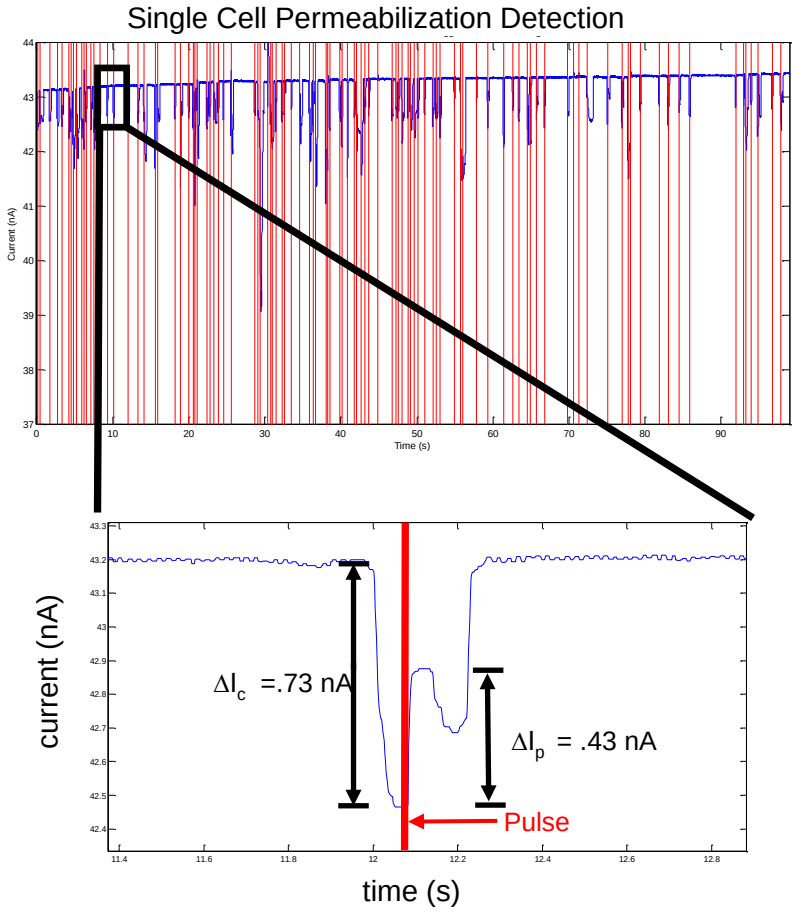

Figure 4.2. Electrical recording of single cell level permeabilization detection. (Top) Current reading showing the application of the electroporation pulse (red line) to single cells in a serial fashion. (Bottom) Close-up current signal for a single cell in transit. Upon cell entry into the electroporation region, the insulated cell membrane causes a sharp decrease in the current (due to an increase in resistance). The current drop due to the cell size is noted as ΔI_c. The sharp signal change is detected via LabVIEW to output a prescribed electroporation pulse (red line). The change in current following electroporation is noted as ΔI_p, or the permeabilization current. After the cell exits the electroporation region the current signal returns to baseline.

Standard electrical impedance spectroscopy utilizing the resistive-pulse method is used for detecting the traversing cells between the electrodes[8-10]. **Figure 4.3** is a workflow diagram showing the order of operations for a successful cell detection and pulse application. Briefly, the Zurich HF2LI lock-in amplifier signal output channel outputs a 1 V_{p-p} sine wave at a frequency of 1.224 kHz to excite the device-under-test (DUT) which allows for the detection of membrane permeabilization[11-13]. The voltage in the DUT is monitored at the 2nd electrode by the HF2TA current pre-amplifier and the current is then sent to the lock-in signal input. This signal is sent to a custom-built LabVIEW algorithm (see chapter 6) which detects a sharp decrease in current when a cell enters the electroporation region and automatically outputs a TTL digital output to trigger the application of both the prescribed electroporation pulse from a function generator (33220A Waveform Generator, Agilent) and the capture of a fluorescence image by a mounted microscope CMOS camera (PowerView 1.4MP, TSI). The pulse from the function generator was fed into a high-voltage amplifier (Model 2350, TEGAM) to amplify to the pulse to the desired strength. The amplified pulse was then sent into the signal add-on channel of the lock-in amplifier where it was then superimposed on the sine-wave. To protect the input of the lock-in amplifier, a CMOS switch (DF419DJ+ Analog Switch, Maxim Integrated) was synchronized with the electroporation pulse to prevent the high energy pulses from damaging the lock-in amplifier. During this process, the change in current is continuously monitored by the LabVIEW before and after pulse application to the cell in transit. Upon cell exit, the baseline current reading is restored, and the system then awaits the entry of the next cell where this process will then repeat itself.

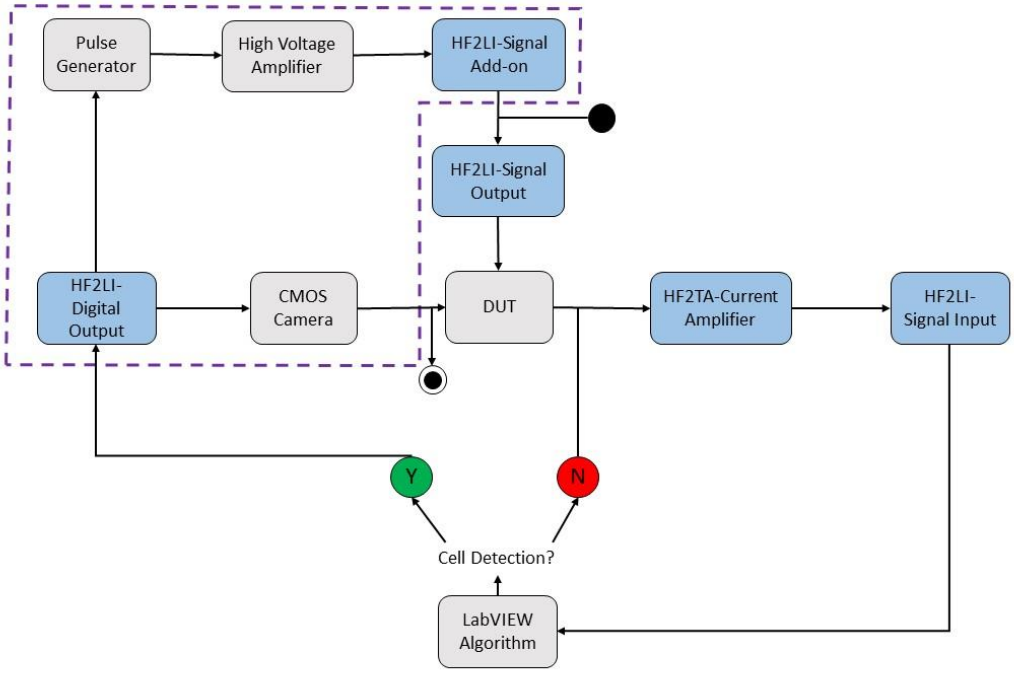

Figure 4.3. System operation schematic. The lock-in frequency signal is generated by the HF2LI and delivered to the device-under-test (DUT) via the signal output. The voltage in the channel is then measured and sent to the HF2TA current amplifier, and this current reading is then sent into the HF2LI signal input channel. The current is then monitored by a custom-built LabVIEW program. Upon cell detection, a digital output is generated to trigger both the electroporation pulse and image capture.

4.2.3 Experimental Design

Mouse 3T3 fibroblasts cells were cultured in DMEM supplemented with 10% FBS, 1% L-glutamine, and 1% penicillin/streptomycin (Sigma Aldrich, St. Louis, MO). Once cells reached 70%-80% confluency in a 6-well plate they were harvested for experiments. For harvest, cells were washed and resuspended in an electroporation buffer at a concentration of ~3 million cells per mL. The electroporation buffer was iso-osmotic (~300mOsm) with a final conductivity of 100 µS/cm. The exact recipe was 250 mM sucrose, 10 mM HEPES, and 0.4 mM $MgCl_2$[14]. Cells were perfused through the microfluidic device using a syringe pump (PicoPlus, Harvard Apparatus) at a rate of 0.1 µL/min, providing a cell transit time of ~250 ms through the electroporation zone. A total of 25 pulse parameters were applied to cells in transit. The applied electric field strengths were: 0.44 kV/cm, 0.58 kV/cm, 0.70 kV/cm, 0.87 kV/cm, and 1.05 kV/cm. The accompanying pulse durations were: 0.2 ms, 0.8 ms, 1.0 ms, 3.0 ms, and 5 ms, for a total of 15 pulse applications.. The electrical response of each electroporated cell was recorded for analysis. For optical detection studies (i.e. small molecule delivery), the cell suspension was supplemented with propidium iodide (PI) at a final concentration of 100 µM[13].

4.3 Pulse Energy & the Degree of Permeabilization

Initial evidence suggesting our experimental setup is capable of electrically monitoring the degree of cell membrane permeabilization during the electroporation process is shown in **Figure 4.4**. In this parameterized study, the applied electroporation pulse strength and duration were varied, ranging from 0.44 kV/cm – 1.05 kV/cm and 0.2 ms – 5 ms, respectively, with a total of 25 pulse applications used in the study. Referring to **Figure 4.2**, the degree of membrane permeabilization electrical signal is defined as $\Delta I_p/\Delta I_c$. Where ΔI_p is denoted as the permeabilization current, or the change in current following the pulse application and ΔI_c is the current change due to the presence of the cell between the electrodes. Since the magnitude of ΔI_c (see chapter 6) is proportional to the size/volume of the cell, each of the measured responses is therefore normalized by cell size, to help eliminate any variability seen amongst the cell population.

Figure 4.4 is a plot of the degree of membrane permeabilization ($\Delta I_p/\Delta I_c$) versus pulse duration, with the various pulse strengths denoted as a different marker as you move vertically up the plot. It is evident that the degree of membrane permeabilization both increases as you increase the length and strength of the applied electrical pulse. An interesting result is shown when we transition from 0.8 ms to 1.0 ms for the pulse strengths greater than 0.58 kV/cm, where we see a sharp increase in the degree of cell membrane permeabilization. This suggests that the threshold for significant electroporation has been surpassed and is in agreement with other research groups' findings[14-20].

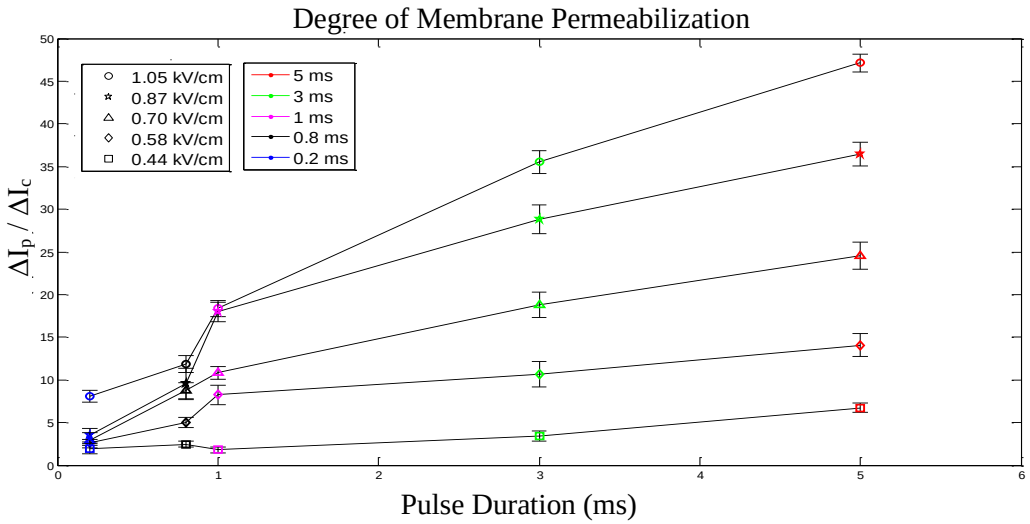

Figure 4.4. Degree of membrane permeabilization—Electrical. The degree of membrane permeabilization (ΔI_p / ΔI_c) increases as the severity (energy) of the pulse increases. Each electric field strength applied (0.44 kV/cm to 1.05 kV/cm) was applied for each pulse duration (0.2 ms to 5.0 ms) tested. Resulting in a total of 25 pulses.

Upon completion of the experimental process shown in Chapter 3, where the applied electrical energy of the pulse application had a strong effect on both cell viability and electro-transfection efficiency, a retroactive analysis was performed on the electrical data shown in **Figure 4.4**. Instead of plotting the results of the parameterized study, each of the pulses were converted into their corresponding applied electrical pulse energy term ($E^2 \times t$, E—Electric Field Strength, t—pulse duration). In this analysis, the x-axis omits the conductivity term (σ, which is a constant) so the values are not truly energy density (J/m^3), however, the relationship between the variables is still the same. This plot is shown in **Figure 4.5**. It is evident that the electrical response indicating the degree of cell membrane

permeabilization is correlated with the total energy of the applied electroporation pulse. For these experiments, a sigmoidal trend is expected, such that at a certain energy threshold a horizontal asymptotic value is reached for the $\Delta I_p/\Delta I_c$ term. Future studies could include further increasing the electrical energy of the pulse applications to see where this value may lie. As well as testing the response of the cell membrane under conditions of high energy pulse applications, but significantly under the electroporation threshold; i.e. a very long duration pulse at a small electric field strength magnitude.

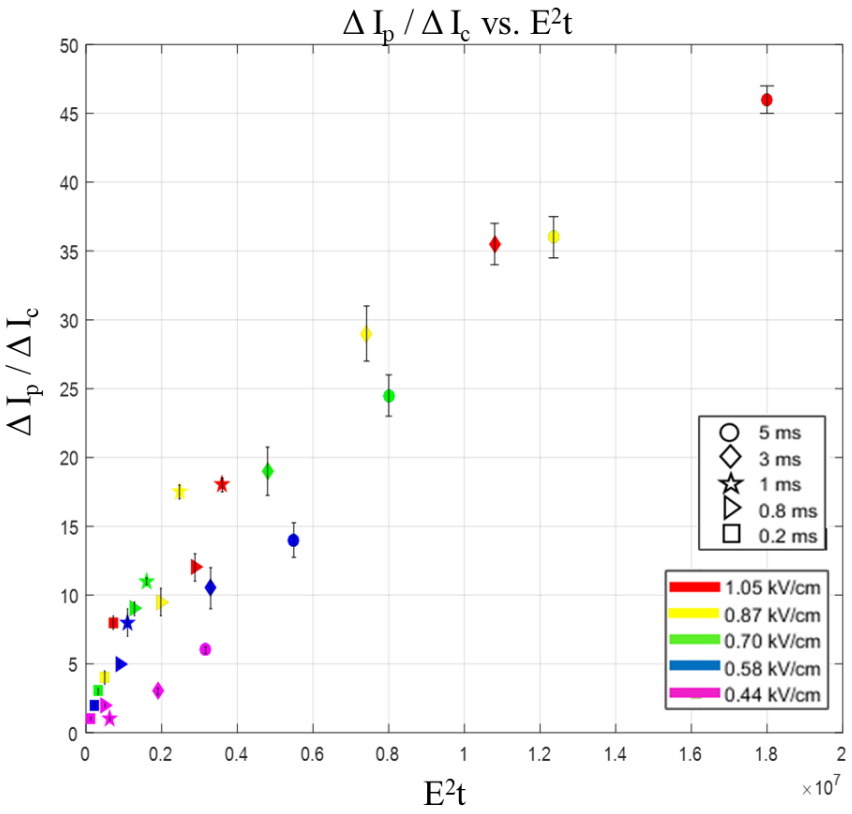

Figure 4.5. Degree of membrane permeabilization vs pulse energy. The electrical signal indicating the degree of cell membrane permeabilization increases with the applied pulse energy. E—electric field strength, t—pulse duration.

4.4 Small Molecule Delivery

To validate that the electrical signal ($\Delta I_p/\Delta I_c$) was indicative of the degree of cell membrane permeabilization another study was performed using propidium iodide (PI). As mentioned in Chapter 2, PI is a commonly used electroporation indicator, as it is naturally impermeable to an intact cell membrane, and following entry into the cytosol, it fluoresces upon binding to nucleic acids[13]. In this study, a CMOS camera (PowerView 1.4MP, TSI) was triggered simultaneously with the application of the electroporation pulse to capture a fluorescent image of the traversing cell. All 25 of the electroporation pulse applications were repeated in this optical study. **Figure 4.6** is a quadrant plot showing the PI fluorescence within an electroporated cell as both the pulse duration (x-axis) and pulse strength (y-axis) increase. It is evident that we see an increase in fluorescence as both parameters are increased which is indicative of an increase in cell membrane permeabilization. Additionally, the hyperpolarization effect of the cell membrane (discussed in Chapter 2) is also witnessed[21].

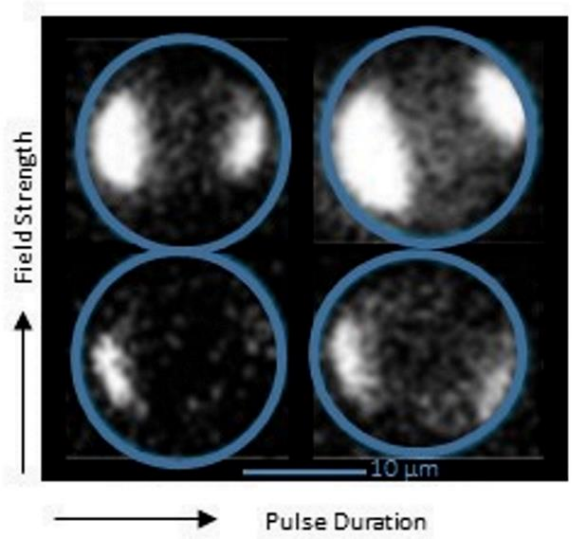

Figure 4.6. Degree of membrane permeabilization—Optical. The quadrant of cells showcases the effect that increasing both the electric field strength and pulse duration have on PI delivery. A similar increase in PI fluorescence is observed compared to the electrical detection of cell membrane permeabilization.

To further verify that the electrical signal is indicative of cell membrane permeabilization, a correlation was performed between the electrical signal ($\Delta I_p/\Delta I_c$ %) and the PI fluorescence intensity (a.a.u.). Where the PI fluorescence was summed and averaged for each pulsing condition. This relationship can be found in **Figure 4.7**. A linear relationship is found between these variables, having a strong correlation constant ($R^2 = 0.93$). The results of this optical, cell membrane permeabilization tracking study verify / validate that our microfluidic electroporation platform is capable of electrically monitoring the electroporation events in real-time.

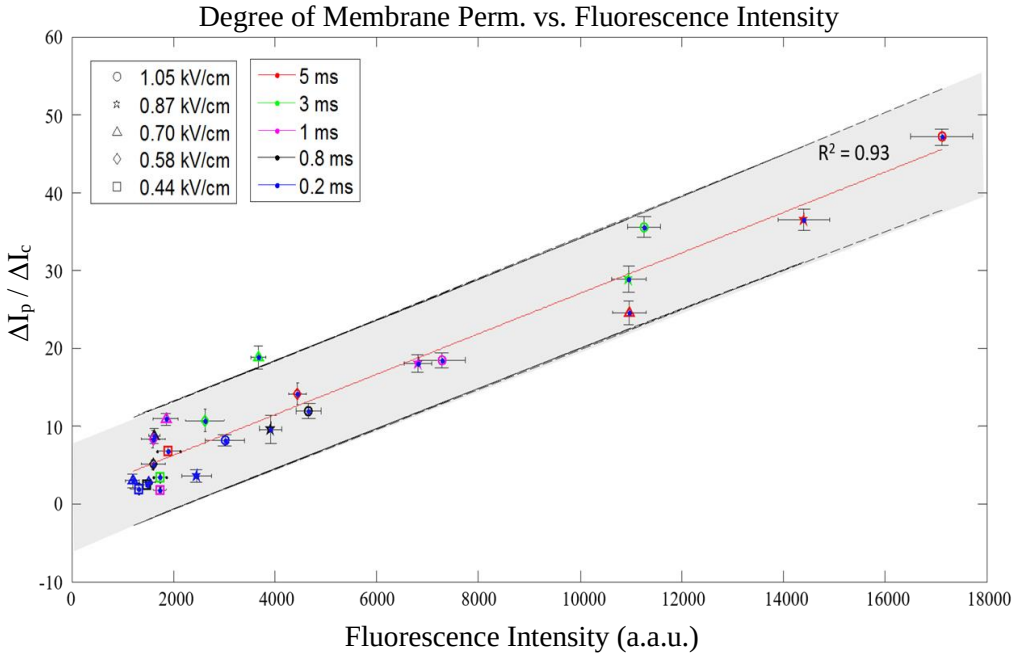

Figure 4.7. Degree of membrane permeabilization—Electrical & Optical. The electrical response of the permeabilized cells is plotted against the optical membrane permeabilization indicator fluorescence intensity for each pulse condition. A strong correlation is observed (R^2=0.93) indicating the electrical signal does represent the degree of cell membrane permeabilization.

4.5 Conclusion

The experimental results highlighted in this chapter builds the foundation for this micro-electroporation technology. The ability to individually sense the degree of cell membrane permeabilization in a serial, flow fashion has previously been unachievable, and thus with further advancement of the technology will allow for an electroporation device capable of performing highly specialized electroporation procedures in a high throughput fashion. The electrical sensing capabilities of the device were verified through the performance of a correlation study, in which the amount of PI fluorescence was strongly correlated with the electrical signal indicating the degree of cell membrane permeabilization ($\Delta I_p/\Delta I_c$). In the upcoming chapter more relevant applications of this technology will be explored and the relationship between $\Delta I_p/\Delta I_c$ and cell viability / electro-transfection efficiency will be addressed.

4.6 Chapter References

1. Huang, Y., & Rubinsky, B. Microfabricated electroporation chip for singe cell membrane permeabilization. *Sensors and Actuators*, 2001, **89**, 242-249.
2. Khine, M., *et al*. Single-cell electroporation arrays with real-time monitoring and feedback control. *Lab-on-a-Chip*, 2007, **7**, 457–462.
3. Guo, X. & Zhu, R. Controllable in-situ cell electroporation with cell positioning and impedance monitoring using micro electrode array. *Scientific Reports*, 2016, **6**, 1-8.
4. Bürgel, S.C., *et al*. On-chip electroporation and impedance spectroscopy of single-cells. *Sensors and Actuators B: Chemistry*. 2015, **210**, 82–90.
5. Zheng, M. *et al.* Continuous-flow, electrically-triggered, single cell-level electroporation. *Technology,* 2017, **5**, 31–41.
6. Zheng, M., *et al.* Hydrodynamically controlled cell rotation in an electroporation microchip to circumferentially deliver molecules into single cells. *Microfluidics & Nanofluidics,* 2016, **20**, 16.
7. Wang, H., & Lu, C. Microfluidic Electroporation for Delivery of Small Molecules and Genes Into Cells Using a Common DC Power Supply. *Biotechnology & Bioengineering*. 2008, **100**, 579-586.
8. Jagtiani, A.V, Carletta, J., & Zhe, J. An impedimetric approach for accurate particle sizing using a microfluidic Coulter counter. *Journal of Micromechanics and Microengineering.* 2011, **21**, 045036.
9. Sun, T., & Morgan, H. Single-cell microfluidic impedance cytometry: a review. *Microfluidics & Nanofluidics.* 2010, **8**, 423–443.
10. Carbonaro, A. & Sohn, L.L. A resistive-pulse sensor chip for multianalyte immunoassays. *Lab on a Chip.* 2005, **5**, 1155–1160.
11. Castellvi, Q., Meradal, B., & Ivorra, B. Assessment of Electroporation by Impedance Methods. *Handbook of Electroporation.* 2016, 1-20.
12. Ivorra A, & Rubinsky B. In vivo electrical impedance measurements during and after electroporation of rat liver. *Bioelectrochemistry*, 2007, **70**, 287–295.
13. Napotnik, T.B., & Miklavcic, D. In vitro electroporation detection methods—An overview. *Bioelectrochemistry*. 2018, **120**, 166-182.
14. Sadik M.M., et al. Scaling relationship and optimization of double-pulse electroporation. *Biophysical Journal*. 2014, **106**, 801–812.
15. Gabriel, B. & Teissié, J. Time courses of mammalian cell electropermeabilization observed by millisecond imaging of membrane property changes during the pulse. *Biophys. J*. 1999, **76**, 2158–2165.
16. Smith, K.C., Neu, J.C. & Krassowska, W. Model of creation and evolution of stable electropores for DNA delivery. *Biophys. J*. 2004, **86**, 2813–2826.
17. Puc, M., *et al*. Quantitative model of small molecules uptake after in vitro cell electropermeabilization. *Bioelectrochemistry*. 2003, **60**, 1–10.
18. Beebe, S.J., *et al*. Nanosecond, highintensity pulsed electric fi elds induce apoptosis in human cells. *FASEB J.* 2003, **17**, 1493–1495.

19. Teissié, J., *et al*. Time dependence of electric fi eld effects on cell membranes. A review for a critical selection of pulse duration for therapeutical applications. *Radiol. Oncol*. 2008, **42**, 196–206.
20. Rols, M.P. & Teissié, J. Electropermeabilization of mammalian cells to macromolecules: Control by pulse duration. *Biophys. J.* 1998, **75**, 1415–1423.
21. Rosazza, C., *et al.* Gene Electrotransfer: A Mechanistic Perspective. *Current Gene Therapy.* 2016, **16**, 98-129.

Chapter 5

Development of a Biosensor for DNA Electro-Transfection

5.1 Study Overview

In this chapter, findings from both Chapter's 3 and 4 are utilized. With respect to Chapter 3, the 'optimized' electroporation buffer and electric pulse application scheme were adapted[1]. Chapter 4 builds the foundation for the work of this Chapter. The evidence presented highlighting this systems' capability to electrically sense the degree of membrane permeabilization is further studied and built upon[2]. In particular, the relationship between the electrical pulse energy density, the degree of cell membrane permeabilization, cell viability, electro-transfection efficiency (eTE), and the electroporation outcome score (viability × eTE) are explored. An important improvement in this experimental design is the inclusion of a long-term, 24 hr, cell viability assessment, compared to the previous short-term viability (not shown)[2]. As well as the delivery and assessment of a clinically relevant DNA plasmid encoding for green fluorescent protein (GFP) allowing for eTE determination. To accomplish these outcomes, system enhancements were introduced for the next generation of both the microfluidic device and external hardware configurations. Briefly, the electroporation region of the microfluidic channel was redesigned to be a straight channel of dimensions 300 μm × 100 μm × 20 μm (L × W × H) (**Figure 5.1**). This produced a larger cross-sectional area compared to the previous constriction geometry, allowing for similar cell transit velocities at higher infusion flow rates, and more importantly, increasing the user-friendliness of the experimental setup. Additionally, the previous hardware setup was limited in the voltage capabilities for electroporation pulsing.

A new hardware setup was implemented, eliminating the need of the Zurich add-on channel (which is limited to 10 Volts maximum)[3]. This hardware setup was built around a high-power op amp (Apex Technologies, PA-90) capable of a V- to V+ voltage supply requirement of 400 Volts (**Figure 5.2**)[4]. These changes will be discussed in context in the following sections.

5.2 Materials & Methods

5.2.1 Device Fabrication

The micro-device consists of a pair of planar, titanium/platinum (Ti/Pt) electrodes on a glass substrate and a polydimethylsiloxane (PDMS) microchannel fabricated via soft lithography[2,5]. The silicon wafer master mold with device features were fabricated using standard photolithographic techniques using the EVG620 mask aligner. The recipes for photolithography were developed following recommended protocols from the photoresist suppliers (MicroChem). The mask was designed using AutoCAD software and manufactured by Cad/ART, with a guaranteed resolution of 8 μm. The electroporation region of the microfluidic device was designed as a rectangular channel of the dimensions 300×100×20 μm^3, the depths of the channels were validated using a surface profiler (DekTak). Prior to pouring PDMS over the silicon master mold, the mold was treated with perfluorodecyltrichlorosilane (SigmaAldrich) to form a self-assembled monolayer to minimize the adherence of PDMS on the SU-8 substrates and increasing the lifetime of the silicon master mold. A 10 : 1 mixture of PDMS polymer and hardening agent were poured over the master mold to create a negative replica and was allowed to cure at 65 °C overnight. The cured PDMS was then surgically cut-off of the master mold and holes were punched to define the inlet (0.75 mm) and outlet (3 mm), to gain fluidic access to the device. Punched PDMS devices were sonicated in an iso-propanol bath to removed debris from the inlets/outlets and then placed in the 65 °C oven overnight to de-swell. Ti/Pt planar electrodes were fabricated via a metal ‘lift-off’ process. Electrode patterns were defined photolithographically on a glass substrate and recesses were chemically etched in a 10 : 1 buffered hydrofluoric acid for 1 minute to a depth of ~200 nm. The metals were deposited

using physical vapor deposition (KJL PVD75, Kurt Lesker). The deposition times for titanium followed by platinum were 8 min and 10 min, respectively. Following deposition, the remaining photoresist was dissolved in an acetone bath to perform the 'lift-off', leaving behind the defined set of Ti/Pt planar electrode traces which were 100 μm in width and 300 μm in separation. The surfaces of the PDMS and electrode substrates were treated under oxygen plasm at 70 W power, 250 sccm O_2, at 350 mTorr for 35 s (PX-250, March Instruments). The activated substrates were aligned under a stereo microscope (SZ61 Binocular Stereo Zoom, Olympus) and irreversibly bonded to form the enclosed microfluidic capillary. Devices were briefly placed on a hot plate at 95 °C to ensure a strong bond. Copper wires were bonded to the planar electrodes via conductive epoxy to allow for electrical connection with the rest of the experiment set-up. A bright field image of the electroporation region of the microfluidic device can be seen in **Figure 5.1**.

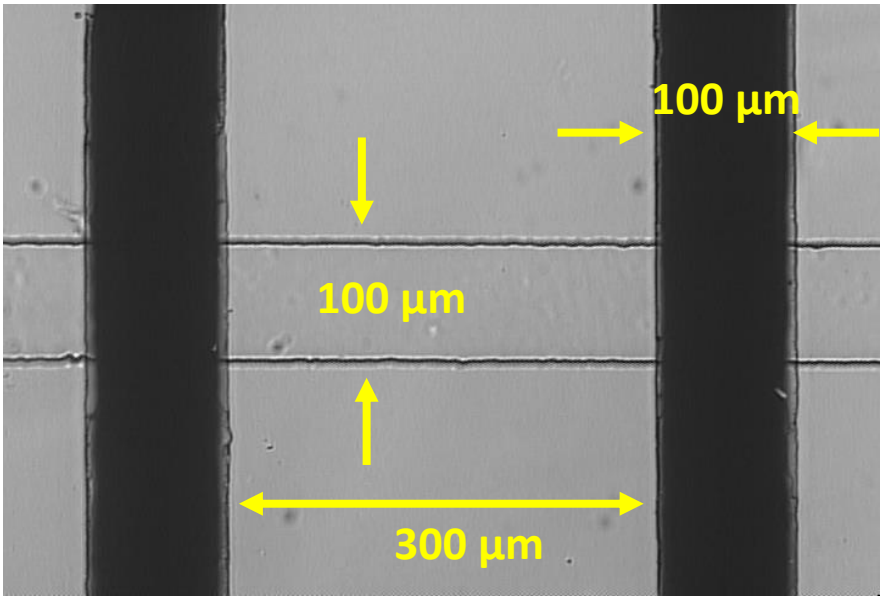

Figure 5.1 Electroporation Region of Microfluidic Device. The electroporation region of the 2nd generation microfluidic device is a simpler design to allow for enhanced experimental usability. The Ti/Pt electrode design is conserved, 100 µm planar electrodes with 300 µm spacing. The microfluidic channel width and height were increased to 100 µm and 20 µm, respectively. This allows for slower transit times at higher initial flow rates when compared to the design in Chapter 4, increasing the overall efficiency of the device.

5.2.2 System Operation

The operation of the automated, detect-pulse electroporation system starts with the perfusion of single cells through the electroporation region of the device (**Figure 5.1**). The electroporation region was altered compared to the previous constriction design to increase the cross-sectional area. This increased cross-sectional area allows for higher infusion flow rates without altering the cell transit time, $Q = v \times A$, where Q is flow rate [m^3/s], v is velocity [m/s], and A is cross-sectional area [m^2]. Although, this change decreases the cell-volume fraction within the electroporation region, the electrical sensing system did not forfeit the ability to detect and pulse the cells in transit. Instead, an enhancement with this experimental setup and performance was introduced, eliminating much of the need for experimental user-interference to result in reliable, single cell passages through the electroporation region. In addition to the microfluidic design changes, the accompanying electronic circuitry was also upgraded to enhance the electroporation pulse electric field strength capabilities.

The previous experimental setup was limited on the voltage capabilities for the applied electric field strength. In particular, the Zurich add-on channel, used to superimpose the square-wave pulse, has an upward limit of 10 Volts[3]. Though this did not limit the functionality for delivering the small molecule, propidium iodide (PI), a larger range of electric field strengths would be necessary to test the technology's ability to deliver the much larger biomolecule, plasmid DNA. To this end, the electronic and hardware experimental set-up were built around an external, high-power op amp (Apex Technologies, PA-90).

A schematic of the new electronic/hardware set up is found in **Figure 5.2**, centered around the PA-90 op amp. Both a positive and negative power supply voltage are required to power the circuitry, with a maximum V- to V+ of 400 Volts[4]. In this setup, a power supply was used to generate the V- of -15 Volts (E3631A DC Power Supply, Agilent) and a function generator (33220A Waveform Generator, Agilent) was set to a DC offset of 2 Volts, which was set to the input of a 50X amplifier (Model 2350, TEGAM) to generate V+ of 100 Volts (note, this voltage could be increased to allow for higher electric field strengths to be applied). The Zurich HF2LI lock in amplifier signal output channel outputs a 1 V_{p-p} sine wave at a frequency of 1.224 kHz to excite the device-under-test (DUT) which allows for the detection of membrane permeabilization[2,6-8]. The voltage in the DUT is monitored at the 2nd electrode by the HF2TA current pre-amplifier and the current is then sent to the lock-in signal input. This signal is sent to a custom-built LabVIEW algorithm (see chapter 6) which detects a sharp decrease in current when a cell enters the electroporation region and automatically outputs a TTL digital output to trigger the application the prescribed electroporation pulse from a function generator (33220A Waveform Generator, Agilent). The pulse from the function generator was also fed into the 50X, high-voltage amplifier (Model 2350, TEGAM) to amplify to the pulse to the desired strength. The amplified pulse was superimposed onto the 1 V_{p-p} sine wave through the use of the high-power op amp (PA-90). All-the-while during this process, the LabVIEW algorithm is continuously monitoring the change in current before and after pulse application to the cell in transit. Upon cell exit, the baseline current reading is restored, and the system then awaits the entry of the next cell where this process will then repeat itself.

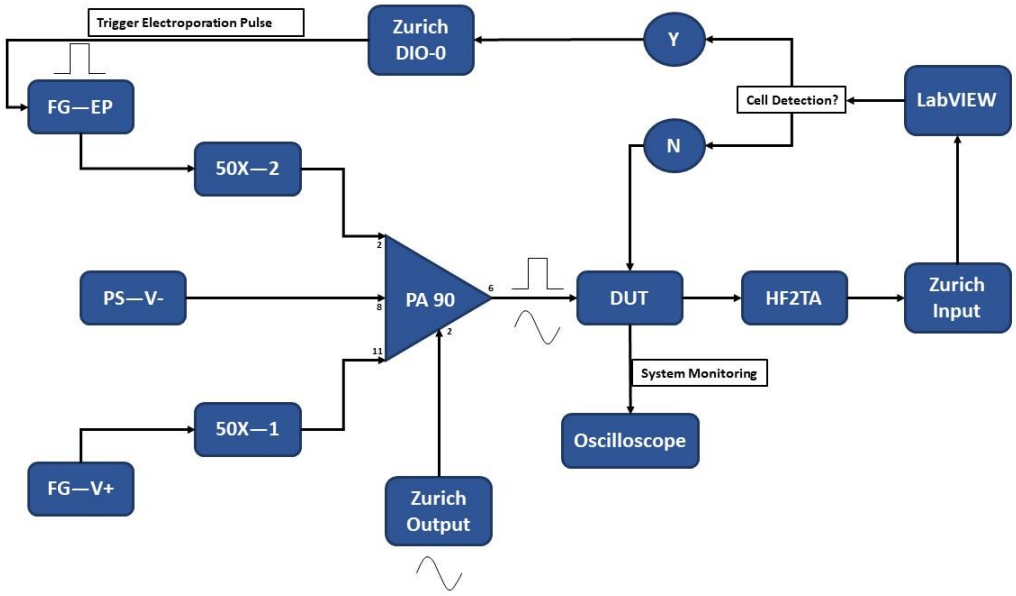

Figure 5.2. Schematic of System Operation. Due to the need of higher applied voltages to perform the DNA transfections a next generation hardware platform required development. Particularly is the integration of the high power op-amp (PA 90) which allows for the superimposition of a high voltage DC square wave electroporation pulse on the Zurich Output AC lock-in signal. Legend: PA-90 (high power op amp), DUT (device under test), HF2TA (current pre-amplifier), DIO (digital input/output), FG—EP (function generator / electroporation pulse), 50X (50X amplifier), PS—V- (power supply / negative voltage for PA 90), FG—V+ (Function Generator, positive voltage for PA 90).

5.2.3 Experimental Design

Mouse 3T3 fibroblasts cells were cultured in DMEM supplemented with 10% FBS, 1% L-glutamine, and 1% penicillin/streptomycin (Sigma Aldrich, St. Louis, MO). Cells were passed 24 hours prior to experimentation such that they reached 70%-80% confluency in a 6-well prior to harvest. For harvest, cells were washed and resuspended in an electroporation buffer at a concentration of ~3 million cells per mL containing DNA plasmid (pDNA) encoding for green fluorescent protein at a final concentration of 20 µg/mL (pMAX-GFP, Lonza, Walkersville, MD). The electroporation buffer was iso-osmotic (~300mOsm), pH of 7.4, and had a final conductivity of 500 µS/cm. The exact recipe was 250 mM sucrose, 10 mM HEPES, 3 mM NaOH, 1 mM KCl, and 0.7 mM $MgCl_2$[1]. Cells were perfused through the microfluidic device using a syringe pump (PicoPlus, Harvard Apparatus) at a rate of 0.3 µL/min, providing a cell transit time of ~250 ms through the electroporation zone. Pulsing parameters were chosen such that the total ionic charge movement per unit area, i.e. charge flux ($\Phi_Q = \sigma \times E \times t$), was held constant. Where Φ_Q is charge flux [C/m^2], σ is buffer conductivity [S/m], E is electric field strength [V/m], and t is pulse duration [s]. The pulses tested, in increasing electrical energy density ($\sigma \times E^2 \times t$, [$J/m^3$]), were: 0.4 kV/cm : 3 ms, 0.8 kV/cm : 1.5 ms, 1.0 kV/cm : 1.2 ms, 1.2 kV/cm : 1.0 ms, 1.8 kV/cm : 0.67 ms, 2.4 kV/cm : 0.5 ms. The electrical recording and the electrical response of each electroporated cell was recorded for analysis (**Figure 5.3**).

Similar to Chapter 4, the electrical response of the cell membrane indicative of membrane permeabilization was determined, however, in this body of work, the degree of membrane permeabilization was plotted against applied pulse energy density. Due to a combination of higher energy pulses and a higher conductivity electroporation buffer in these

experiments, an alternative method was necessary to determine the degree of cell membrane permeabilization (ΔI_p / ΔI_c). Following pulse application, an inevitable electrical artifact was introduced into the electrical recording, masking the ability to determine ΔI_p in the fashion that was performed in Chapter 4. Instead, a second ΔI_{c2} term is introduced, which is the magnitude of the cell current drop after the cell is electroporated. Taking the difference between the initial current drop, ΔI_{c1}, and the ΔI_{c2} term, the degree of membrane permeabilization ΔI_p, can be recovered. Please refer to **Figure 5.3** for a visualization of this calculation.

In addition to correlating the degree of membrane permeabilization to the applied pulse energy, a relationship between these two variables with cell viability and eTE was also explored. Briefly, following each experimental condition (n=3), cells were re-plated in a 96 well plate (0.3 cm^2 surface area) in antibiotic-free full DMEM[1]. Following 24 hours cells were assessed for both cell viability and eTE using bright field and epifluorescence microscopy (FITC filter), respectively (Microscope: Olympus IX81, Japan, Camera: Hamamatsu Photonics, Model: C4742-95-12G04, Japan, Software: MetaMorph). The captured images using a 10× objective in combination with the camera result in a field-of-view (FOV) of 0.006 cm^2. To calculate cell viability, the total number of cells perfused through the device was estimated based on the electrical recording, and an average estimated cell number per 10× objective imaging field was determined based on the ratio of the 96 well plate surface area to the FOV (1 : 50). An example calculation is shown in the accompanying section. The eTE was simply calculated as the percentage of the number of GFP(+) cells to the total number of viable cells.

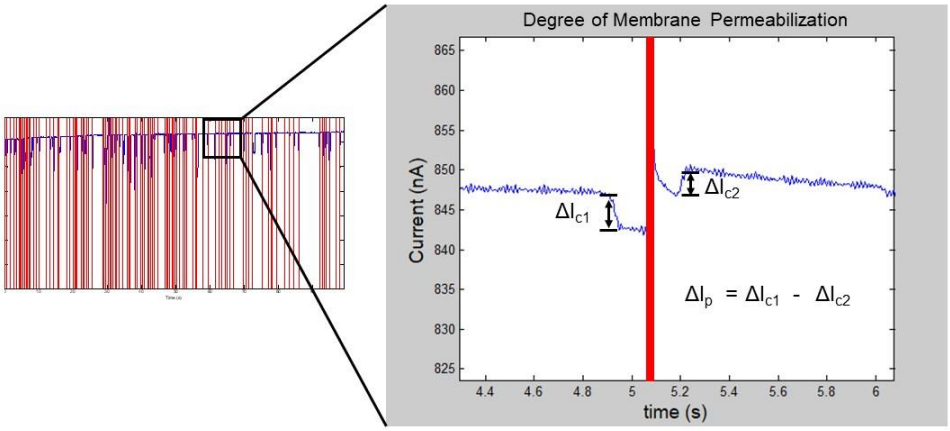

Figure 5.3. Electrical Recording and Degree of Membrane Permeabilization. Following experimentation, electrical recordings (Left) were analyzed in MATLAB to determine the overall number of cells that traversed the device and received a pulse application. This information is used to determine the resulting cell viability 24 hours later. (Right) Zoomed in recording of a single cell receiving a pulse application (red line) and the resulting membrane permeabilization response. Note the difference in the response due to the higher energy pulse application, resulting in the need for a new method to determine the degree of cell membrane permeabilization (ΔI_p / ΔI_c).

5.3 Pulse Energy & Degree of Membrane Permeabilization

A plot of the degree of cell membrane permeabilization versus applied electrical energy density is shown in **Figure 5.4**. The trend found corroborates with the retro-active data analysis plot shown in Chapter 4, where it is found that the degree of cell membrane permeabilization increases with increasing applied electrical pulse energy density. The shape of the plot resembles that of a sigmoidal curve, with the exponential increase occurring in the range of $\Delta I_p / \Delta I_c$ values of approximately 30% to 45%. The relationship between this electrical measurement and the electroporation outcome score (a metric that accounts for both the cell viability and the eTE outcomes) is discussed in a future section. However, the evidence supports the fact this electrical measurement can provide real-time feedback, acting as a microfluidic biosensor, to ultimately determine optimal pulsing conditions for the electroporation experiment.

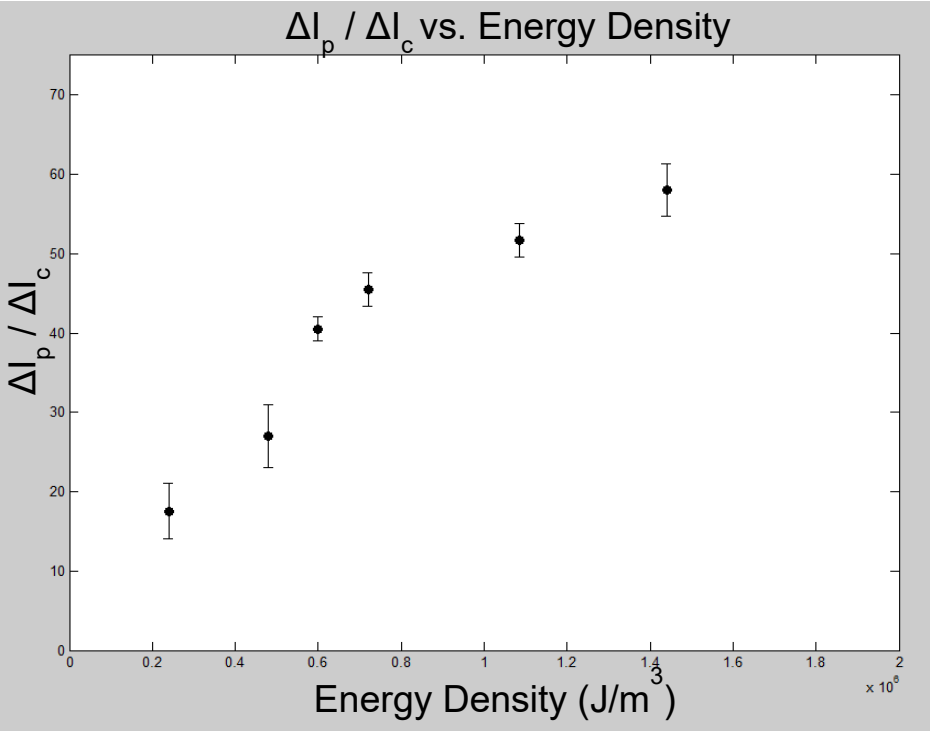

Figure 5.4. Degree of Cell Membrane Permeabilization versus Energy Density. Data is represented as σ ± std (n=3). A total of 150 cells were analyzed at each condition. The electrical response of the cell membrane behaves similarly as was shown in Chapter 4. A sudden increase in permeabilization is shown following the 2nd data point, with the degree of membrane permeabilization approaching an asymptotic value at higher energy pulse applications.

5.4 Pulse Energy & Cell Viability

To determine cell viability of our microfluidic device, a new assay was developed, taking advantage of the technology's electrical sensing capabilities. Briefly, following each individual experimental run, cells were removed from the microfluidic outlet and re-plated in an individual 96 well plate containing antibiotic free full DMEM media. After 24 hours, cells were then imaged for cell viability. The viability assay is an estimate based on the total number of cells that traversed the microfluidic device for that given experiment and the ratio of the surface area of the 96 well plate (0.3 cm^2) to the FOV of the 10× objective/camera (0.006 cm^2). The total cell count was determined through post-experiment analysis of the electrical recording to determine the total number of cells that had traversed the device. The ratio of the 96 well plate surface area to the FOV is a factor of 50. For example, in an arbitrary case that the estimated cell number is 1000 (from the electrical recording), you would expect 20 cells per 10× image (1000/50), assuming that the cells were uniformly distributed along the surface of the plate. Therefore, if you captured 5 images and only counted 90 cells, the viability would be 90% (cells counted / cells expected, i.e. 90 / 100).

Using this assay, the relationship between cell viability and electroporation pulse energy density is shown in **Figure 5.5**. As expected, and in agreement with our previous works and works of others, as pulse energy density increases, we see a decrease in the corresponding cell viability. The vertical red line is representative of the energy region where the cell viability initially begins to drop-off. Prior to the red line, the cell viability is unaffected with estimated cell viabilities greater than 100%. This is likely due to an underestimation of the total cell count from the electrical recording. In particular, it is

difficult to differentiate if a cluster of multiple cells entered the electroporation region together, how many cells exactly were contained in that cluster. As the current drop is proportional to the volume of fluid displaced, it is hard to estimate the total cell count of the cluster given each of the cells will be of different sizes. Regardless, the overall trend shown in **Figure 5.5** would be conserved which is the important result of the study, not the exact magnitude of the numbers. The eTE is shown in the next section, which had a more reliable metric for calculation.

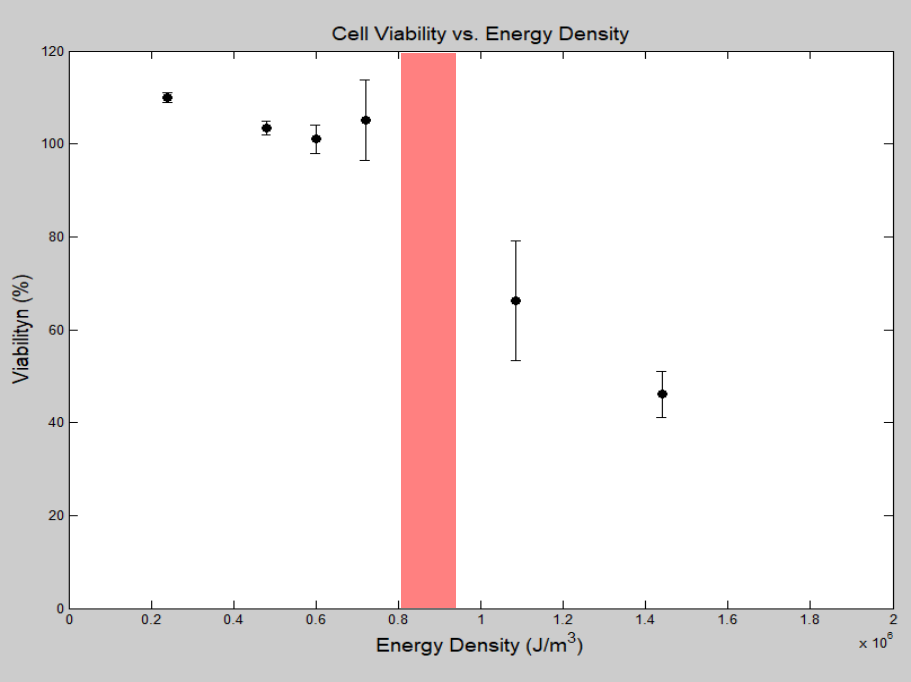

Figure 5.5. Cell Viability versus Energy Density. 24 hours following experiments cell viability was determined via bright field imaging of a 96 well plate. Data is represented as σ ± std (n=3). To calculate viability the total number of cells were counted and normalized to the total number of expected cells. The expected cell count is based on the electrical recording cell number, the field of view of the microscope camera, and the area of a single well in a 96 well plate. For example, an expected total cell number of 1000 would result in an expected cell number of 20 cells per 10X image. As expected, with increasing pulse energy, the viability decreased. The red bar indicates the pulse energy region when we begin to see this drop-off in viability.

5.5 Pulse Energy & Electro-Transfection Efficiency

When assessing the eTE at 24 hours, the assay to determine this value is not as complicated as the accompanying cell viability. To determine the eTE, it is simply the ratio of the total number of GFP(+) cells to the total number of viable cells. The relationship between eTE and electroporation pulse energy density is shown in **Figure 5.6**. As expected, an increase in eTE is found with increasing pulse energy density[1,9,10]. The vertical green region indicates the threshold of energy for a single pulse application at which a sharp increase in eTE is observed. In particular, this occurred with the 1.0 kV/cm : 1.2 ms pulse application. Prior to this region, the weaker energy pulses were not capable of disrupting the membrane sufficiently and/or electrophoretically driving the pDNA molecules close enough to the membrane such that they could be taken up via endocytosis[11,12]. On the other side of the spectrum, the high energy pulse applications approach a horizontal asymptotic value at ~90% eTE. Taking both the cell viability and eTE data into account, an optimization metric termed the electroporation outcome score is described in the next section to determine the optimal pulse energy for the 3T3 cell line.

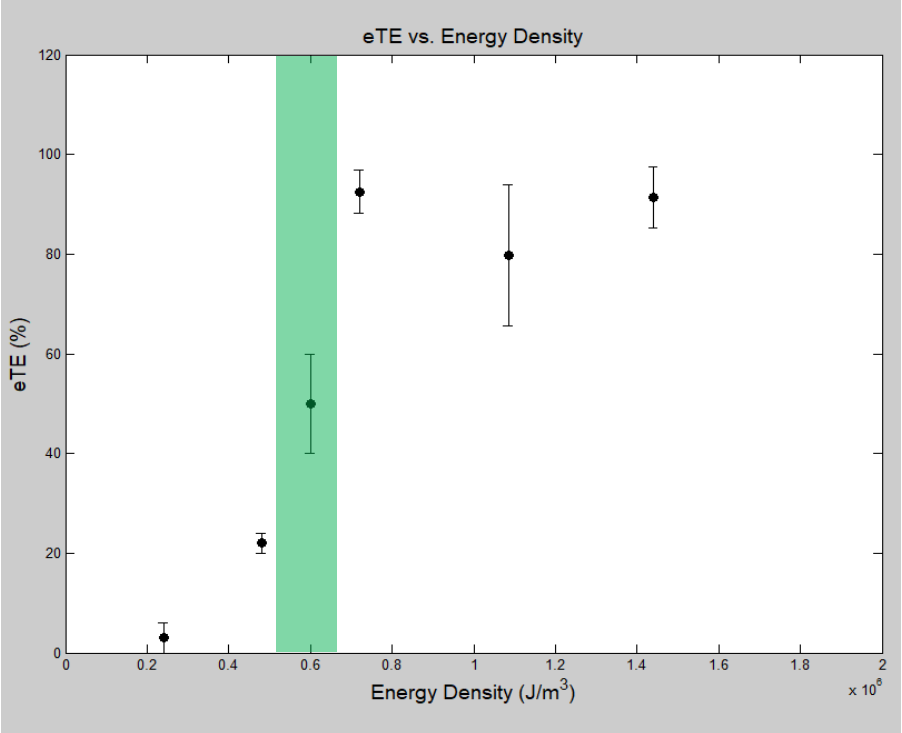

Figure 5.6. Electro-Transfection Efficiency versus Energy Density. The electro-transfection efficiency (eTE) was determined as the total number of GFP(+) cells to the total number of viable cells. Data is represented as σ ± std (n=3). As expected, eTE increases with increasing pulse energy. The green indicates the region of pulse energy where the eTE begins to increase, at which it approaches an asymptotic value.

5.6 Electroporation Outcome Score, Pulse Energy, & Degree of Membrane Perm.

As previously introduced in Chapter 3, the electroporation outcome score is a unitless metric used to discriminate amongst electroporation outcomes[1]. In particular, the outcome score is the product of the cell viability percentage and the eTE percentage, normalized to a maximum score of 100 (the ideal maximum of 100% viability and 100% eTE). **Figure 5.7** is a scatter plot of the experimental results previously shown, however, now representative of the electroporation outcome scores. The lower energy pulse applications ride along the top of the y-axis as these conditions all had viabilities greater than 100%. However, the accompanying eTE results were low due to under permeabilization of the cell membrane, which puts them at a lower overall outcome score (See **Figure 5.8**). For this experimental data set, the 1.2 kV/cm : 1 ms pulse application (red in **Figure 5.7**) had the highest scores, greater than 90, indicating this pulse application was sufficient at delivering the pDNA without over-permeabilizing the cell membrane to cause irreversible damage. The over-permeabilization cases occur for the final 2 pulse conditions which had the highest applied energy density. In these cases, there was sufficient pDNA delivery, but due to the irreversible cell membrane damage affecting the cell viability, these conditions' scores suffered. A better representation of this data can be found in **Figure 5.8**, which is a plot of the electroporation outcome score versus applied electrical pulse energy density.

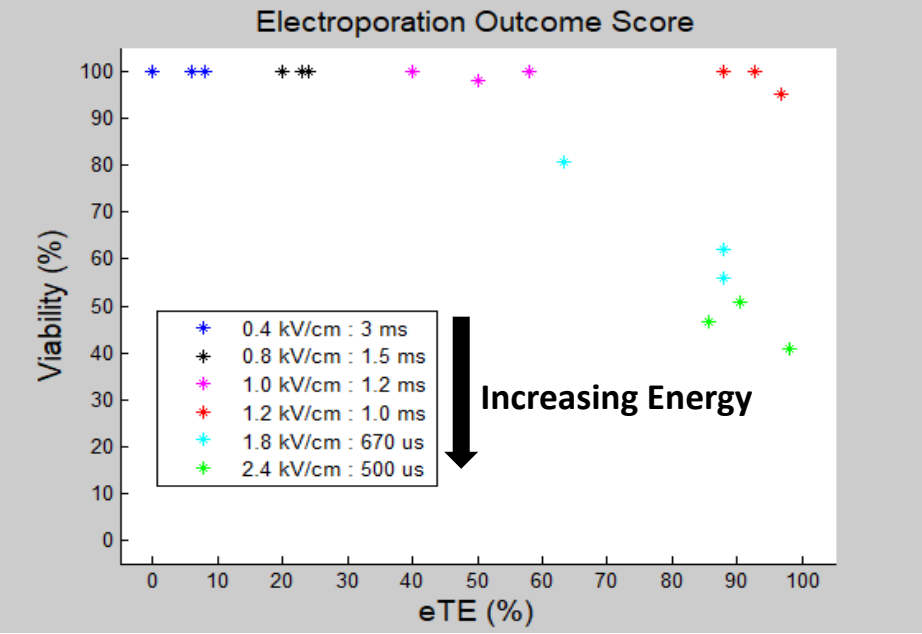

Figure 5.7. Electroporation Outcome Score. This data is represented as a scatter plot (n=3). The electroporation outcome score is a unitless metric, which is the product of the cell viability (y-axis) and electro-transfection efficiency (eTE, x-axis). The ideal results would be 100% viability and 100% eTE, in the uppermost right corner. The pulse application of 1.2 kV/cm : 1.0 ms resulted in highest outcomes (>90) in these experiments.

The trend of the electroporation outcome score may better be described through the visualization shown in **Figure 5.8**, a plot of the electroporation outcome score versus applied electrical energy density. In this case, the 3 regions previously mentioned are better depicted. The first case, to the left of the green/red color spectrum, is the case of under-permeabilization resulting in low eTE. Though these pulses resulted in high cell viability, the lack of GFP expression makes the outcomes undesirable. On the opposite side of the green/red spectrum, the case of over-permeabilization is observed. Though these scores are higher than the under-permeabilized conditions, they are still sub-optimal due to the severe drop-off in cell viability that occurs from the high energy pulse applications. Lastly, the green/red spectrum is representative of the optimal range of applied electrical energy density for highly desirable outcomes.

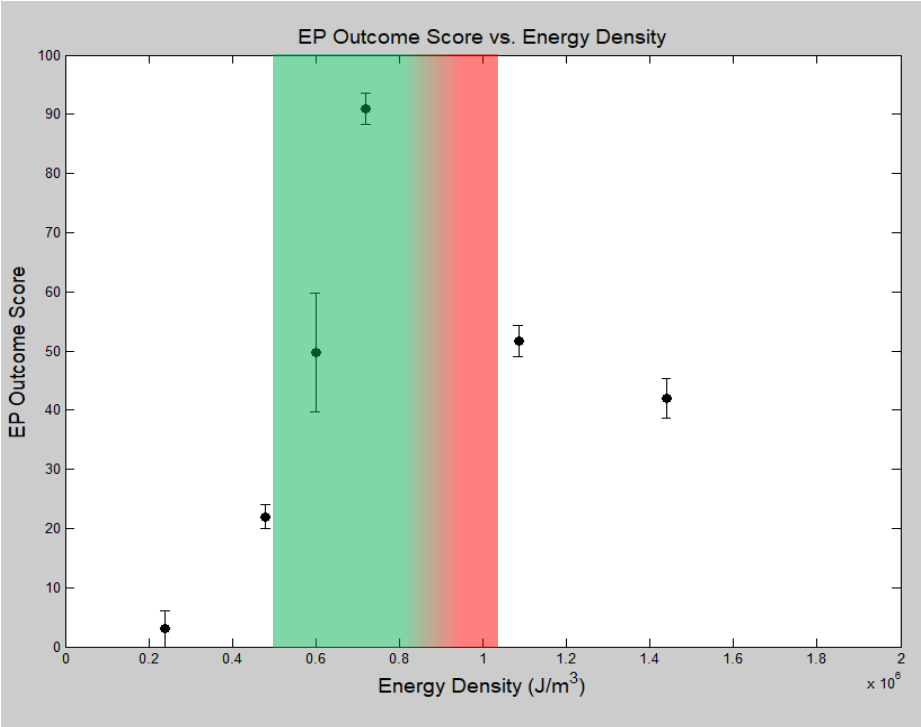

Figure 5.8. Electroporation Outcome Score versus Energy Density. Data is represented as σ ± std (n=3). The outcome score shows 3 distinct regions. The farthest left results have low outcome scores due to the lack of transfection, although cell viability was unperturbed. The farthest right we have higher scores, but still outside of the optimum range (center), where we have good transfection, but the cell viability is affected by the high energy pulse application. The center region (green/red) is the optimum pulse energy for the highest outcomes, resulting in both good viability and good transfection efficiency.

The last comparison made in this study highlights the importance of the electrical sensing data in optimizing the electroporation pulsing parameters. This is shown in **Figure 5.9**, where the electroporation outcome score is plotted against the degree of cell membrane permeabilization for each of the pulsing conditions. Since the degree of membrane permeabilization was shown to be positively related to the pulse energy, we see a similar shape in the curve when compared to **Figure 5.8**. However, **Figure 5.9** gives more insight into the usefulness of the microfluidic technology under development, which has been described throughout this body of work. In particular, the use of this electrically measured term serves as an indicator as to the effect of the applied pulsing conditions on the cell membrane and how these conditions are ultimately going to affect the outcome of the electroporation. Therefore, the range highlighted in the green/red spectrum in **Figure 5.9** indicates the optimum electrical signal for cell membrane permeabilization to maximize both cell viability and eTE.

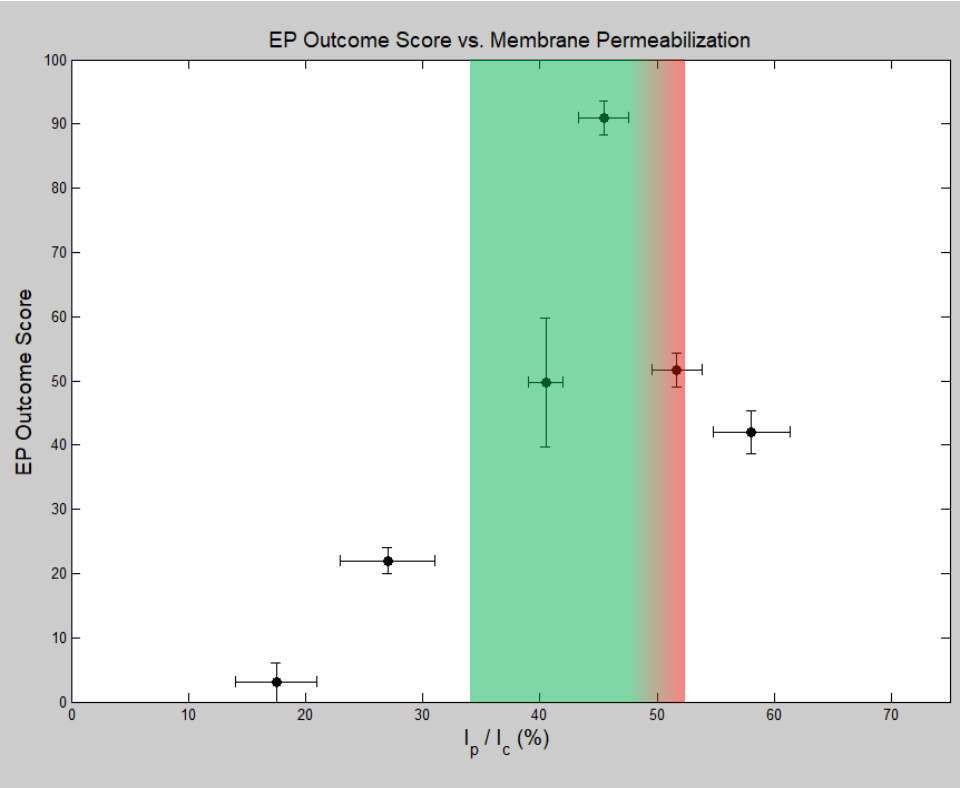

Figure 5.9. Electroporation Outcome Score versus Degree of Cell Membrane Permeabilization. Data is represented as σ ± std (n=3). Using the electrical term indicative of the degree of cell membrane permeabilization as the independent variable, we see a similar trend as Figure 5.8. This indicates this micro-electroporation platform can be utilized as a biosensor in the optimization of an electroporation experimental procedures. Highlighting the ΔI_p / ΔI_c range of 35% to 50% to be ideal for good electroporation outcomes.

5.7 Utilizing the Micro Electroporation Platform as a Biosensor

The previous section highlights the effects that both pulse energy density and the degree of cell membrane permeabilization have on the electroporation outcome score (**Figure 5.8** and **Figure 5.9**, respectively). In the case of pulse energy density, there exists a region of optimal pulsing conditions (represented by the green/red in **Figure 5.8**) for maximizing the electroporation outcome score, i.e. high viability and high eTE. This range of pulse applications represents a zone for further optimization (i.e. application of pulse trains, or different pulse waveforms, etc.) to occur to enhance the electroporation outcomes[13,14]. For example, a user could test multiple pulse applications on the lower energy density side of this spectrum or possibly test pulses of variable magnitudes, starting with a more severe pulse closer to the red side of this spectrum, followed by a lower magnitude, longer duration pulse to deliver materials[9].

Although this information is valuable and provides insight into optimization of electroporation conditions, it requires the determination of cell viability and eTE 24 hours following experimentation. Ultimately, this time lag is not ideal in an experimentation setting when trying to optimize conditions for precious cell types. In **Figure 5.4**, the electrical parameter, $\Delta I_p/\Delta I_c$, indicating the degree of membrane permeabilization was shown to be positively correlated with increasing pulse energy density. Furthermore, **Figure 5.9** shows an optimal region of $\Delta I_p/\Delta I_c$ values for maximizing electroporation outcomes. Since this electrical term can be calculated in real-time, and its effect on cell viability and eTE follow a similar trend to that of the applied pulse energy density, this infers that the micro electroporation device can operate as a biosensor, utilizing the $\Delta I_p/\Delta I_c$

values to determine optimal pulsing conditions, eliminating the lag time typically found when optimizing electroporation conditions.

Therefore, the technology's ability to sense the degree of cell membrane permeabilization in real-time will eliminate the need for empirically derived electroporation protocols, all-the-while optimizing the electroporation pulsing conditions for a given cell type and for a given experimental parameters. The next sections and chapters will touch on the future of this technology in respect to performing real-time feedback-controlled electroporation, increasing the device's capacity to handle higher cell throughputs, and testing different cell types / molecules of interest for delivery.

5.8 Conclusion / Future Directions

The work presented in this Chapter, builds upon Chapter 4 where the initial evidence showcasing this technology's capabilities to electrically sense the state of the cell membrane during the electroporation process. In this Chapter the effect of applied electrical energy density on cell membrane permeabilization, cell viability, and eTE is explored. Supporting results to the retro-active data analysis study presented in Chapter 4 were shown, that being the degree of membrane permeabilization is dependent on the applied electrical pulse energy density. With respect to cell viability and eTE, similar trends were found to that of the bulk electroporation experiments in Chapter 3. The trends being that the cell viability decreases with increasing applied electrical energy and the eTE increases with increasing applied electrical energy. However, when looking at the electroporation outcomes, it is shown that performing electroporation on the single cell level outperforms the bulk electroporation analogue. The micro-scale electroporation work presented within this Chapter had a maximum outcome score of 92 a.u., which is significantly greater than the maximum outcome score reached in the bulk electroporation work of 52 a.u. (Chapter 3). Lastly, the electroporation outcome score was plotted against the electrical measurement (ΔI_p / ΔI_c) indicative of the degree of cell membrane permeabilization. This curve had similar trend to that of the outcome score versus applied electrical energy density which is used as an optimization curve. This evidence shows the importance of being able to monitor the degree of cell membrane permeabilization during the electroporation process, such that this technology can act as a biosensor to optimize electroporation conditions.

Future work entails the further development of this technology, in particular, the development of a single cell, real-time, feedback-controlled electroporation platform. Details on this idea are provided in the next Chapter. Furthermore, future work requirements for the advancement of this technology include increasing the overall throughput capabilities of the microfluidics. As well as validating this micro-electroporation platform with different cell types and expanding upon the applications this device can accomplish. Preliminary results and ideas are discussed in the final chapter (Chapter 7) on these matters.

5.8 Chapter References

1. Sherba, J.J., *et al*. The effects of electroporation buffer composition on cell viability and electro-transfection efficiency. *Nature Scientific Reports*, 2020 **10**, 3053.
2. Zheng, M. *et al.* Continuous-flow, electrically-triggered, single cell-level electroporation. *Technology*, 2017, **5**, 31–41.
3. Zurich Instruments AG. HF2 User Manual. 2020.
4. Apex Microtechnology Inc. High Voltage Power Operational Amplifiers. 2019.
5. Zheng, M., *et al.* Hydrodynamically controlled cell rotation in an electroporation microchip to circumferentially deliver molecules into single cells. *Microfluidics & Nanofluidics,* 2016, **20**, 16.
6. Castellvi, Q., Meradal, B., & Ivorra, B. Assessment of Electroporation by Impedance Methods. *Handbook of Electroporation.* 2016, 1-20.
7. Ivorra A, & Rubinsky B. In vivo electrical impedance measurements during and after electroporation of rat liver. *Bioelectrochemistry*, 2007, **70**, 287–295.
8. Napotnik, T.B., & Miklavcic, D. In vitro electroporation detection methods—An overview. *Bioelectrochemistry*. 2018, **120**, 166-182.
9. Sadik M.M., et al. Scaling relationship and optimization of double-pulse electroporation. *Biophysical Journal*. 2014, **106**, 801–812.
10. Madison, A.C., *et al.* Scalable Device for Automated Microbial Electroporation in a Digital Microfluidic Platform. *ACS Synthetic Biology.* 2017, **6**, 1701-1709.
11. Mao M., *et al*. Involvement of a Rac1-Dependent Macropinocytosis Pathway in Plasmid DNA Delivery by Electrotransfection. *Molecular Therapy*. 2017, **25,** 803–815.
12. Wu M., & Yuan F. Membrane Binding of Plasmid DNA and Endocytic Pathways Are Involved in Electrotransfection of Mammalian Cells. *PLOS ONE*. 2011, **6**, 1–9.
13. Rebersek, M., *et al*. Electroporator with automatic change of electric field direction improves gene electrotransfer *in-vitro*. *BioMedical Engineering OnLine*. 2007, **6**, 1-11.
14. His, P., *et al.* Acoustophoretic rapid media exchange and continuous-flow electrotransfection of primary human T cells for applications in automated cellular therapy manufacturing. *Lab on a Chip*. 2019, **19**, 2978.

Chapter 6

Movement Towards a Smart Electroporation Technology

6.1 Chapter Overview

In this chapter, the current state of the feedback control algorithm will be discussed in detail. Initially, a high-level description will be provided. The algorithm is broken up into 2 separate phases, phase I the ΔI_c calculation in real-time and phase II the pulse application, real-time cell membrane permeabilization monitoring, and pulse cut-off. Verification / validation methods for phase I are described, confirming the accuracy of this portion of the algorithm. For phase II, the current state of the technology is discussed, including current challenges and technical hurdles that will need to be overcome to move forward with the single-cell level, microfluidic feedback-control electroporation technology. Lastly, the idea of performing a 'population'-based feedback control is introduced.

As was previously discussed in Chapter 2, the idea of performing 'smart' electroporation is not a new concept, with different groups showing the capabilities to electrically sense the event of electroporation on static or 'pseudo'-static cells[1-5]. Additionally, some groups have developed tissue-level feedback-controlled electroporation technologies[6,7]. The idea of single-cell feedback control was first introduced in the *Khine et al* work in 2007[3]. Another group performs 'feedback' control in a fluidic environment, however, using the device as a Coulter Counter (phase I of our technology) paired with finite element modeling of electroporation to predict what pulse should be applied to the cell passing through the microfluidic electroporation region[8]. Though this device is technically single-cell level 'feedback'-controlled micro-electroporation, it differs drastically to the technology

discussed within this body of work. The innovation and novelty of our device is the ability to actively sense the degree of cell membrane permeabilization in real-time on an individual cell basis in a continuous flow environment[1].

6.2 Feedback Algorithm

A common electrical recording is shown in **Figure 6.1**, labeled 1-3 to help aid in the explanation of the operation principles of the feedback-control algorithm. The algorithm is broken down into 2 distinct phases. Phase I (1—2) is the accurate calculation of the current drop, ΔI_c. This portion of the algorithm functions as a microfluidic Coulter Counter[9,10]. The algorithm is a point-by-point, slope-based, threshold detection system. Upon cell entry into the electroporation region, a sharp spike in current is observed, which trips the algorithm to detect the cells presence (1). The system then waits for the occurrence of an inflection point (i.e. slope changes from negative to positive value) (2). Once the inflection point is detected, the ΔI_c value is determined, all-the-while moving to phase II of the algorithm (2—3). The electroporation pulse is immediately administered to the cell in transit (red line) and the permeabilization current (ΔI_p) is calculated in real-time (3). Depending on the threshold percentage set by the user (ΔI_p / ΔI_c) additional pulses will be administered (in the case of T_2) until the threshold is surpassed (in the case of T_1). The cell then exits the electroporation region and the algorithm returns to the monitoring phase, awaiting the next cell detection event.

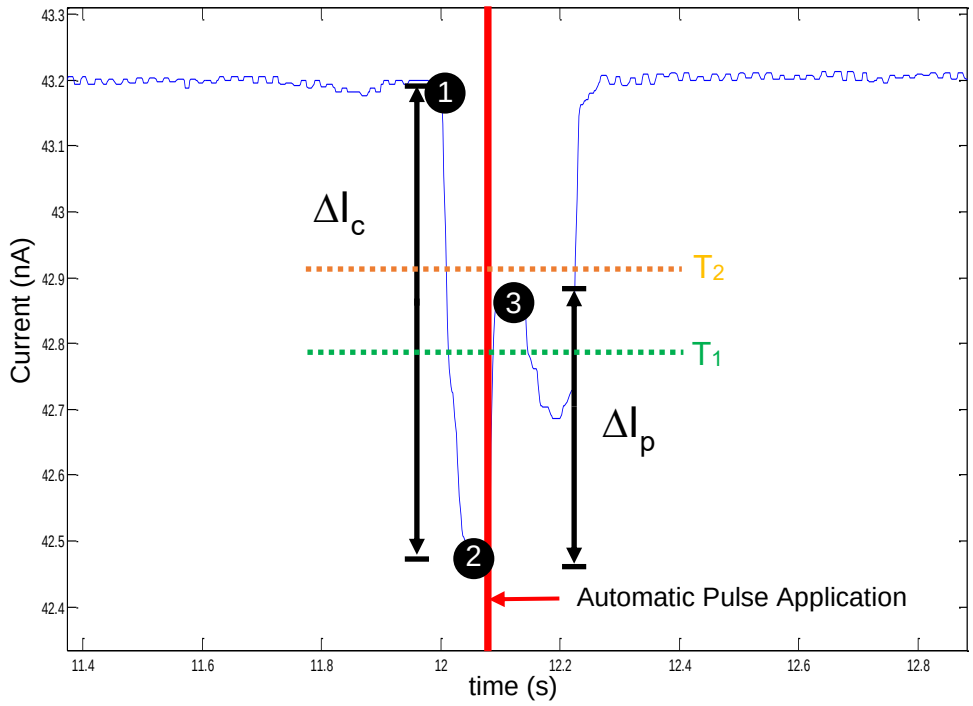

Figure 6.1. Feedback Control Algorithm. The basics of the single-cell feedback control algorithm can be broken into 2 phases, cell size determination (1-2) and pulse administration / cut-off (2-3). In this depiction, location 1) represents the point of cell entry at which the algorithm detects the presence of the cell. Location 2) represents the inflection point where the cell size can be calculated (ΔI_c) and the simultaneous application of the electroporation pulse (red line). Location 3) represents the threshold-based pulse cut-off point, where the degree of membrane permeabilization is determined in real-time (ΔI_p / ΔI_c). In the case of T_1 the user-set threshold is surpassed, therefore additional pulses would not be administered. However, in the case of T_2, the threshold is not achieved, and additional pulses would be administered to the cell in transit. Once the cell exits, the algorithm resets and waits for the next cell entry.

6.2.1 Phase 1—Cell Size Determination

As mentioned, phase I of the feedback algorithm is the accurate calculation of the current drop, ΔI_c. **Figure 6.2** is the representative study to validate this portion of the algorithm. In this study, the LabVIEW program was altered to both save all of the electrical information and stop after 100 trigger events occurred. Following 100 trigger events the algorithm then calculated both the average and standard deviation of the ΔI_c values. This was repeated a total of 10 times. The saved data were then analyzed in MATLAB to calculate this same data to compare to the LabVIEW results. The plots on the top of **Figure 6.2** are generated in MATLAB with black stars added at the points used to calculate the ΔI_c values. The bottom bar graph in **Figure 6.2** is the direct comparison of the real-time LabVIEW code versus the post-processing performed in MATLAB. As shown, there is virtually no difference between the plots. The average difference between the MATLAB versus LabVIEW calculations is a negligible 0.027 nA, validating the feedback algorithm can reliably calculate the ΔI_c value in real-time.

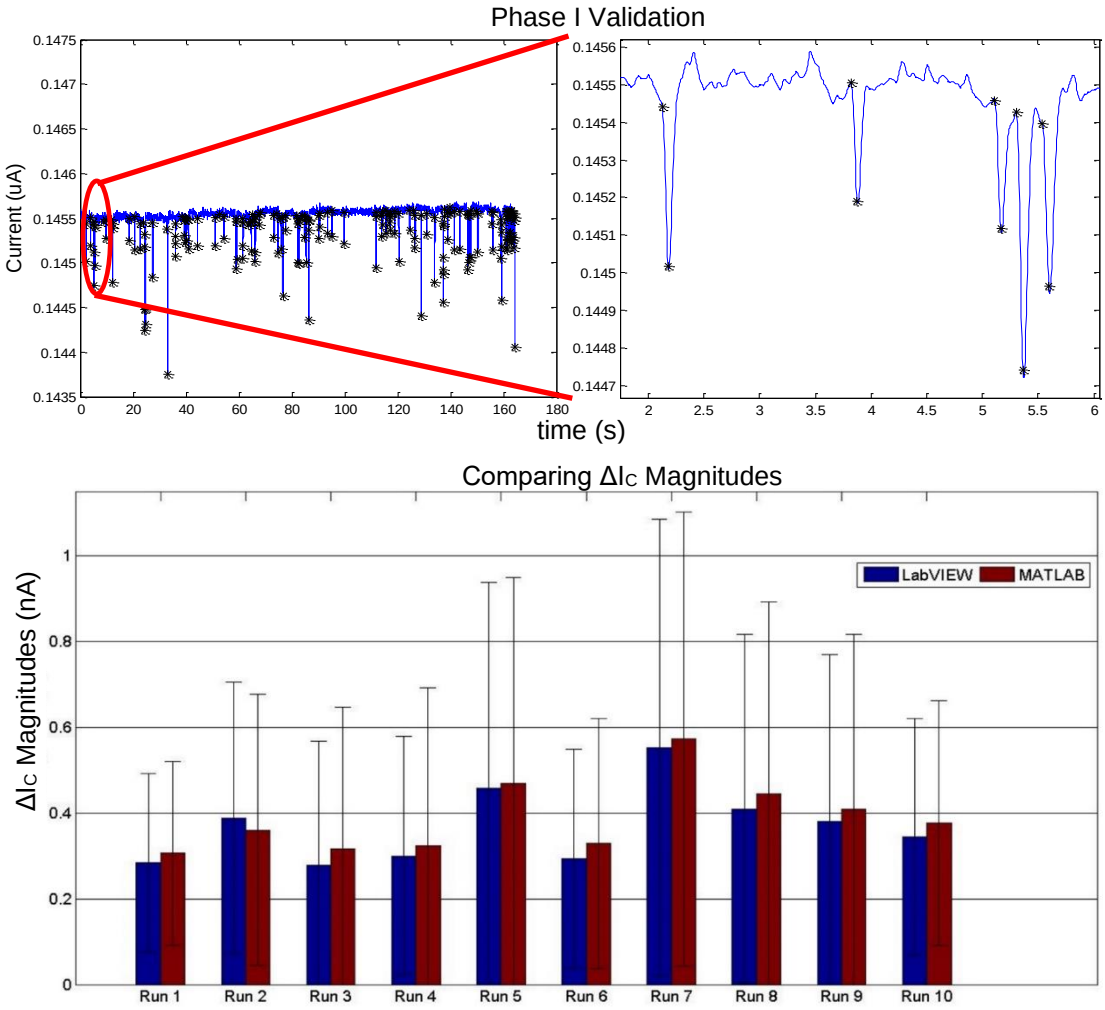

Figure 6.2 Phase I validation. (Top) A representative electrical signal of single cell detections in MATLAB (post processing) with the *'s representing data points used to calculate ΔI_c. (Bottom) A direct comparison of the real-time algorithm (LabVIEW—blue) vs post processing in MATLAB (red) of a total of 100 cells for each individual run. An average difference of 0.027 nA was found between both methods of ΔI_c calculation. This negligible amount indicates the accuracy of phase I of the feedback-control algorithm.

To further validate the system, a COMSOL analysis was performed to calculate the expected ΔI_c current values for a range of cell sizes, shown in **Figure 6.3** (**A-B**). These values were then compared to the actual cell size distribution of 3T3 cells determined using a Coulter Counter (**C**). The exact channel dimensions were constructed in COMSOL, containing the same material properties used during experimentation (refer to Chapter 4). Surface integrals were taken $\int A\ \sigma * E * dA$ to calculate the expected current value. This was performed with no cell present, followed by cells of various radii, to generate a plot of the expected ΔI_c as a function of cell volume (**B**). A Coulter Counter analysis was then performed to determine the size population of the 3T3 cells (**C**). The resulting volumes correspond to cells in diameter ranging from 10 μm to 18 μm. The ΔI_c values calculated in COMSOL also comparatively matchup with the previously experimentally calculated values (**Figure 6.2**), further validating phase I operation of the feedback algorithm.

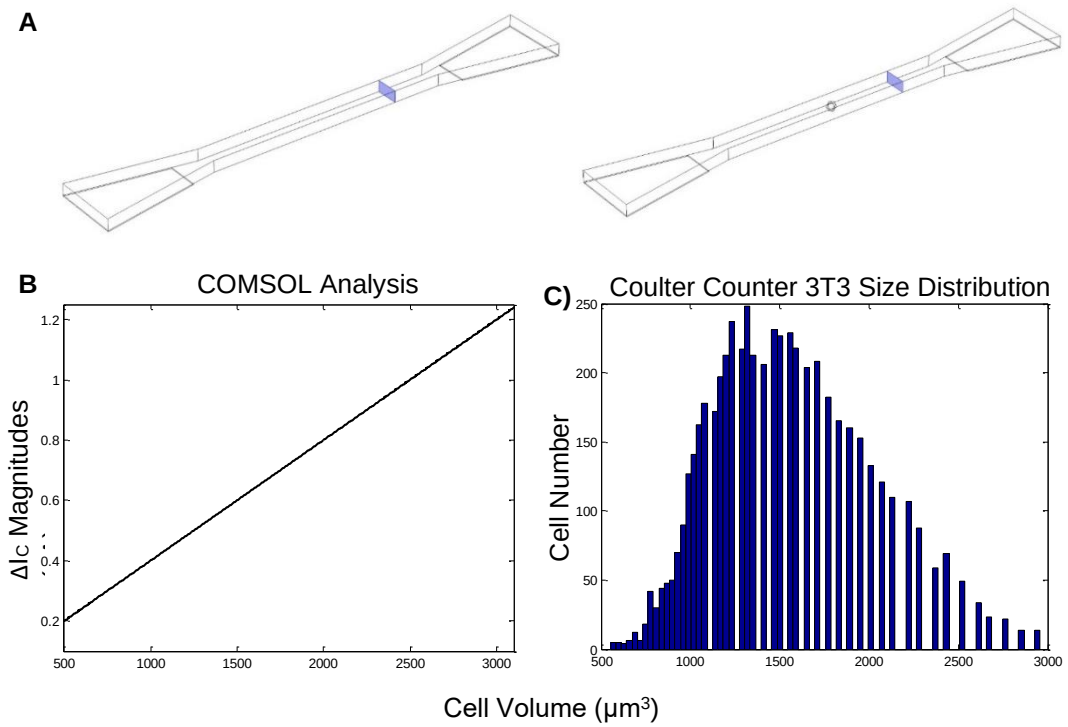

Figure 6.3 Phase I validation—COMSOL. To further validate the ΔI_c magnitudes seen during experimentation, a COMSOL analysis was performed. (A) Illustration of the surface integral solved ($\int A\ \sigma * E * dA$) to estimate the current change due to the cells presence within the micro-device. Cells of various radii were simulated to gather a relationship between ΔI_c magnitude and cell volume (B). To verify, 3T3 cell size was determined using a Coulter Counter (C). The population size distribution on the x-axis corresponds to cell diameters of 10 μm to 18 μm and the predicted current drops corroborates with experimental results.

6.2.2 Phase 2—Pulse Application and Cut-Off

Though phase I of the algorithm is operating efficiently, with the introduction of the external pulse application to the electrical sensing system during phase II, complications are introduced. **Figure 6.4** is an electrical recording of a cell that is pulsed with a high energy electroporation pulse (1.8 kV/cm : 330 μs). In this case, a 500 μS/cm buffer (optimized buffer from Chapter 3) was used for the electroporation buffer (note the baseline of ~847 nA). A large pulse artifact is introduced into the sensing system. This is troublesome for performing feedback, as this capacitive discharge is superimposed onto the cell membrane permeabilization signal. This artifact is not consistent, making for a real-time filter to be a difficult solution. In addition, a real-time filter implemented into the algorithm would further bog down an algorithm that must react as fast as possible given such a limited window of time per cell in transit.

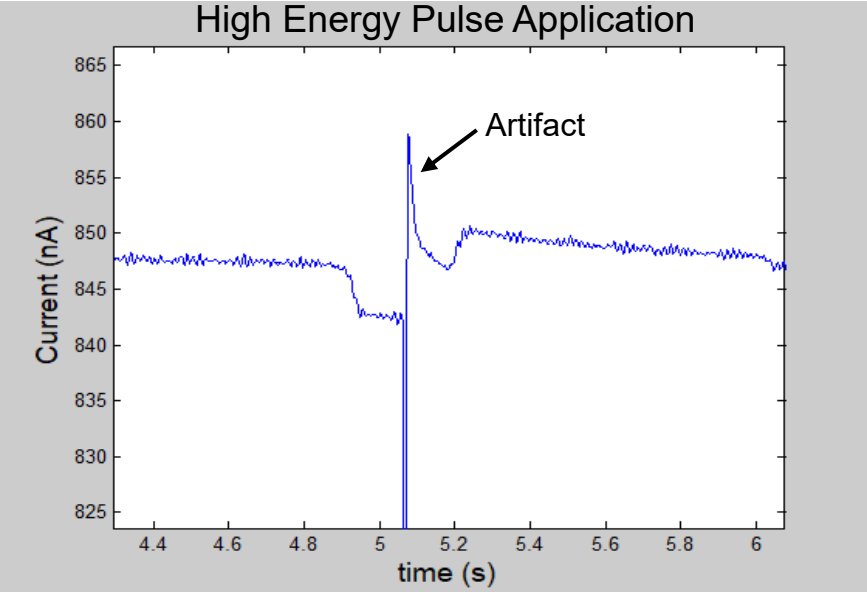

Figure 6.4 High energy pulse application artifact. Electrical recording of a cell suspended in 500 µS/cm buffer (hence higher baseline current) pulsed by a 1.8 kV/cm : 330 µs electroporation pulse. The high energy pulse results in a sharp spike in the electrical recording, introducing problems for the feedback algorithm that will need to be addressed in future prototypes.

A different solution to this problem is to move away from a single, high energy pulse, to an applied pulse train of lower energy pulses. In this situation, instead of reaching the desired permeabilization level after the first pulse, the permeabilization state of the cell would increase with the increasing number of pulses applied. This idea is more akin to the desired feedback-controlled algorithm operation principle. However, new problems arise in this scenario which require a high level of system optimization to properly execute this approach in the feedback-algorithm framework. In particular, the settings of the lock-in amplifier must be optimized to not only allow for cell membrane permeabilization detection, but also for a quick recovery to the current signal following pulse application. The settings that require optimization are the lock-in frequency and the time-constant. Each combination will influence both the signal-to-noise ratio of the electrical recording and the recovery time to the signal (referred to as the blackout period). A preliminary optimization experiment is discussed/shown in **Appendix C**.

Figure 6.5 builds off this preliminary study to show the requirement of an additional variable that needs optimized for feedback-control, pulse delay time. In this study, the lock-in frequency was increased to 3 kHz (typically is ~1 kHz) with a time constant of 800 µs (typically ~2 ms) to allow for a quick recovery back to the electrical signal. In this experiment, upon cell detection, a pulse train was applied to the cell in transit with electric field strength of 0.5 kV/cm and duration of 200 µs (the lower limit of pulse duration for the current electronics). In **(A)**, a total of 3 pulse were applied with 10 ms 'off' time between consecutive pulses. It is evident that given these lock-in settings, the 10 ms between pulses is not long enough to allow for the electrical signal to 're'-lock-in (i.e. it never reaches back to the baseline magnitude). Whereas, in **(B)**, the total pulses applied

was 10, with an ‘off’ time of 30 ms between pulses. In this situation, the current level surpasses the magnitudes prior to pulse application, and an evident increase in permeabilization can be observed with consecutive pulse applications, until the cell exits the electrodes.

This balancing of variables further complicates algorithm development, as the average cell transit time is ~250 ms, with a long delay in the ‘cell-detection’ to ‘pulse-application’, the window to perform real-time feedback-control is even smaller. From a realistic perspective, the current state of the system (LabVIEW-based, Zurich lock-in amplifier) is not built to function at the speeds necessary for a reliable, real-time single-cell level feedback-controlled micro-electroporation device. System upgrades will be necessary in the future or alternative approaches must be implemented to achieve a high throughput, smart electroporation device.

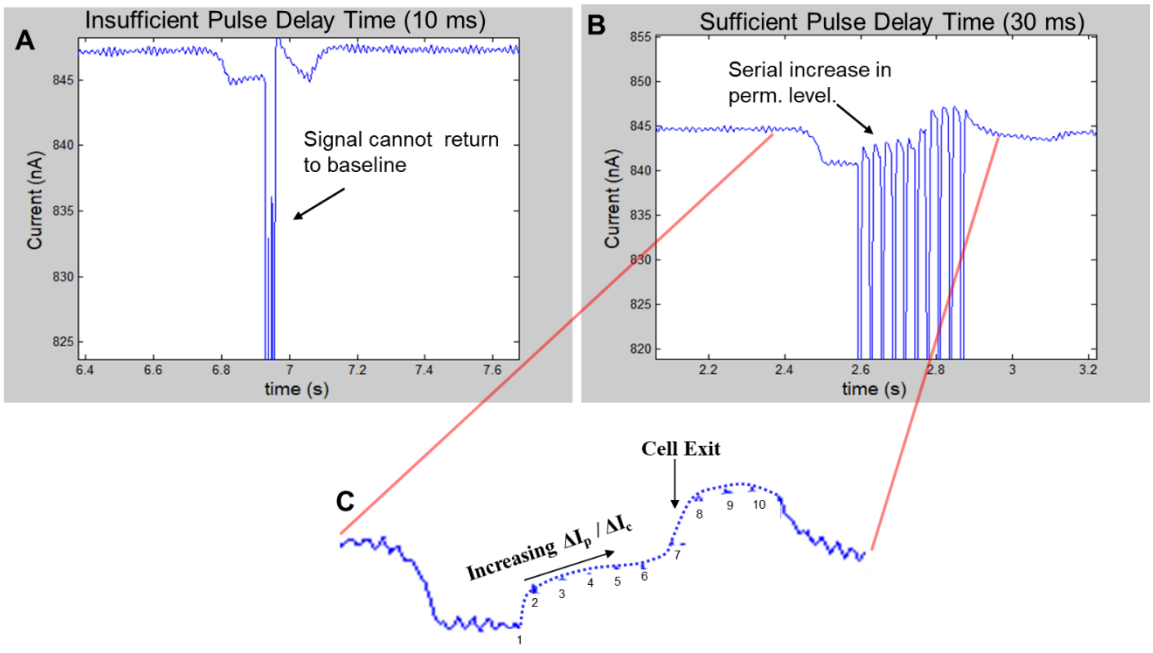

Figure 6.5. Balancing pulse delay for feedback algorithm. A major drawback using the Zurich lock-in amplifier is balancing the various settings to allow for the quick response times necessary to perform single cell level feedback control in a flow environment. For these plots the lock-in frequency was increased to 3kHz with a time constant of 800 µs to decrease the black-out period between pulses. A pulse train of either 3 (A) or 10 (B) pulses of parameters 0.5 kV/cm : 200 µs were applied. (A) A 10 ms pulse of duty cycle 2% was used. Note that this condition did not allow enough time between pulses for the sensing equipment to reach the current level required for the feedback algorithm. (B) A 30 ms pulse of 0.7% duty cycle was used. In this case, the longer 'off-time' between pulses allows ample time for the electrical signal to surpass the baseline current necessary for feedback. In this case, a consecutive increase in membrane permeabilization is observed until the cell exits the electrode set. (C) Removal of the 'blackout' period showing the increase in the degree of cell membrane permeabilization with each additional pulse application until the cell exits (following pulse 7).

6.3 Conclusion / Future Directions

The proposed algorithm in this chapter, with continued system improvements, will be able to achieve the desired outcome of single-cell level, feedback-controlled electroporation in a continuous flow, high throughput fashion. However, with the current prototype installment, this goal is simply unattainable. In order to achieve control of the degree of cell membrane permeabilization at the single-cell level, the first requirement is the installment of a Coulter Counter module (phase I of the algorithm). The current LabVIEW based algorithm was able to reliably and accurately operate as a Coulter Counter in its ability to calculate the ΔI_c magnitudes in real-time. The problems associated with using LabVIEW as the programming environment are evident when phase II of the algorithm is initiated.

Since the cell size calculations are accurate, we know the detection of the cell is occurring simultaneously with the entrance into the electrode set. However, upon initiation of the applied pulse, we see a delay of 80 ms – 100 ms from the time of detection and the time of pulse application. This slow reaction, a combination of the software (LabVIEW is a slow programming language) and the complexity of the Zurich lock-in amplifier sensing and data transmission, makes it almost impossible to sense the response (assuming we have no pulse artifact) and apply additional pulse applications given our window to probe the cell is ~ 250ms. These limitations require further prototype advancement.

The first and possibly easiest advancement is moving from the slow, LabVIEW-based programming environment, into a C+ language that can be programmed onto the real-time module of the Zurich lock-in amplifier. Upon completion, similar studies performed throughout this chapter will need to be redone to ensure the algorithm is working

efficiently, as well as making sure this allows for the fast, real-time requirements necessary to perform the single-cell feedback-control in a continuous flow environment. Alternatively, a separate hardware device may have to be developed based on the necessary functions required by the lock-in, without many of the 'bells and whistles' capabilities that may delay the functionality of the system. Ideally, this device would be able to perform the sense-detect-pulse-sense application required with minimal software intervention. In parallel with this idea, a scale-up, parallelized microfluidic design must be developed (Refer to Future Directions in Chapter 7), such that high numbers of cells can be processed per unit time. This is a necessity, as how the system currently stands with the slow operating times, when running at 100% efficiency, only 4 cells per second can be processed with a single set of electrodes. This intrinsic low throughput opens the door to investigate alternative approaches that can apply this technology, but in a more translatable fashion.

One approach is a 'population-based' feedback-controlled electroporation system, which is depicted in **Figure 6.6**. The methodology behind this idea is to utilize the current technology's capability of monitoring the degree of cell membrane permeabilization to make an autonomous decision as to what is the 'best-case' scenario pulse application for the entire population of cells under test. To start the system will operate at a slow flow rate, Q_0, to allow for a flow of single cells through the electroporation region. The 'detect-pulse-sense' capabilities of the existing algorithm works perfectly under these conditions. The pulse generator will be programmed to generate the initial pulse of E_0 / t_0. After a significant number of cells have been pulsed and the average $\Delta I_p / \Delta I_c$ is calculated, the applied pulse energy will increase to the next programmed value. This process will continue until all pulses have been applied, generating the $\Delta I_p / \Delta I_c$ versus Electrical Energy curve. From this

curve an electroporation pulse will be chosen that causes significant membrane permeabilization to both minimize cell death and maximize electro-transfection efficiency. Simultaneously, both the pulse generator and flow generation system will receive an input to alter their settings. The flow system (shown as a syringe pump in **Figure 6.6**) will increase the flow rate to drastically increase the throughput of the cells in the device ($Q_{throughput}$). At this stage, the system will no longer be capable of performing the single-cell electrical interrogations. Therefore, the pulse generator will change from a triggered setting to constantly output a pulse waveform (E_{opt} / t_{opt}) at a duty cycle that is synchronized with the new cell transit time. This ensures that each cell in transit will be pulsed with a single pulse at the desired strength. Though this system does not account for variability from cell to cell, it will allow the researchers to account for variability across different cell types and day to day variability seen within the same cell type. All the while increasing the throughput of the device to achieve cell numbers that are necessary for most biomedical and clinical settings. Preliminary results using a rudimentary version of the population-based feedback-control are shown in the Future Directions of Chapter 7.

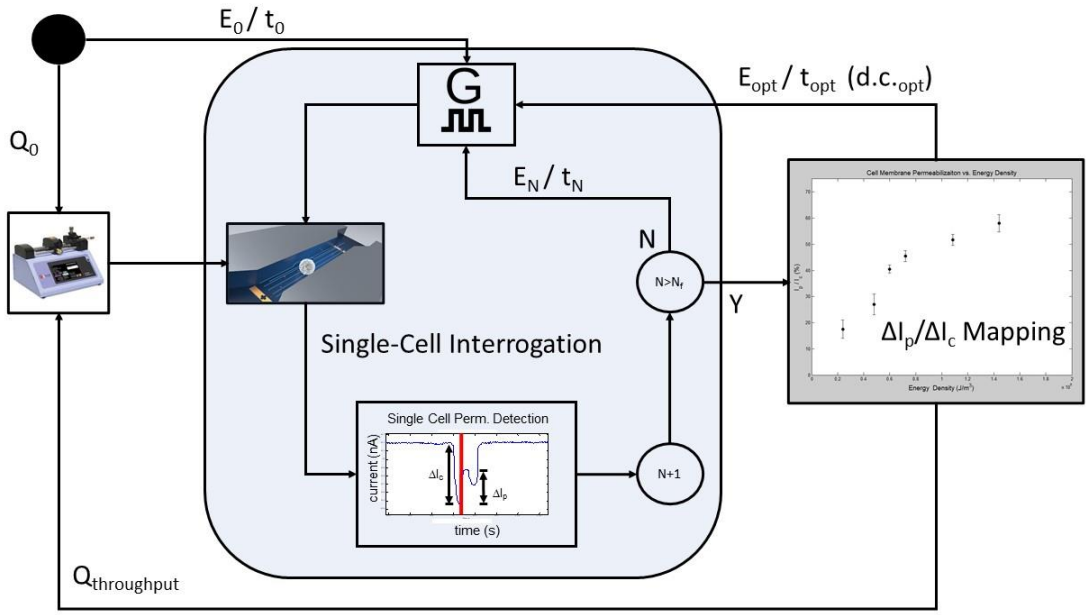

Figure 6.6. Population-based feedback control algorithm. An alternative approach to performing single-cell level feedback control is a population-based algorithm. The schematic shows a proposed method for doing so. Initially, a slow flow rate is programmed (Q_0) to allow for single-cell level interrogation. A set number of cells will be pulsed with a series of pulses (E_0 / t_0 – E_N / t_N). The algorithm will map out the cell membrane permeabilization curve and select an optimal pulse for the given cell population. The flow rate will be increased to $Q_{throughput}$ and the 'detect-pulse-sense' single cell interrogation will be omitted. The optimal pulse train will be continuously applied E_{opt} / t_{opt} at $d.c._{opt}$ such that each cell will received the desired pulse based on the cell transit time and the duty cycle (d.c.).

6.4 Chapter References

1. Zheng, M., *et al.* Continuous-flow, electrically-triggered, single cell-level electroporation. *Technology*, 2017, **5**, 31-41.
2. Huang, Y., & Rubinsky, B. Microfabricated electroporation chip for singe cell membrane permeabilization. *Sensors and Actuators*, 2001, **89**, 242-249.
3. Khine, M., *et al*. Single-cell electroporation arrays with real-time monitoring and feedback control. *Lab-on-a-Chip*, 2007, **7**, 457–462.
4. Guo, X. & Zhu, R. Controllable in-situ cell electroporation with cell positioning and impedance monitoring using micro electrode array. *Scientific Reports*, 2016, **6**, 1-8.
5. Bürgel, S.C., *et al*. On-chip electroporation and impedance spectroscopy of single-cells. *Sensors and Actuators B: Chemistry*. 2015, **210**, 82–90.
6. Brown, D.W, *et al.* Development of an adaptive electroporation system for intratumoral plasmid DNA delivery. *Bioelectrochemistry*. 2018, **122**, 191-198.
7. Atkins, R.M., *et al*. Impedance spectroscopy as an indicator for successful *in vivo* electric field mediated gene delivery in a murine model. *Bioelectrochemistry*. 2017, **115**, 33-40.
8. Ghadami, M., *et al.* Model-based feedback control of a microfluidic electroporation system. *Journal of Micromechanics and Microengineering*. 2013, **23**, 125032.
9. Jagtiani, A.V, Carletta, J., & Zhe, J. An impedimetric approach for accurate particle sizing using a microfluidic Coulter counter. *Journal of Micromechanics and Microengineering.* 2011, **21**, 045036.
10. Sun, T., & Morgan, H. Single-cell microfluidic impedance cytometry: a review. *Microfluidics & Nanofluidics.* 2010, **8**, 423–443.

Chapter 7

Conclusion and Future Work

7.1 Summary on Resuspension Buffer and Electroporation Outcome

Chapter 3 involves a large body of research utilizing macroscale or bulk electroporation to showcase the effect that different molecular compositions of electroporation buffer have on the resulting electroporation outcomes, i.e. cell viability and electro-transfection efficiency. Much detail goes into discussing the background and importance of the work as well as the experimental design. The results focus on showing the effects that both electroporation pulse energy and different ionic contents in the buffer have on cell viability and electro-transfection efficiency. The discussion centers around the role that Mg^{2+} ions play in the electroporation process, how this ion preserves cell viability and hinders electro-transfection efficiency. Different biochemical/enzymatic mechanisms are speculated upon for these effects and supporting evidence for the role that ATPase membrane ion transporters play in cell recovery is shown/discussed. Lastly, a rating system is introduced, termed the electroporation outcome score, to distinguish which buffers/pulsing conditions achieves the best outcomes. A major takeaway from this study is that Mg^{2+} concentration should be optimized in electroporation buffer to improve outcomes. Future studies are introduced, expanding to both more electroporation buffer compositions and cell types to be tested.

7.1 Summary of Cell Membrane Permeabilization Detection

Chapter 4 re-introduces the microfluidic technology. The study and experimental design are introduced, with a focus on the microfabrication and experimental set-up. In this work several electroporation parameters were studied, and the electrical response of the cell membrane was recorded. An electrical metric was created to represent the degree of cell membrane permeabilization ($\Delta I_p / \Delta I_c$). In order to validate that this technology was capable of electrically monitoring the degree of membrane permeabilization, an optical study was performed utilizing propidium iodide, a live/dead cell stain that is impermeable to an intact cell membrane and fluoresces upon binding to nucleic acid. The fluorescence signal was shown to be strongly correlated to the electrical signal, indicating the technology's capabilities of electrically monitoring electroporation events.

7.3 Summary of Biosensor for DNA Electro-Transfection

Chapter 5 focuses on using this technology for a more clinically relevant application, plasmid DNA transfection encoding for green fluorescent protein. The chapter shows the evolution of the technology, explaining microfluidic device changes as well as hardware improvements. Like chapter 4, major results from chapter 5 include correlating the electrical response of the cell to the resulting cell viability, electro-transfection efficiency, and the applied pulse electrical energy. Additionally, the same scoring metric introduced in chapter 3 (electroporation outcome score), is correlated with both the applied pulse energy and the electrical response of the cell, or the degree of membrane permeabilization. What is found is an optimization curve, showing that to achieve both high cell viability and high electro-transfection efficiency there exists a finite region of cell membrane permeabilization in which this can be achieved. This result highlights the ability of this technology to serve as a biosensor to aid in the optimization of electroporation protocols. Finally, future directions are introduced which speak on expanding the data set, to include more cell types.

7.4 Summary of Smart Electroporation Technology

Chapter 6 focuses on the state of the art in terms of the detection software and introduces the idea of a closed-loop, feedback-controlled electroporation device. Such a device would be able to perform electroporation of single cells with the highest level of control, accounting for the intrinsic variability amongst a cell population. A software algorithm capable of performing this level of control is introduced as well as various bottlenecks and alternative approaches to achieve this goal are in the conclusion/future directions. The major alternative approach / future direction being the idea of a population-based feedback-control micro-electroporation platform.

7.5 Additional Preliminary Experiments and Future Work

New Cell Types

To date, the majority of the work has been done using mouse 3T3 fibroblast cells. Though this cell line is a good choice for the micro-electroporation technology advancement, it does not represent a good cell for translatable applications, such as cell therapeutics. Further validation of this technology should be accomplished using different representative cell lines and more importantly, primary human cells. Preliminary work has been performed using human embryonic kidney cells (HEK293), an engineered HEK293 cell line for CRISPR-Cas9 experiments, a representative white blood cell line (Jurkat T cell lymphoma), and human mesenchymal stem cells (hMSCs). **Figure 7.1** is the electrical data representative of the degree of cell membrane permeabilization versus electrical energy density for m3T3 cells versus hMSCs. The hMSC cell membrane response is slightly shifted to the left compared to the m3T3 cells. This indicates that this cell line permeabilizes at a lower pulse energy density compared to the m3T3 cells. This finding makes sense as the hMSCs have a larger average cell diameter compared to that of the m3T3 cells. Additionally, comparing published commercial electroporation protocols for the NEON system, the ratio of the applied electrical energy for 3T3 to hMSC is approximately 2. Whereas, the electrical data in **Figure 7.1** suggests a similar ratio of approximately 1.5.

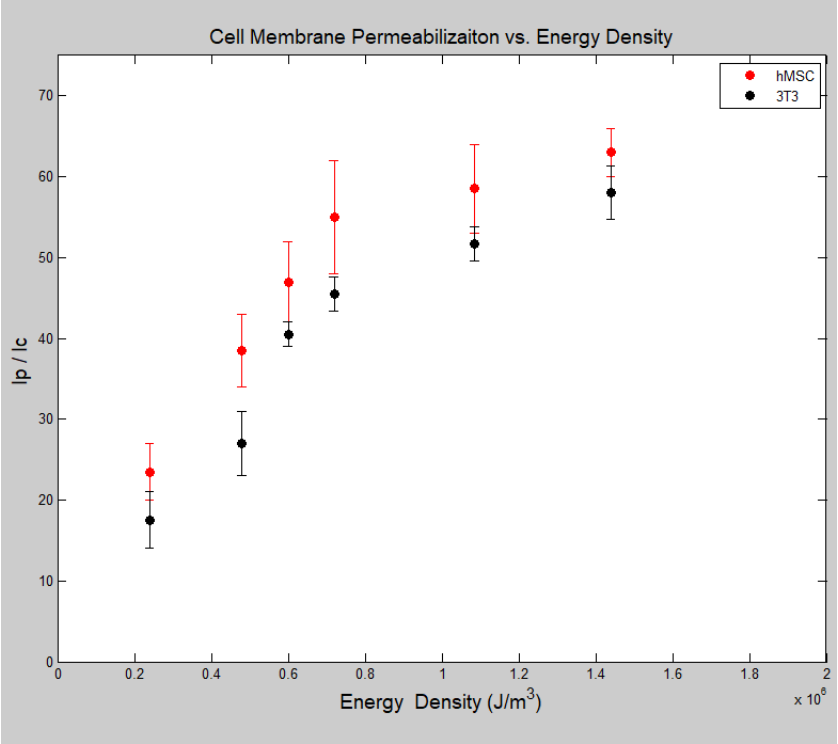

Figure 7.1. Comparing the Degree of Cell Membrane Permeabilization of Different Cell Types. Comparing the response of 3T3 cells to human mesenchymal stem cells (hMSCs), it is shown that the electrical response for hMSCs is shifted slightly to the left, indicating they are easier to permeabilize than 3T3 cells. Phenomenologically, hMSCs are larger than 3T3 cells and therefore this result is expected.

Although a full characterization is still necessary for the hMSC and other cell types, preliminary results of successful pDNA encoding GFP have been achieved. Representative images are shown in **Figure 7.2**. For the m3T3 cells, hMSCs, and HEK293 cells, they were suspended in the optimized Mg^{2+} / K^{+}, 500 µS/cm buffer (from Chapter 3), and the detect-pulse program was utilized. However, when testing the Jurkat, T cell lymphoma cell line complications were introduced. First, this cell line was incompatible with the low conductivity electroporation buffer, such that cell viability was significantly affected even at low energy pulse applications. To workaround this issue, the Jurkat cells were simply electroporated in their suggested RPMI-1640 cell culture medium (conductivity ~ 10 mS/cm). The high conductivity further complicated the execution of the micro-electroporation setup. The 'standard' pulses that have been used (Chapter 3 and Chapter 5) produced highly undesirable electrolysis, causing bubble formation in the device. To mitigate this concern, an imperfect pulsing scheme was utilized to test for GFP expression. The image in **Figure 7.2B** was the result of a pulse train of 6 pulse of 2 kV/cm : 200 µs, with an off time of 9.8 ms between pulses. This did not guarantee all cells were pulsed, a major flaw in the experimental design. Another problem presented itself due to the high conductivity RPMI-1640 medium, electrode degradation over time. This is shown in **Figure 7.3**. Though the electrodes remained functional, the experimental reliability will be affected when sensing is involved. Also, upon further degradation, the electrode set would be unusable. Since white blood cells are extremely relevant in a clinical setting, many of these technical limitations must be addressed to better equip this micro-electroporation technology to handle this precious cell type. Another buffer optimization study should be performed specific to white blood cells, with hopes of finding a recipe with a lower

conductivity that does not drastically affect their viability upon external electroporation pulses. Additionally, alternative approaches in both microfluidic / electronic design may be necessary to mitigate the electro-chemical reactions taking place in the fluidic environment, with hopes of enhancing the range of pulse applications possible to test for this cell type.

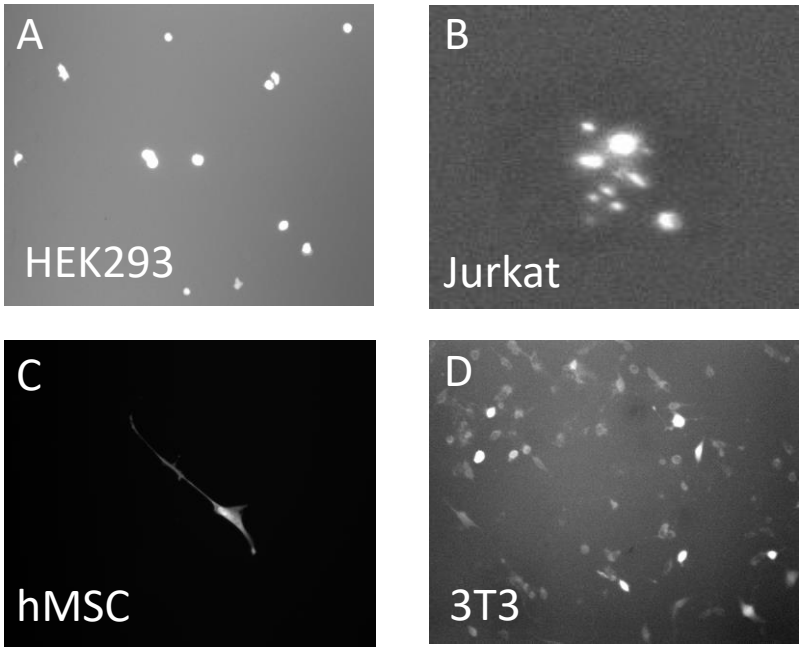

Figure 7.2. GFP Expression in Different Cell Types. Preliminary experiments have been performed using the microfluidic electroporation platform to successfully transfect different cell types with pDNA encoding for GFP. The cell types that have successfully transfected are: (A) Human Embryonic Kidney Cells (HEK293), (B) Jurkat T Cell Lymphocytes, (C) Human Mesenchymal Stem Cells, and (D) Mouse 3T3 Fibroblast Cells.

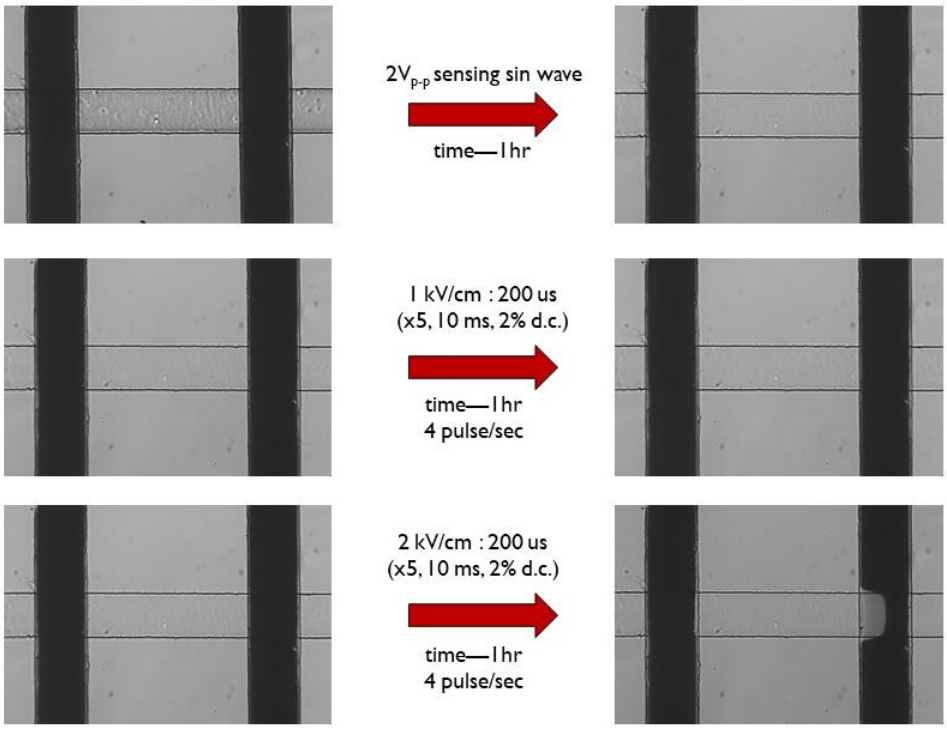

Figure 7.3. Electrode Degradation in High Conductivity Buffers. The left side is an image before the described pulsing waveform was applied for 1-hour duration. A frequency of 4 Hz was chosen to simulate the device operating at 100% efficiency (4 cells/second). The electroporation buffer used in this study is the Full RPMI 1640 media, having a conductivity of ~ 10 mS/cm. The bottom row of images show the effect of a high 2 kV/cm : 200 µs with an off time of 9.8 ms between consecutive pulses. After 1 hour, a clear electrode degradation effect can be seen. Though, the electrode set is still functional in this state, it introduces a set of new challenges to be overcome.

New Applications

As was discussed in Chapter 6, an alternative approach to performing single-cell level feedback control is a population-based methodology. In this scenario, a single-cell interrogation will be accomplished across multiple pulse strengths to generate the degree of cell membrane permeabilization versus electrical energy density curve. From this data, an optimal pulse is decided upon and the system switches to a high throughput mode. Such that the flow rate is increased, and the pulse application is constantly applied with a duty cycle matching that of the cell transit time. This is to ensure that the likelihood of the scenario is that each cell in transit will receive the specified electroporation pulse.

Preliminary evidence using this platform has been performed on a specialized HEK293 cell type (**Figure 7.4**). **Figure 7.4A** utilizes this cell line in the conventional way by simply performing a DNA transfection, encoding for GFP protein. The pulse application in this scenario was a 1.8 kV/cm : 670 μs pulse (50 ms pulse at 1.4% duty cycle). The initial results were promising, with an eTE greater than 60%. Further testing and system improvement will further enhance the electro-transfection capabilities of this population-based feedback control platform.

However, the main application to be used with this new cell line is shown in **Figure 7.4B.** These HEK293 cells were engineered for CRISPR-Cas9 gene editing experiments, such that they naturally produce a non-functional GFP protein. Upon receiving both DNA plasmids encoding for the Cas9/effector protein and guide RNA, respectively, the malfunctioning GFP gene can be corrected and the cells then produce GFP and can be visualized using epifluorescence microscopy (**Figure 7.4B**). Using the same pulsing scheme as mentioned above, a correction ratio of ~5% was shown with the population-

based feedback control micro-electroporation platform. This experimental design is much more complex than a simple pDNA transfection making it impossible to draw comparisons between them. For instance, 2 plasmids must be co-delivered for the Cas9/effector protein and guide RNA (plasmid sizes are 9.3 kbp and 3.5 kbp, loaded at concentrations of 750 ng/mL and 250 ng/mL, resprectively). The products of the transfection must be expressed at overlapping time intervals and come into close proximity of each other, all-the-while being transported into the nucleus of the cell. Lastly, the Cas9/guide RNA complex must bind at the exact position along the DNA in order to fix the mutation. However, 5% correction efficiency showcases the ability of this technology to successfully perform precise gene editing, and with further advancement of the platform this correction efficiency will surely improve.

Note: The specialized HEK293 cell line and both DNA plasmids for performing the CRISPR/Cas9 experiments were a generous gift from the Shengkan (Victor) Jin Lab from the Department of Pharmacology at Rutgers University.

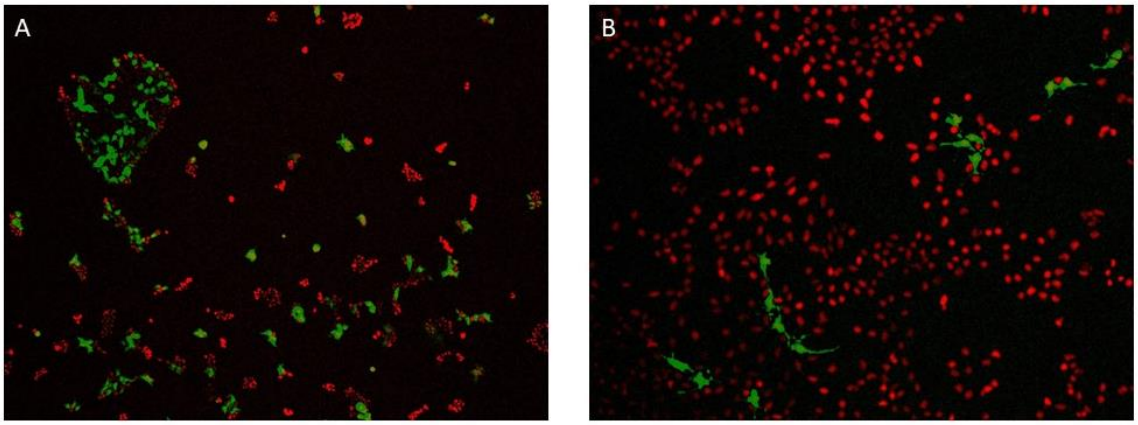

Figure 7.4. Population-Based Feedback Control Applications. The population-based feedback method (constant pulsing at a duty cycle matched to the cell transit time) was tested for two different applications using an engineered HEK293 cell line. (A) The standard pDNA encoding GFP expression. eTE was ~60 to 70% for a 1.8 kV/cm : 670 µs pulse. DNA plasmid was at a final concentration of 20 µg/mL (B) CRISPR-Cas9 application where GFP expression is indicative of a successful gene editing experiment. The correction efficiency was ~ 5% with the same 1.8 kV/cm : 670 µs pulse. DNA plasmids were at a total concentration of 1 µg/mL, with 750 ng/mL of the 9.3 kb Cas9/effector plasmid and 250 ng/mL of the 3.5 kb guide RNA plasmid.

Device Scale-up

The implementation of the population-based feedback control micro-electroporation platform allows for higher flow rates to be used during experimentation. Thus, equating to a higher device throughput. However, even with this enhancement, in order to achieve throughputs that would be required to translate to a clinical / cell therapy setting, further design alterations must be implemented to achieve this goal. One idea is to simply parallelize the number of electroporation devices, leading to a multiplication factor of the total cell throughput capabilities. **Figure 7.5** is a CAD drawing of an envisioned 256 channel device. This design has a total fill volume of 55 µL and upon running at 100% efficiency (i.e. 4 cells per second in the detect-pulse platform) this design can achieve a cell throughput of 3.6×10^6 cells/hour. Therefore, implementing the population-based feedback control technology onto this microfluidic chip will further enhance the cell throughput. Upon testing this idealized system, it is irrational to believe there would not be any complications introduced into to micro-electroporation technology. The overall electronic setup would have to be revamped to allow for 256 individual electrode sets and many microfluidic design iterations would need tested to ensure all the hydrodynamic resistances are properly balanced. However, moving toward a parallelized device that can implement some of the basic technological advancements presented within this thesis has the potential to replace existing technologies used in clinical settings to perform the gene delivery step in cell therapy manufacturing. I am personally excited to see where this project goes in the future and the impact that electroporation in general will have on biomedical and clinical research / medicine.

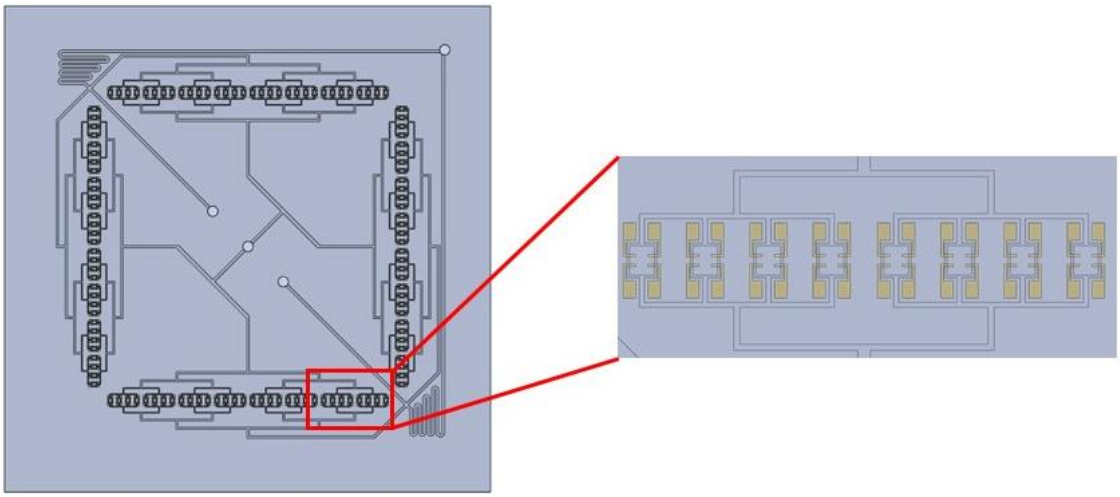

Figure 7.5. CAD Drawing of a Microfluidic Scale Up Design. A conceptualized idea for a microfluidic device design to parallelize electroporation regions. This design has 256 channels in parallel, equating to a total fluidic volume of 55 µL. Device operation at 100% efficiency would allow for the transfection of 3.6×10^6 cells/hour.

Appendix A

Macro-Scale Electroporation Devices (Company, Model)

This is not an all-encompassing list of available electroporation devices, rather commonly used devices/brands that perform cuvette-based electroporation.

- Bio-Rad
    - Gene Pulser
    - MicroPulser
- BTX
    - ECM 830 (**Figure 2.3C**)
    - AgilePulse
    - Gemini Twin Wave
    - ECM 2001+
    - ECM 630
    - ECM 399
- Eppendorf
    - Eporator
- Lonza
    - Nucleofector
- Mirus Bio
    - Ingenio EZporator
- ThermoFisher
    - NEON

Appendix B

Chapter 3—Supplementary Information

This supplementary file contains the results from all of the statistical analyses performed, the two-way ANOVAs and post hoc analysis. These are found in Tables 1 and 2, respectively. Table 1 is further separated into 3 sections, containing the results for the constant applied energy pulse applications, constant charge flux pulse applications, and ATPase inhibition, respectively. Each analysis reports the resulting statistical significance values from each two-way ANOVA. Similarly, Table 2 is separated into three groups and reports the results from the post-hoc analyses that reached statistical significance for the constant charge flux pulse applications. These groupings are: viability, electro-transfection efficiency, and ATPase inhibition viability. Figure 1 is the viability data plots for the various buffer compositions for the pulse applications of the same energy. This demonstrates that there are no significant changes in viability when the same pulse energy is applied. However, at the highest charge flux applications, a slight decrease in cell viability for most electroporation buffers is observed. Lastly, Figure 2 is a plot of viability versus applied pulse energy for the 500 μS/cm Mg^{2+} -containing buffer compositions. No significant differences are found at any pulse energy, indicating the enhancement of viability is independent of the Mg^{2+} source.

Supplementary Figures:

Buffer Composition	Charge Flux	Interaction
Constant Applied Energy --Viability		
All Buffers (500 µS/cm)		
n.s.	n.s.	n.s
All Buffers (2000 µS/cm)		
n.s.	$p = 0.0044$	n.s.
Constant Applied Energy --eTE		
All Buffers (500 µS/cm)		
$p < 0.0001$	$p = 0.0073$	n.s.
Mg^{2+} -Containing Buffers (500 µS/cm)		
$p < 0.0001$	n.s.	n.s.
All Buffers (2000 µS/cm)		
$p < 0.0001$	$p < 0.0001$	n.s.

Supplementary Table 1.1. Two-way ANOVA results for constant applied energy pulsing conditions—Viability and eTE. n.s.- not significant.

Buffer Composition	Appl. Energy	Interaction
Constant Charge Flux--Viability		
All Buffers (500 µS/cm)		
$p < 0.0001$	$p < 0.0001$	$p < 0.0001$
Mg^{2+} -Containing Buffers (500 µS/cm)		
n.s.	$p < 0.0001$	n.s.
All Buffers (2000 µS/cm)		
$p < 0.0001$	$p < 0.0001$	n.s.
Constant Charge Flux--eTE		
All Buffers (500 µS/cm)		
$p < 0.0001$	$p < 0.0001$	$p = 0.0148$
Mg^{2+} -Containing Buffers (500 µS/cm)		
$p < 0.0001$	$p < 0.0001$	n.s.
All Buffers (2000 µS/cm)		
$p < 0.0001$	$p < 0.0001$	n.s.

Supplementary Table 1.2. Two-way ANOVA results for constant charge flux pulsing conditions—Viability and eTE. n.s.- not significant.

Buffer Composition	Appl. Energy	Interaction
ATPase Inhibition--Viability		
$MgCl_2$ versus $MgCl_2$ with Lidocaine		
$p < 0.0001$	$p < 0.0001$	$p < 0.0001$
KCl versus KCl with Lidocaine		
$p < 0.0001$	$p = 0.0074$	n.s.
KCl versus $MgCl_2$ with Lidocaine		
$p < 0.0001$	$p < 0.0001$	n.s.

Supplementary Table 1.3. Two-way ANOVA results for ATPase inhibition experiments. n.s.- not significant.

Buffer 1	Buffer 2	p-value
Constant Charge Flux--Viability		
1.2 kV/cm : 1 ms		
$MgCl_2$ (500)	KCl (Trehalose)	<0.0001
KCl (500)	KCl (Trehalose)	<0.0001
$MgCl_2$/KCl	KCl (Trehalose)	<0.0001
$MgSO_4$	KCl (Trehalose)	<0.0001
1.8 kV/cm : 670 µs		
$MgCl_2$ (500)	KCl (500)	0.0097
$MgCl_2$ (500)	KCl (Trehalose)	<0.0001
$MgCl_2$/KCl	KCl (500)	0.02
$MgCl_2$/KCl	KCl (Trehalose)	0.0001
$MgSO_4$	KCl (500)	0.0005
$MgSO_4$	KCl (Trehalose)	<0.0001
$MgCl_2$ (2000)	KCl (2000)	0.0051
2.4 kV/cm : 500 µs		
$MgCl_2$ (500)	KCl (500)	0.0006
$MgCl_2$ (500)	KCl (Trehalose)	<0.0001
$MgCl_2$/KCl	KCl (500)	0.0001
$MgCl_2$/KCl	KCl (Trehalose)	<0.0001
$MgSO_4$	KCl (500)	0.0015
$MgSO_4$	KCl (Trehalose)	0.0001
3.6 kV/cm : 330 µs		
$MgCl_2$ (500)	KCl (500)	<0.0001
$MgCl_2$ (500)	KCl (Trehalose)	<0.0001
$MgCl_2$/KCl	KCl (500)	<0.0001
$MgCl_2$/KCl	KCl (Trehalose)	0.0076
$MgSO_4$	KCl (500)	<0.0001
$MgSO_4$	KCl (Trehalose)	0.0002
4.8 kV/cm : 250 µs		
$MgCl_2$ (500)	KCl (500)	0.0006
$MgCl_2$ (500)	KCl (Trehalose)	0.0005
$MgSO_4$	KCl (500)	0.0158
$MgSO_4$	KCl (Trehalose)	0.0125

Supplementary Table 2.1. Statistical significance achieved in constant charge flux conditions—viability. Numbers in parenthesis indicate buffer conductivity (μS/cm). KCl (Trehalose), $MgCl_2$/KCl, and $MgSO_4$ buffers had a final conductivity of 500 μS/cm.

Buffer 1	Buffer 2	p-value
Constant Charge Flux--eTE		
1.2 kV/cm : 1 ms		
$MgCl_2$ (500)	KCl (500)	<0.0001
$MgCl_2$ (500)	$MgCl_2$/KCl	0.0004
$MgCl_2$ (500)	KCl (Trehalose)	<0.0001
$MgCl_2$/KCl	$MgSO_4$	0.0342
$MgCl_2$/KCl	KCl (Trehalose)	0.0004
$MgSO_4$	KCl (500)	0.0012
$MgSO_4$	KCl (Trehalose)	<0.0001
KCl (500)	KCl (Trehalose)	0.016
$MgCl_2$ (2000)	KCl (2000)	0.0196
1.8 kV/cm : 670 µs		
$MgCl_2$ (500)	KCl (500)	0.0033
$MgCl_2$ (500)	KCl (Trehalose)	<0.0001
$MgCl_2$/KCl	KCl (Trehalose)	0.0105
$MgSO_4$	KCl (500)	0.0299
$MgSO_4$	KCl (Trehalose)	0.0015
$MgCl_2$ (2000)	KCl (2000)	0.008
2.4 kV/cm : 500 µs		
$MgCl_2$ (500)	KCl (500)	<0.0001
$MgCl_2$ (500)	KCl (Trehalose)	<0.0001
$MgCl_2$/KCl	KCl (500)	0.0033
$MgCl_2$/KCl	KCl (Trehalose)	0.0299
$MgSO_4$	KCl (500)	<0.0001
$MgSO_4$	KCl (Trehalose)	0.0001
$MgCl_2$ (2000)	KCl (2000)	0.0031
3.6 kV/cm : 330 µs		
$MgCl_2$ (500)	KCl (500)	<0.0001
$MgCl_2$ (500)	$MgCl_2$/KCl	0.0413
$MgCl_2$ (500)	KCl (Trehalose)	0.001
$MgCl_2$/KCl	KCl (500)	0.0072
$MgSO_4$	KCl (500)	<0.0001
$MgSO_4$	KCl (Trehalose)	0.0033
4.8 kV/cm : 250 µs		
$MgCl_2$ (500)	KCl (500)	<0.0001
$MgCl_2$ (500)	$MgCl_2$/KCl	0.0151
$MgCl_2$ (500)	KCl (Trehalose)	0.0214
$MgCl_2$/KCl	$MgSO_4$	0.0105

$MgSO_4$	KCl (500)	<0.0001
$MgSO_4$	KCl (Trehalose)	0.0151

Supplementary Table 2.1. Statistical significance achieved in constant charge flux conditions—eTE. Numbers in parenthesis indicate buffer conductivity (μS/cm). KCl (Trehalose), $MgCl_2$/KCl, and $MgSO_4$ buffers had a final conductivity of 500 μS/cm.

Buffer 1	Buffer 2	p-value
ATPase Inhibition--Viability		
1.2 kV/cm : 1 ms		
$MgCl_2$ (500)	KCl (500)	0.0152
$MgCl_2$ (500)	KCl (w/ Lidocaine)	<0.0001
KCl (500)	$MgCl_2$ (w/ Lidocaine)	0.0328
KCl (500)	KCl (w/ Lidocaine)	0.0235
$MgCl_2$ (w/ Lidocaine)	KCl (w/ Lidocaine)	0.0002
1.8 kV/cm : 670 µs		
$MgCl_2$ (500)	KCl (500)	0.0006
$MgCl_2$ (500)	KCl (w/ Lidocaine)	<0.0001
KCl (500)	$MgCl_2$ (w/ Lidocaine)	0.0021
KCl (500)	KCl (w/ Lidocaine)	0.0465
$MgCl_2$ (w/ Lidocaine)	KCl (w/ Lidocaine)	<0.0001
2.4 kV/cm : 500 µs		
$MgCl_2$ (500)	KCl (500)	<0.0001
$MgCl_2$ (500)	KCl (w/ Lidocaine)	<0.0001
KCl (500)	$MgCl_2$ (w/ Lidocaine)	0.0094
$MgCl_2$ (w/ Lidocaine)	KCl (w/ Lidocaine)	<0.0001
3.6 kV/cm : 330 µs		
$MgCl_2$ (500)	KCl (500)	<0.0001
$MgCl_2$ (500)	$MgCl_2$ (w/ Lidocaine)	<0.0001
$MgCl_2$ (500)	KCl (w/ Lidocaine)	<0.0001
4.8 kV/cm : 250 µs		
$MgCl_2$ (500)	KCl (500)	<0.0001
$MgCl_2$ (500)	$MgCl_2$ (w/ Lidocaine)	<0.0001
$MgCl_2$ (500)	KCl (w/ Lidocaine)	<0.0001

Supplementary Table 1.4. Statistical significance achieved in ATPase inhibition conditions—viability. All buffers had a final conductivity of 500 µS/cm and sucrose was used as the osmotic balancing agent.

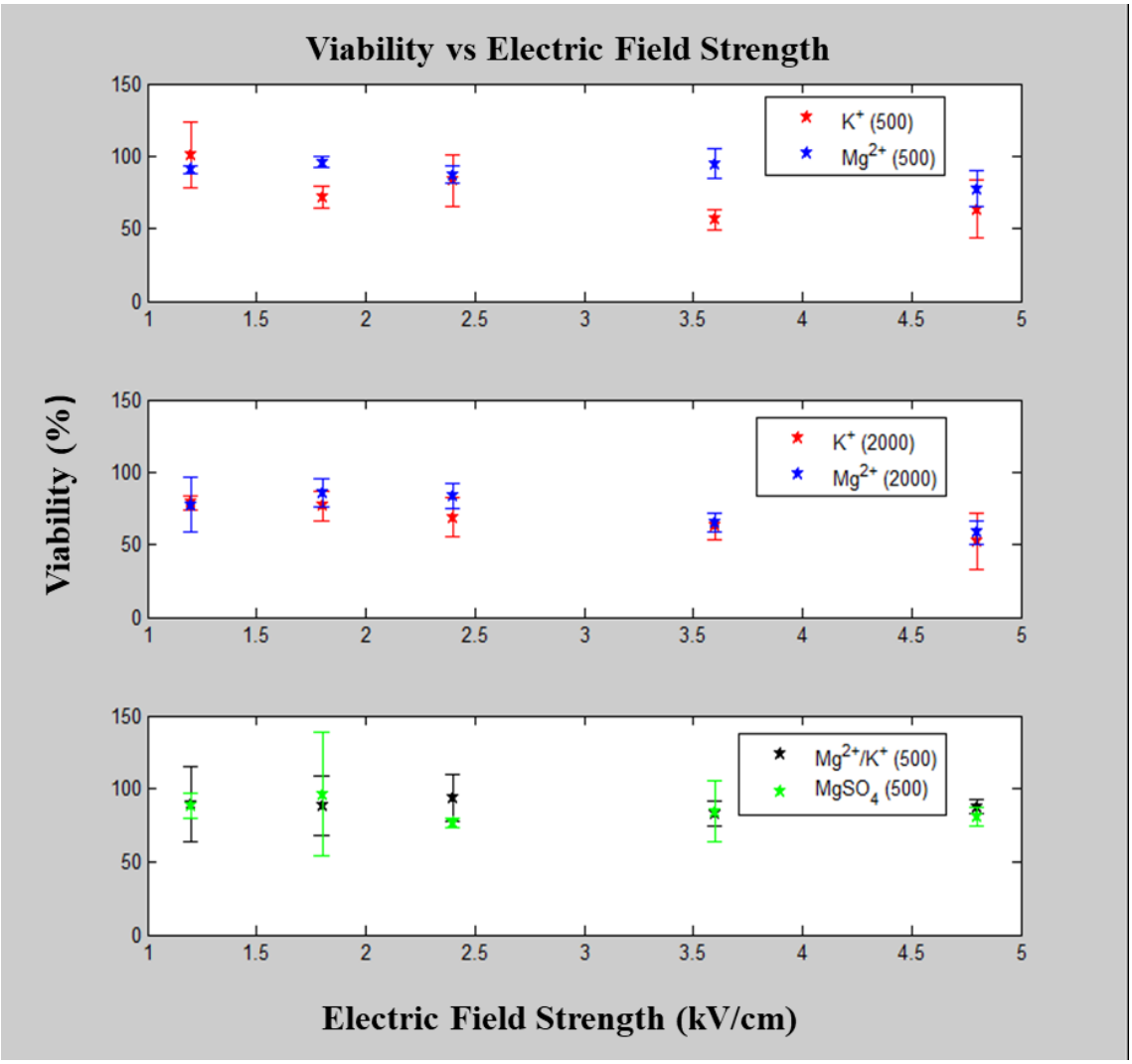

Supplementary Figure 1. Viability vs electric field strength for constant applied energy. (Top) KCl and $MgCl_2$ buffers at 500 µS/cm. (Middle) KCl and $MgCl_2$ buffers at 2000 µS/cm. (Bottom) $MgCl_2$/KCl mixture and $MgSO_4$ buffers at 500 µS/cm. A slight decrease in viability is observed at high electric field strength, short duration, pulse applications.

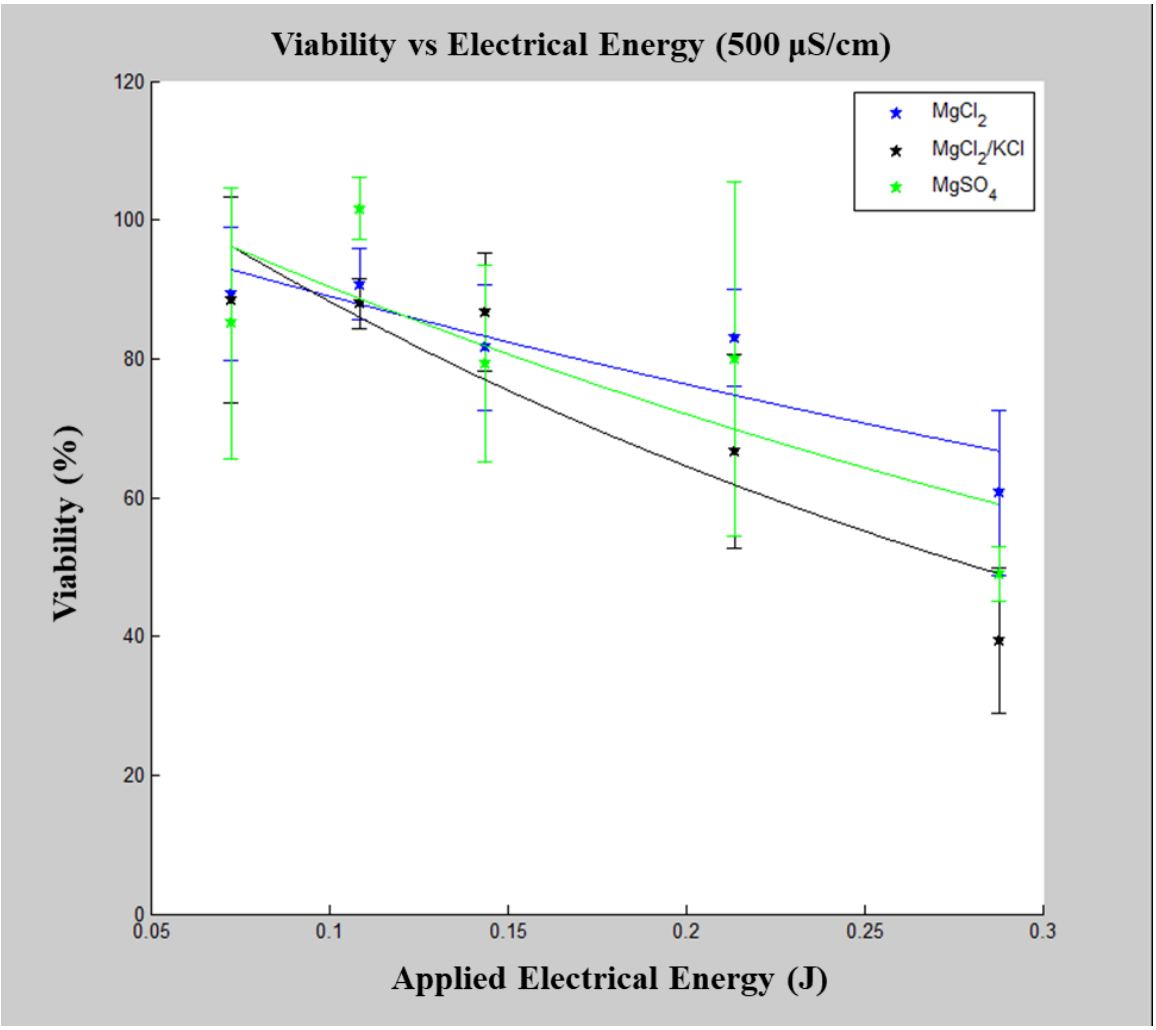

Supplementary Figure 2. Viability vs applied electrical energy for Mg^{2+} containing buffer solutions. Each buffer with a final conductivity of 500 µS/cm and sucrose as the osmotic balancing agent. Statistical significance ($p < 0.05$) was not reached for any pulse applications when comparing $MgCl_2$, $MgSO_4$, and $MgCl_2$/KCl mixture to each other. Data fit to a two-term exponential.

Appendix C

Zurich Lock-in Amplifier Setting Optimization

As mentioned in Chapter 6, the settings of the lock-in amplifier have a significant effect on the ability to perform feedback-control. In this study, a single lock-in frequency of ~1.2 kHz was used, our standard for membrane permeabilization sensing. The time constant was varied from 500 µs up to 70 ms and the 'blackout' time or the recovery time of the lock-in amplifier was determined for each time constant. Three regions were found to exist and are shown in **Figure 1**. The first is shown in red and is the undetectable region. In this case with time constants below 800 µs, the signal-to-noise ratio (SNR) is too low, making it difficult to detect cells and extract important information from their electrical response. The green region (800 µs – 2 ms) would be the optimal range for this lock in frequency. With the average cell transit time at ~250 ms, a blackout period ranging from 10 ms – 35 ms would allow for multiple pulse applications to the cell in transit. Further increasing the time constant, the blue region (2 ms – 5 ms) allows for a high SNR for 'detect-pulse' applications, while keeping a respectably low recovery period. Moving beyond 5 ms leads to a large blackout period that is even undesirable for the 'detect-pulse' platform as cells will inevitably traverse the electroporation region while the system is still recovering, resulting in many more missed events.

This study was performed at a single lock-in frequency. Further optimization to minimize the response time can be achieved by increasing the lock in frequency (i.e. using 3 kHz as in Chapter 6). However, this again turns into a balance of optimization, as increasing the frequency too much will result in unreliable changes in the signal due to the cells presence.

In particular, a cross-over frequency range will be observed at which case the cells presence will no longer cause a drop in current, rather a sharp increase in current, due to the electric field penetrating beyond the cell membrane. In such a case, detecting the degree of cell membrane permeabilization will no longer be possible.

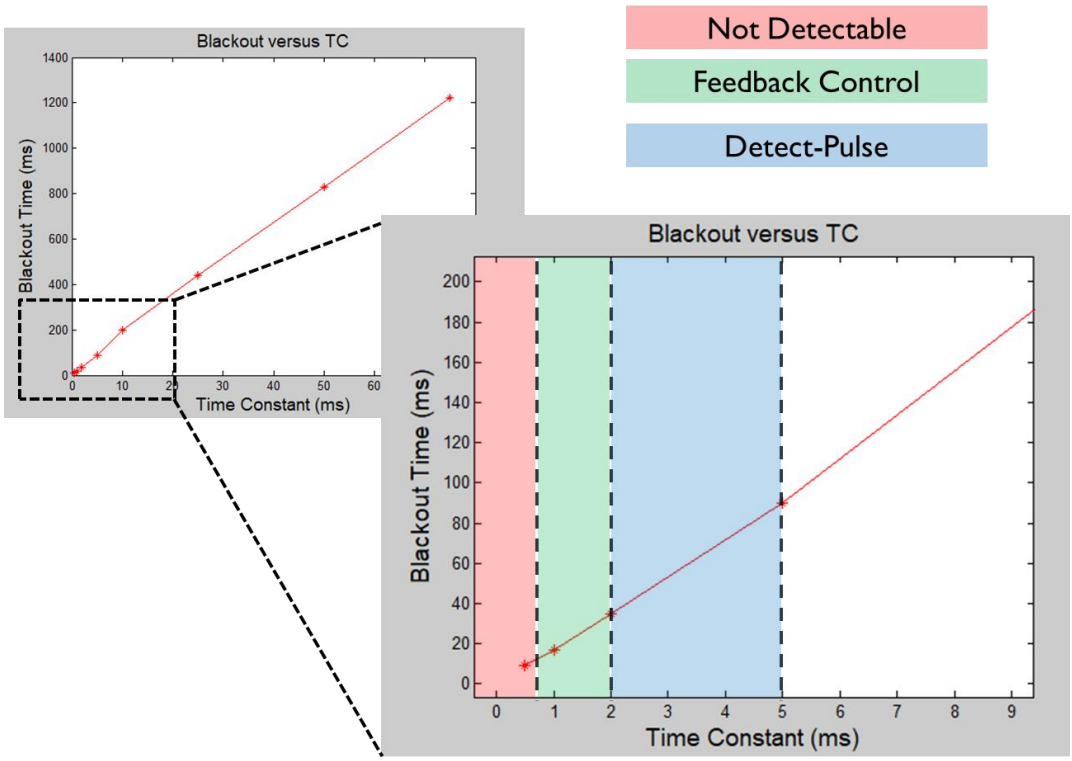

Figure 1. The system recovery period (blackout time) versus the lock-in time constant. The lock-in frequency was kept constant at ~1.2 kHz. For this frequency, three distinct regions were found, 'undetectable' (red), 'feedback-control' (green), and 'detect-pulse' (blue). In the red, below an 800 µs time constant, the SNR was too low to allow for reliable cell detection and feature extraction. As in the time constant increases, the 'sweet-spot' range of 800 µs – 2 ms time constant values allows for a blackout period of 10 ms – 35 ms, respectively. This window would allow for some level of feedback-control. From 2 ms – 5 ms time constant values, this range allows for a high SNR required for the 'detect-pulse' platform of the technology. Further increasing the time constant beyond 5 ms is undesirable, as the recovery period will lead to missed trigger events.